ABSTRACT

Title of Document: SYNTHESIS AND CHARACTERIZATION OF PRODUCTS PRODUCED FROM ALUMINUM MONOHALIDE PRECURSORS

Samantha M. DeCarlo
Doctor of Philosophy, 2015

Directed By: Professor Bryan W. Eichhorn,
Department of Chemistry and Biochemistry

In this thesis, the synthesis, characterization and applications of aluminum compounds and cluster from aluminum monohalide solutions, AlX (where X = Cl or Br) are described. Chemistry of AlX solutions is not well understood, but AlX has proven adept at producing aluminum metalloid clusters (Al_nL_m where n>m). A brief overview of the renaissance of low-valent aluminum chemistry and select low-valent Al products is presented as background.

The neutral mononuclear aluminum tris-bpy complexes [Al(^{Me}bpy)$_3$] and [Al(^{tBu}bpy)$_3$] have been synthesized, isolated, and structurally characterized via X-ray single crystal diffraction. These complexes are the first structurally characterized homoleptic tris-bpy complexes and were studied via ESI-MS, d.c. magnetic susceptibility, electrochemical analyses. Electrochemistry demonstrates that six oxidation states are accessible from both neutral complexes: [Al(^{R}bpy)]^n (n = -3 to 3, R = Me or

tBu). The [Al(^{Me}bpy)$_3$] complex demonstrates unexpected magnetic ordering at 19 K which is not observed in [Al(^{tBu}bpy)$_3$] nor in transition metal centered tris-bpy congeners.

Synthesis, isolation, and characterization of the low-valent aluminum cluster [LiOEt$_2$]$_2$[HAl$_3$(PPh$_2$)$_6$] via NMR and ESI-MS studies are also described. These experiments proved the presence of an H atom, and developed a complete and comprehensive picture of the structure, magnetism, and spectroscopy of this compound.

Solution studies of reactions of AlBr with tBu-thiolate via ESI-MS show the formation and identification of [Al$_{17}$Br(StBu)$_{10}$S$_3$]$^{1-}$, [Al$_{10}$(StBu)$_4$S$_5$]$^{1-}$, [Al$_{13}$(StBu)$_4$BrS]$^{1-}$, and [Al$_5$(StBu)$_7$Br]$^{1-}$ in solution. The preparation and characterization of the aluminum (III) thiolate complex, Na[Al(SPh)$_4$], is also described. These studies demonstrate the importance of reaction conditions in the formation of aluminum clusters in solution, and the viability of thiolate ligands to isolate low-valent aluminum products.

Al nanoparticles (NP) can be produced from AlX solutions and have been successfully supported on both graphene and graphene oxide. The reduction of AlX solutions are quick, facile, and performed at low temperatures (-78°C). In the presence of graphene, faceted and well-dispersed graphene supported Al-NPs can be obtained.

The [AlBrNEt$_3$]$_4$ cluster is isolated from AlBr·NEt$_3$ solution and is soluble in toluene and diethyl ether. The burning rate of the hydrocarbon fuel doped with the tetramer is studied. There is an increase in burning rate attributed to the presence of [AlBrNEt$_3$]$_4$.

ISOLATION AND CHARACTERIZTION OF PRODUCTS PRODUCED FROM ALUMINUM MONOHALIDE PRECURSORS

By

Samantha M. DeCarlo

Dissertation submitted to the Faculty of the Graduate School of the
University of Maryland, College Park, in partial fulfillment
of the requirements for the degree of
Doctor of Philosophy
2015

Advisory Committee:
Professor Bryan W. Eichhorn, Chair
Professor Alan Kaufman, Dean's Representative
Professor Efrain Rodriguez
Professor Michael R. Zachariah
Professor Andrei N. Vedernikov

Foreword

“Research is what I'm doing when I don't know what I'm doing.”

---Wernher von Braun

Acknowledgements

My sincerest thanks go to my advisor Prof. Bryan Eichhorn. He took me in as a first year graduate student with a background in solid-state chemistry, and gave me the tools to become a synthetic inorganic chemist. My project had many more difficult days than easy ones, but he never stop encouraging me. He allowed me to forge my own path in this project while also being there to guide me when I faced many obstacles within my research. I always appreciate his advice, honesty, and passion for chemistry. Thank you for everything, Bryan.

I also thank all of my lab mates, past and present, from the Eichhorn research group: Dr. Chunjuan Zhang, Dr. Yang Peng, Dr. Aldo Ponce, Dr. Hao Lei, Dr. Christopher Snyder, Dr. Dennis Mayo, Dr. Domonique Downing, Dr. Yi Yu, Dr. Christopher Sims, Jonathan Senn, Aaron Geller, Kim Hyunh, Lauren Stevens, Luning Wang, and Noah Masika. Every single one of you challenged me and kept me on my toes, and made working our office and lab a great experience. I'd especially like to thank Dennis, Yang, Chris, and Lauren. Dennis and Yang you both taught me all the basics of being a synthetic inorganic chemist and how to handle this project. You also taught me to have a sense of humor about research in general and that sometimes you need to take a step back, thank you. Chris you have had an indelible mark on my scientific career, you pushed me each and every day to try something new and encouraged me to stay on when I wanted to quit. Lauren, thank you for joining this difficult project, and putting up with me as I slowly relinquished the Schnöckelator to you.

I would also like to thank Dr. Yiu-fai Lam for his assistance in all things related to NMR. I thank Dr. Peter Zavalij for running crystallography experiments on our notoriously difficult samples.

I'd also like to acknowledge my undergraduate advisor, Prof. Anne Marteel-Parrish who help set me on the path to graduate school when she asked me to do summer research for her back in 2007.

I thank the members of my incoming cohort at Maryland including Dr. Edward Sisco, Dr. Andrew Keane, Dr. Wesley Farrell, Brittany Vinciguerra, and Jason Hustedt. You all helped get me through first year and beyond. I have had a great time getting to know all of you, and am very thankful to have been surrounded by such a great group of friends.

A special thanks to my former college and current roommate Molly O'Connell who at this point is more like a second sister to me. You helped take a step back from all things chemistry to remind me that there is a world outside of lab. Your ability to deal with my extreme sarcasm and my slightly OCD tendencies make you one of the best roommates ever.

Last, but not least, I thank my family for being my greatest support; I really could have not gotten through the past five years without you. First, thanks to my Uncle Terry who always supported my academic pursuits. I thank my parents Dan and Kathleen DeCarlo for always believing in me and being there when I need them. I thank my sister Jamie for always brightening my day no matter what, and reflating my confidence when graduate school would try to crush it. Thank you all, and now its time to head onto the next adventure.

Table of Contents

List of Tables

List of Figures

Abbreviations

Å	angstrom
bpy	bipyridine
Cp	cyclopentadienyl, C_5H_5
Cp^*	Pentamethylcyclopentadienyl
Dip	Diisopropyl
Dipp	2,6-diisopropylphenyl
DMF	Dimethylformamide
e^-	electron
EDX	energy-disperse X-ray spectroscopy
EPR	electron paramagnetic resonance
Eq	Equation
ESI	electrospray ionization
Et_2O	diethyl ether
FGS	functionalized graphene sheets
GO	graphene oxide
HMDS	hexamethyldisilazane, $HN(Si(Me_3)_2)$
Hz	hertz
iPr	iso-propyl
Mes	mesityl
MFC	mass flow controller
MHCR	metal-halide co-condensation reactor
MHz	megahertz

min	minutes
mL	milliliter
mmol	millimole
MS	mass spectroscopy
nAl	Solution consisting of dispersion of Al nanoparticles
nm	nanometer
NMR	nuclear magnetic resonance
NP	nanoparticle
ORTEP	Oakridge thermal ellipsoid parameters
Ph	phenyl
ppm	parts per million
tBu	tert-butyl
TEM	transmission electron spectroscopy
THF	tetrahydrofuran
THP	tetrahydropyran
tol	toluene
XPS	X-ray photoelectron spectroscopy
XRD	X-ray diffraction
δ	chemical shift

Chapter 1: Introduction

1.1 Introduction to low oxidation state aluminum chemistry

Aluminum is one of the most abundant elements, but relatively little is understood about its chemistry outside of the thermodynamically stable states of Al^0 and Al^{3+}. The renaissance of aluminum chemistry, more specifically low oxidation-state aluminum chemistry, began in 1988, when Uhl *et al.* isolated and structurally characterized the first complex containing an Al–Al bond.[1] This complex, tetrakis[bis(trimethylsilyl)methyl] dialane, marked the beginning of a new era of aluminum chemistry exploring aluminum oxidation states between 0 and 3+. Reduced oxidation state aluminum products have the potential to yield insight into various processes including Al-metal formation, and basic elemental properties in various catalytic and energetic applications. Progress in this field has been limited due to the inherent difficulties associated with reduced oxidation state aluminum including extreme air and moisture sensitivity, low yields, and metastability of aluminum products not in the thermodynamically stable oxidation states of 0 and 3+.

A major breakthrough in low-valent aluminum chemistry was the synthesis and isolation of monovalent aluminum halide solutions (AlX; X = Cl, Br, I); the first reproducible, large-scale, low-valent aluminum starting material.[2] This material yielded a new route for production of aluminum products in reduced oxidation states (i.e. not thermodynamically stable state) not produced via traditional reductive chemistry. These solutions have produced aluminum 'metalloid clusters'. Metalloid clusters are clusters that contain more metal–metal bonds than metal–ligand bonds, and have the general formula M_nR_m (where $n > m$). AlX is a revolutionary step towards understanding aluminum on the basic level, but there is still a lot to learn about aluminum monohalide.

This thesis describes the isolation and characterization of aluminum containing products synthesized from aluminum monohalide precursors. Specifically, the study of novel complexes and clusters through the reaction of AlX with new ligand sets is highlighted. Followed by a description of the synthesis of graphene supported aluminum nanoparticles from AlX precursors, and application of a donor stabilized aluminum cluster as a soluble fuel additive.

1.2 Aluminum

Aluminum is third most abundant element on earth and comprises ≈ 8% by weight of the Earth's solid surface. Aluminum metal is extremely chemically reactive, and because of this, it is not found in its native state, but tends to form compounds with other elements. Aluminum is present in nearly 300 different minerals, and the primary ore that contains aluminum is bauxite. For most of the 19th century, extracting aluminum was an expensive process due to cost of materials and electricity, making it a 'precious' metal. In 1886, Hall and Hèroult independently developed a process in which aluminum oxide was dissolved in molten cryolite and decomposed electrolytically. This discovery made the commercial production of aluminum possible.

Aluminum metal is lightweight, ductile, and extremely inert due to an ever-present oxide layer on its surfaces making it ideal for a wide variety of uses. It is highly oxophilic and electropositive (Pauling electronegativity value of 1.61) and has a valence electron configuration of $3s^2 3p^1$. When in its oxidized form, aluminum is present in numerous compounds such as: alumina (Al_2O_3) widely used as a ceramic, methylaluminoxane ($Al(CH_3)O)_n$) a co-catalyst in the Ziegler-Natta system, and Tebbe's reagent ($Cp_2TiCH_2ClAlMe_2$) used in the methylenation of carbonyl compounds.

1.3 Aluminum Monohalide (AlX)

The thermodynamically stable solid-state binary phase between aluminum and halogens is AlX_3. In order to suppress the formation of AlX_3 and access a subvalent state, reaction conditions must be altered so that AlX will be preferentially formed. Based on the work pioneered by Timms and Skell in the 1970's, Schnöckel developed a system for the production of aluminum monohalide via a metal-halide co-condensation reactor (MHCR, discussed in section 1.3.1).[2,3] Aluminum monohalide gas is generated at elevated temperatures and reduced pressure through the reaction of aluminum and HX gas. The MHCR generates the AlX gas at approximately 1200 K under moderate vacuum (10^{-5} torr) (Eq. 1.1). The high temperature and low pressure allows for the $HX_{(g)}$ to react with molten aluminum resulting in the formation of $AlX_{(g)}$ and $H_{2(g)}$. When broken down, in high $HX_{(g)}$ concentrations AlX_3 is also formed (Eq. 1.2). However, an equilibrium is established between AlX_3 and excess molten aluminum with decreased pressure and high temperature (Eq. 1.4), resulting in the formation of more AlX, leading to the overall product formation being AlX with a small amount (<5% of $AlCl_3$).[2,4]

$$AlX_{3(g)} + 2Al_{(l)} \underset{1000^\circ C}{\overset{10^{-5} torr}{\rightleftharpoons}} 3AlX_{(g)} \quad (1.1)$$

$$Al_{(l)} + 3HX_{(g)} \xrightarrow{1000^\circ C} {}^3/_2 H_{2(g)} + AlX_{3(g)} \quad (1.2)$$

Initial studies of $AlX_{(g)}$ were performed by deposition in argon matrices. Co-condensation with an organic co-solvent matrix at 77 K allows the aluminum subhalide to be prepared on a preparative scale.[2] A MHCR has been implemented on site at the University of Maryland, the only known one of its kind in North America. As the design and maintenance of the reactor is extremely important for the generation of AlX a description of the reactor will be given here.

1.3.1 Metal Halide Co-condensation Reactor

The MHCR is a relatively simple design, with few moving parts that provides proper conditions so that the reaction outlined in Eq. 1.1 favors the generation of AlX over AlX_3. A stainless steel bell jar (30 L) acts as the reaction chamber (Figure 1.1 (A)).

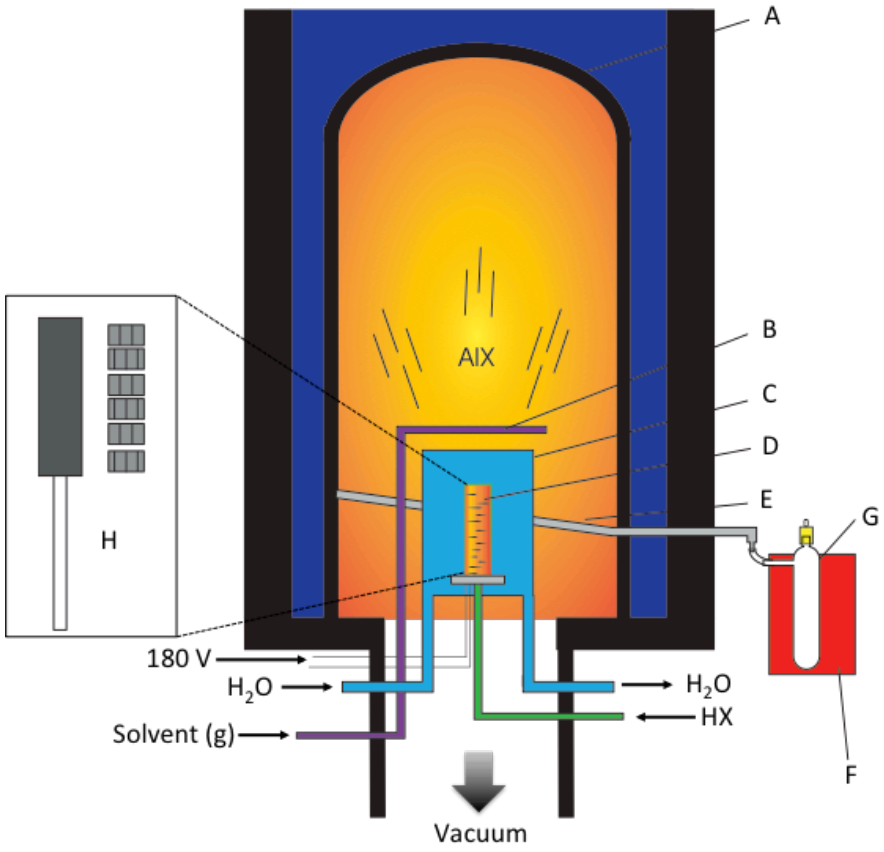

Figure 1.1. Schematic representation of a metal-halide co-condensation reactor: (a) Stainless steel bell jar (30 L) (B) Solvent input (C) Water cooling jacket (D) Resistively heated furnace (E) Drain trough (F) Cooler with dry ice (-78 °C) (G) Storage Schlenk (H) Graphite furnace pieces and graphite cells that contain aluminum (adapted from [5])

A diffusion pump is utilized to reach the necessary vacuum needed to push the reaction equilibrium to favor the production of AlX. During operation, the outer portion of the bell jar is cooled to 77 K by filling the outer steel jacket with liquid nitrogen. The bottom of the bell jar has a band heater to maintain the vacuum seal between the jar and the steel baseplate. The inner portion of the reactor consists of a resistive furnace (D) surrounded

by a water-cooled jacket (C). HX is introduced into the furnace, which contains a graphite tube filled with staggered graphite crucibles containing aluminum metal (H). The HX passes over the aluminum containing crucibles (H), allowing the necessary reaction to occur. The HX gas flow is limited via a mass flow controller (MFC). The solvent vapor that serves as the co-condensate is introduced via a stainless steel halo (B).

On average a 'run' consists of a reaction of $HX_{(g)}$ and $Al_{(l)}$ for two and a half hours. Once a run is completed the heaters are turned off, the liquid nitrogen is drained, and the chamber back-filled with ultrapure nitrogen. While the bell jar warms the AlX solvent matrix thaws down the sides of the bell jar into the internal trough (E) and out to an externally connected Schlenk vessel (G) cooled to -78°C, stored on dry ice (F). The dark solutions (typically yellow-brown for AlCl and red-brown for AlBr) and can be stored for several weeks at -80°C.

1.3.2 Parameters for optimizing Al:X ratio (1:1)

Since its implementation at UMD, two factors have been determined to be integral for optimal Al:X ratio, 1:1. The resultant metal-to-halide ratio is directly proportional to the furnace temperature (i.e. lower temperature yields $AlBr_{1.2}$ while higher temperature will yield $AlBr_{0.9}$) and inversely proportional to HX gas introduction rate (i.e. high gas rate will yield $AlBr_{1.5}$ while lower gas rate yield AlBr). Therefore, fine control of the HX gas is extremely important, and UMD is the first to outfit a MHCR with mass flow controllers (MFCs). The MFCs actively adjust gas delivery, compensating for pressure changes during a run. Even though MFCs are controlled electronically, the solenoid valves that control the unit degrade over time due to exposure to corrosive HX. To compensate for this, the outgas pressure is monitored via

thermocouple vacuum gauges. It has been determined that an increase of 10 mtorr from the starting outgas pressure is optimal for AlX generation with a ratio of Al:X close to 1:1. To provide uniform heating, the Schnepf lab, whose work centers upon generation of group 14 monohalides, have implemented use of an induction furnace in place of a resistive furnace. This uniform heating has proven to be successful in the generation of Si, Ge, and Sn subhalide solutions.[6] It is believed that a similar set-up at UMD will assist in uniform heating of the aluminum, and will help in producing Al:X, 1:1.

1.3.3 Characterization of AlX solutions

In order to experimentally determine the halide content, a Mohr titration is performed on aliquots of the AlX solution. In this direct titration method, the halide content is determined by first hydrolyzing AlX with distilled water (Eq. 1.3). A dilute potassium dichromate solution is added to the hydrolyzed aluminum aliquot, and the solution is titrated with 0.1000 M $AgNO_3$ (Eq. 1.4). First, AgX precipitates, and the endpoint of the titration is characterized by formation of red Ag_2CrO_4, indicated by a color change in solution from yellow to peach (Eq.1.5).

$$2AlX + 14H_2O \rightarrow 2[Al(H_2O)_6]^{3+} + 2HX + H_2 \quad (1.3)$$

$$HX + AgNO_3 \rightarrow HNO_3 + AgX \quad (1.4)$$

$$K_2CrO_{4(aq)} + 2AgNO_{3(aq)} \rightarrow Ag_2CrO_{4(s)} + 2KNO_{3(aq)} \quad (1.5)$$

The aluminum content of the solutions is typically determined by determining the mass loss of the Al-containing furnace assembly after reaction. In addition, the Al content is periodically measured through a back titration method. To determine the amount of Al present in solution ethylene diamintetra-acetic-acid (EDTA) is used as the titrant that will complex to Al^{3+} ions. The titration is performed in a buffered solution (pH = 5.0) with hydrolyzed AlX combined with EDTA (Eqs. 1.6 and 1.7). This solution

is boiled gently to accelerate formation of the Al-EDTA complex. Once the complex is formed indicator (xylenol orange (XO)) is added, resulting in a lemon yellow colored solution. This solution is back titrated with a standard Zn sulfate heptahydrate solution ($ZnSO_4 \bullet 7H_2O$) (Eq. 1.8). At the endpoint solution turns a light red/pink color, a result of the formation of Zn-Xylenol orange complex, $Zn(XO)^{2+}$, formed with un-complexed Zn (Eq. 1.9).

$$AlX + H_2O_{(l)} \rightarrow 2[Al(H_2O)_6]^{3+} + HX + H_2 \quad (1.6)$$

$$Al^{3+} + xs(EDTA)^{4-} \rightarrow Al(EDTA)^{-} + (EDTA)^{4-} \quad (1.7)$$

$$Zn^{2+} + Al(EDTA) + (EDTA)^{4-} \rightarrow Al(EDTA) + Zn(EDTA)^{2-} \quad (1.8)$$

$$Zn^{2+}_{(aq)} + XO_{(aq)} \rightleftharpoons Zn(XO)^{2+}_{(aq)} \quad (1.9)$$

The amount of excess EDTA titrated with zinc is related to the amount of EDTA reacting directly with Al^{3+}. Since this is a back titration method the amount of titrated excess (i.e. $Zn(EDTA)^{2-}$) formed is equivalent to the initial amount of aluminum used. Once the concentrations of both Al and halides are determined, estimation for the average Al oxidation state can be calculated.

1.4 Low-Valent Aluminum Chemistry

1.4.1 The Aluminum–Aluminum bond (Al–Al)

In 1976, Hoberg and Krause were the first to postulate that an aluminum–aluminum bond was an 'accessible structural unit in organometallic compounds.'[7] The first structurally characterized compound containing an Al–Al bond was not reported until over a decade later in 1988 by Uhl *et al.,* in the compound tetrakis[bis(trimethylsilyl)methyl]dialane ($(Al_2(C(SiMe_3)_2)_4)$). This complex was prepared through the reduction of the bis[bis(trimethylsilyl)methyl]chloroaluminum)

precursor with one equivalent of potassium metal (Scheme 1.1) resulting in a crystalline product.

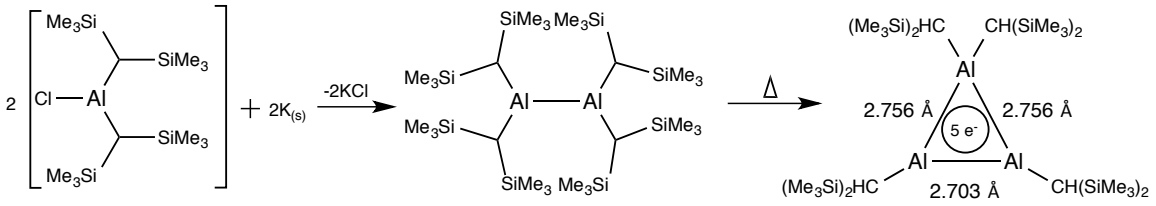

Scheme 1.1. Reduction of $Al(C(SMe_3)_2)_2Cl$ to yield $(Al_2(C(SiMe_3)_2)_4$. Heating of the dialane yields the trimer, $Al_3(CH(SiMe_3)_2)_4$.

Wiberg *et al*. later showed that heating $(Al_2(C(SiMe_3)_2)_4$ led to the isolation of a cyclotrialanyl radical, $Al_3(CH(SiMe_3)_2)_4$.[8] In 1991, Klinkhammer *et al.* isolated the icosahedral $[Al_{12}i\text{-}Bu_{12}]^{2-}$ cluster compound, produced through the reaction of diisobutylaluminum chloride with potassium metal.[9] This is the first documented example of an aluminum cluster compound, but it should be noted that it has yet to be reproduced.

1.4.2 Relationship to Boron chemistry

Although there are distinct features that make aluminum in a class of it own, there are similarities that can be drawn between low-valent aluminum and boron chemistry. Both the aforementioned dimer, $(Al_2(C(SiMe_3)_2)_4$ and the cluster $[Al_{12}i\text{-}Bu_{12}]^{2-}$ demonstrate strong similarities to their boron congeners B_2R_4 (R = OCH_3, $N(CH_3)_2$) (dimer) and $[B_{12}H_{12}]^{2-}$ icosahedron respectively.[4] When defining the similarities in bonding between the boron and aluminum clusters, it can be observed that 2–center $2e^-$ and 3–center $2e^-$ bonding occurs in the aluminum and boron structures. More specifically the $[Al_{12}i\text{-}Bu_{12}]^{2-}$ cluster is isoelectronic and isostructural to $[B_{12}H_{12}]^{2-}$ which is the classic example of a borane. The structures of boranes cannot be predicted by Lewis

structures, but are successfully described by Wade's rules, which correlate the number of electrons in a system to the shape of the borane. A summary of these rules are listed in Table 1.1.[10]

Table 1.1. Wade's Rules for the Boranes (adapted from [10])

Type	Formula	Skeletal e^- Pairs	Borane Examples
Closo	$[B_nH_n]^{2-}$	n + 1	$[B_6H_6]^{2-}$, $[B_{12}H_{12}]^{2-}$
Nido	B_nH_{n+4}	n + 2	B_2H_6, B_5H_9, B_6H_{10}
Arachno	B_nH_{n+6}	n + 3	B_4H_{10}, B_5H_{11}
Hypho	B_nH_{n+8}	n + 4	None

The term deltahedra are used to describe these triangular-faced structures and are characterized by the number of vertices, *n*, present in the structure as well as the number of cluster-bonding electrons present. In Wade's rules the electrons present in the framework, also referred as the 'skeleton', of the cluster are referred to as skeletal electrons. Following Wade's rules, boranes of the structure $[B_nH_n]^{2-}$ have a *closo* deltahedral structure. In these structures there is a boron atom at each vertex and no bridged B–H–B bonds in the complex. The icosahedral structure $[B_{12}H_{12}]^{2-}$ falls under this description. A *closo* structure possess n +1 framework electron pairs, and $2n$ + 2 skeletal bonding electrons. The number of electrons is derived as follows:

- Each $[B_nH_n]^{2-}$ cluster has a total electron count of $4n$ + 2 (each B = $3e^-$, each H = $1e^-$, charge = $2e^-$).
- This electron counts equates to $2n$ + 1 total bonding pairs.
- *Closo* boranes exclusively contain terminal B-H bonds, and thus n bonding pairs are required for these bonds.
- Therefore, n + 1 of the bonding pairs remain to form delocalized bonds within the cluster frameworks, giving $2n$ + 2 skeletal bonding electrons.

Since Klinkhammer's $[Al_{12}i\text{-}Bu_{12}]^{2-}$ is isoelectronic to $[B_{12}H_{12}]^{2-}$ following Wade's rules it can be defined as a *closo* structure with 26 skeletal bonding e^- .

1.4.3 Isolating compounds contaning Al–Al bonds via reductive methods

Traditional reductive methods, as mentioned above, have been successful in the isolation and characterization of compounds that contain Al–Al bonds. Results of this methodology are fairly limited, when compared to the reductive chemistry of other compounds containing metal–metal bonds. The relative instability of +1 and +2 oxidation states of aluminum relative to the 0 and +3 states contributes to the dearth of results. These traditional reductive methods when applied to aluminum chemistry often leads to the deposition of metallic aluminum, but when performed in the presence of ligands with high steric bulk, low-valent aluminum complexes can be isolated. It is believed that the bulky ligands kinetically stabilize the Al-compounds with regards to thermal decomposition. These compounds have been garnering interest due to the unusual oxidation state of aluminum, their high-energy output, and general insight that they yield into the general chemistry of aluminum.

Cui *et al.* utilized a bulky diaryl beta-diketiminate (Nacnac) ligand to prepare a monomeric, donor-free aluminum (I) compound LAl (L= $[CH(CMeNAr)_2]$, Ar =2,6-*i*-$Pr_2C_6H_3$)[11]

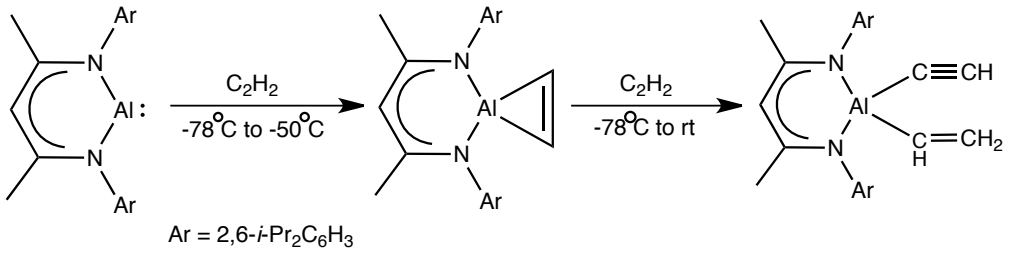

Scheme 1.2. Reaction of LAl with acetylene at low temperature (adapted from [4])

In the reduction the diiodide aluminum (III) precursor [LAl]I_2 with potassium metal, LAl is prepared in moderate yield. The resulting compound contains an aluminum-based electron lone pair analogous to that of a carbene (Scheme 1.2). Diketiminatoaluminum, LAl, reacts with acetylene at low temperature to afford the first stable aluminacyclopropene. Reaction with a second equivalent of acetylene produces an Al^{3+} product which contains –C(H)=CH_2 and C≡ CH functional groups (Scheme 1.2).[12,13]

The bulky terphenyl ligand system has also been shown to stabilize low-valent transition metal and main-group elements and promote metal-metal multiple bonding. Reaction of Ar'AlI_2 (Ar' = C_6H_3-2,6-(C_6H_3-2,6-*i*–Pr_2)$_2$) with sodium metal theoretically yields dialuminene Ar'Al=AlAr' species (it has not been structurally characterized). Treatment of the dialuminene with toluene yields a [4+2] Diels-Alder cycloaddition product; while treatment of the dialuminene with excess sodium metal results in a 'triply-bonded' 'dialuminyne' compound Na_2[Ar'AlAlAr'] (Figure 1.2). The interaction of the 'dialuminyne' compound and the sodium cations plays a role in a short Al–Al bond, and calculations show that effectively this complex had an Al≡Al triple bond.[14]

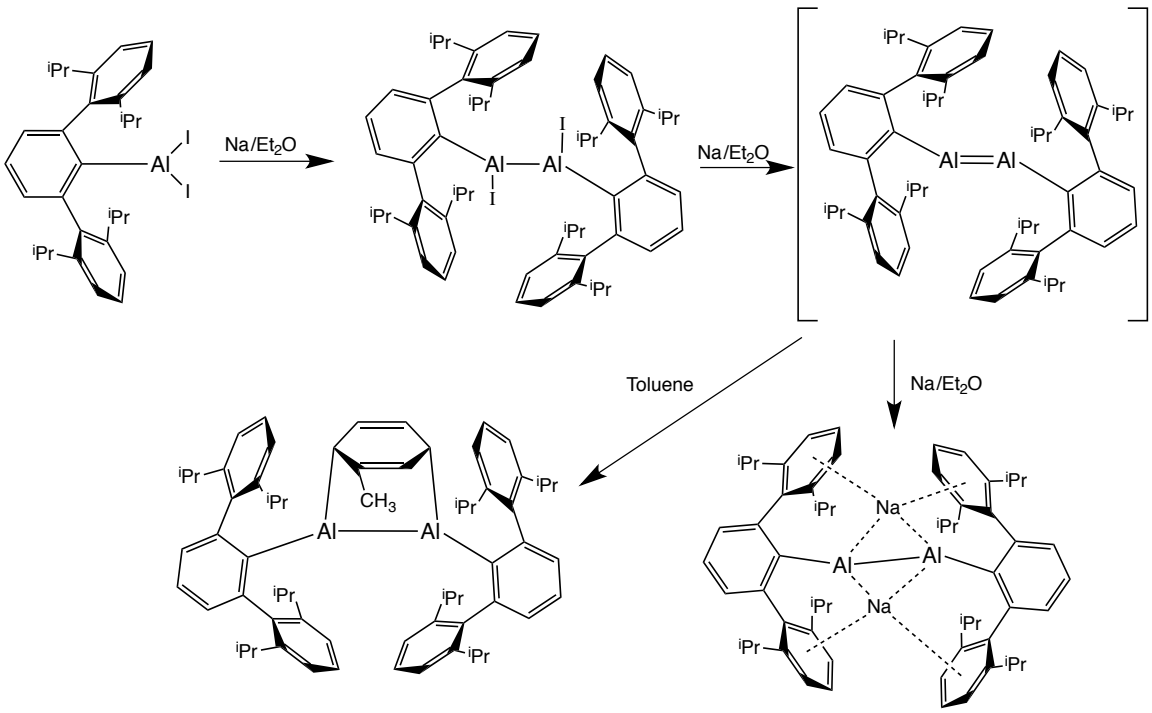

Figure 1.2. Reduction chemistry of terphenylaluminum diiodide compound, adapted from [14].

When the same reduction is performed on the modified Ar"AlI_2 (Ar"= C_6H_3-2,6-(C_6H_3-2,6-(C_6H_2-2,4,6-Me_3)$_2$)), a three-atom aluminum cluster, Na_2[Ar"Al]$_3$ is isolated. This complex will be further discussed in Chapter 3.

Traditional approaches have also yielded a large number of Al^{2+} dimers that do not contain bridging ligands. Ligands used have included Si(*t*Bu)$_3$, C_6H_2-2,4,6-*i*Pr$_3$, C_6H_3-2,6-Dipp$_2$ (Dipp = C_6H_3-2,6-*i*Pr$_2$), C_6H_3-2,6-Mes$_2$, and Cp^*.[15-17]

Jones' dimeric Mg^{I}–Mg^{I} compound, $[\{(^{Mes}Nacnac)Mg\}_2]$ ($^{Mes}Nacnac$ = $[(MesNCMe)_2CH]^-$, Mes = 2,4,6-trimethylphenyl) has also been used to reduce Al(III).[18] Specifically, the dimer reacts with alane derivatives: $IPr{:}AlH_3$ (IPr=:C{$(DippNCH)_2$}, Dipp = 2,6-diisopropylphenyl) and $[(Priso)AlH_2]_2$ (Priso = *i*-$Pr_2NC(NDipp)_2$). These reactions form the ligand-stabilized dialane compound $(Dipp{:}AlH_2)_2$ and $(PrisoAlH)_2$ (Scheme 1.3).[18]

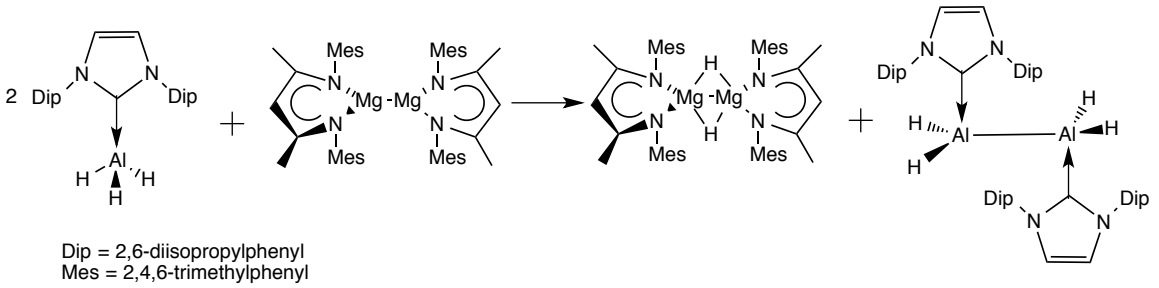

Scheme 1.3. Reaction scheme illustrating the transfer of hydrogen between aluminum(III) and magnesium(I) complexes. Transfer of hydrogen form $[AlH_3(IPr)]$ to $[(^{Mes}Nacnac)Mg]_2$ yields $[(^{Mes}Nacnac)Mg(\mu\text{-}H)]_2$ and the dialane complex $[(Ipr)(H)_2Al]_2$, adapted from [18].

These reactions are noteworthy as they represent the first synthesis of an aluminum (II) hydride compound.

While traditional methods of chemically reducing Al(III) precursors to form low oxidation state Al complexes have given a number of new compounds, they are limited in the scope of products that they can afford. In order to increase the nuclearity of the aluminum within the products, our research has focused on the utilization of aluminum monohalide solutions as a starting material. These solutions have been shown to be adept at yielding unique high nuclearity aluminum clusters.

1.5 Chemistry of AlX solutions and formation of low-valent products

The stability of AlX solutions is extremely dependent on the solvent systems used during formation of the solution. It has been found empirically that a mixed-solvent system containing an aromatic hydrocarbon (toluene or xylene) and a Lewis-donor solvent create solutions that are metastable with respect to disproportionation at -78°C for a few weeks. The Lewis donors that are commonly used as donor co-solvents include Et_2O THF, and NEt_3.

These metastable AlX solution undergo disproportionation reactions to form the thermodynamically stable products of aluminum metal and aluminum trihalides at temperatures greater than -78°C (Eq. 1.10).

$$3AlX \xrightarrow{\Delta} AlX_3 + 2Al^0 \qquad (1.10)$$

In order to synthesize metalloid clusters, anionic ligands are added to drive salt metathesis reactions, theoretically producing AlR species and a halide salt. This low temperature metathesis and subsequent thermal disproportionation process to give Al_xR_y (where x > y) metalloid clusters is known as the "Schnöckel method" (Figure 1.3 D).

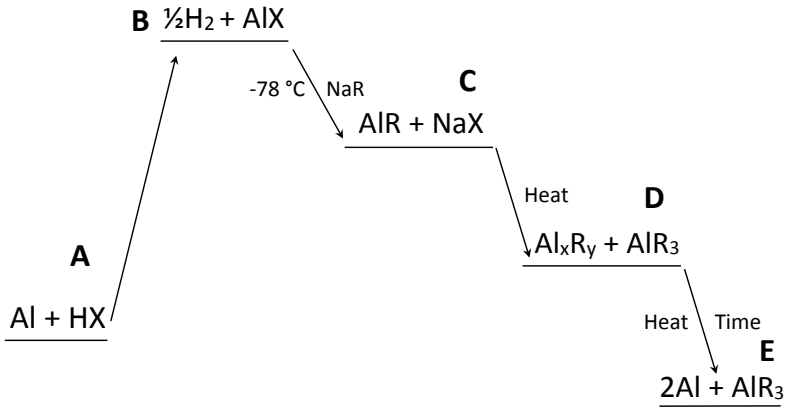

Figure 1.3. Generation (A→B) of metal monohalide followed by stepwise disproportionation of MX solution upon reaction with sodium salt (NaR) (C). The goal is to 'capture' the ligand stabilized aluminum cluster (C→D**)** before complete disproportionation to Al^{3+} and bulk metal (Al^0) (E).

There are multiple factors that contribute to the disproportionation reactions of the AlX solutions, which include the elemental makeup of the subhalide used, the solvent mixture used during co-condensation, the temperature of the co-condensation reaction (and consequently the metal-to-halide ratio), the temperature and order of reactant combination, and the crystallization methods.

The 'Schnöckel' route has resulted in the isolation of various aluminum clusters, including the first organo-Al^{I} compound $[AlCp^{*}]_4$.[19] Specifically, this route has produced several 'metalloid clusters', some of which are listed Table 1.2.

Table 1.2. Metalloid cluster compounds of aluminum[a]

Formula	Al Atoms	Average Ox. State	Ref.
$[Al_7(HMDS)_6]^-$	7	0.714	20
$Al_7N[Me_2SiPh]_6$	7	0.857	21
$K_8Al_{12}(OtBu)_{18}$	12	0.833	22
$[Al_{14}I_6(HMDS)_6]^{2-}$	14	0.714	23
$Si@Al_{14}Cp^*_6$	14	0.428	24
$Si@Al_{14}(N(Dipp)TMS)_6$	14	0.428	25
$Al_{22}Cl_{20}L_{12}$ (L = THF or THP)	22	0.909	26
$Al_{22}Br_{20}(THF)_{12}$	22	0.909	27
$Al_{20}Cl_{10}Cp^*_8$	20	0.900	28
$Al_{20}Br_{10}\ Cp^*_8$	20	0.900	28
$Al_{50}Cp^*_{12}$	50	0.240	29
$SiAl_{14}R_6$ (R = Cp^* or N(Dipp)TMS)	14	0.429	25
$Si@Al_{56}[N(dipp)TMS]_{12}$	56	0.214	30
$[Al_{69}(HMDS)_{18}]^{3-}$	69	0.217	31
$[Al_{77}(HMDS)]_{20}]^{3-}$	77	0.221	32

[a]Cp^* = η^5-C_5Me_5; Dipp = C_6H_5-2,6-$^{i}Pr_2$; THP = Tetrahydropyran

The clusters are often viewed as structural models for the formation of bulk Al metal. Known examples of Al metalloid clusters have metal atom cores that closely resemble that of bulk Al metal. Within the aluminum metalloid cluster the bonding of Al–Al distances range between 2.5 and 3.0 Å.

1.5.1 Effect of Reaction Conditions on Cluster Growth

The size of the Al_n cluster core is determined by the reactivity of the AlX solution with respect to disproportionation.[19] For a particular aluminum monohalide solution the size of the resulting clusters should be tunable by varying reaction conditions such as temperature. Reactions of AlX and HMDS perfectly illustrate how varying the reaction conditions can isolate metalloid clusters of differing aluminum nuclearity.

The smallest example of an isolated Al metalloid cluster, and the first in the HMDS series of Al clusters is $[Al_7(HMDS)_6]^{1-}$.[20] This compound is formed during the reactions of $AlCl{\bullet}Et_2O$ with Li(HMDS) at -7 °C, which contains one central naked aluminum atom contained inside a distorted aluminum octahedron (Figure 1.4).

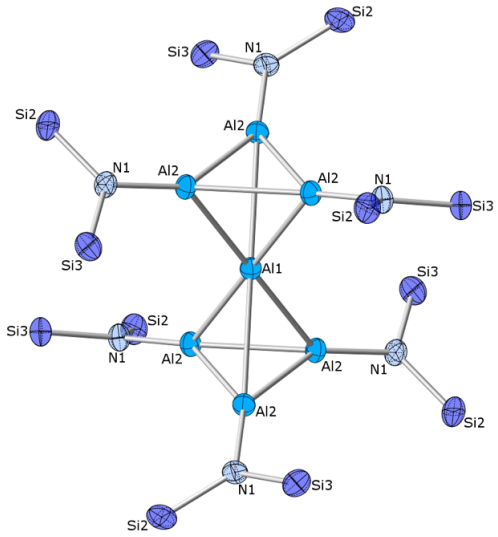

Figure 1.4. Crystal structure of $[Al_7(HMDS)_6]^{1-}$ thermal ellipsodes shown at 50% probability, C and H have been omitted for clarity. Data from reference [20].

The central aluminum atom can be described is 'capped' with two $Al_3(HMDS)_3$ units (distance Al1–Al2 = 2.737 Å) . The Al_3 units are staggered with respect to one another (Al2–Al2 = 2.540 Å) and each Al in the Al_3 unit is bound to an HMDS ligand (Al2–N = 1.844) Å). The average oxidation state aluminum within the cluster is +0.71.

The bond distances are shorter than those in bulk aluminum metal (2.863 Å) highlighting the covalent nature of the Al bonds in the cluster and their lower coordination numbers.

The Al_7 structural unit is particularly stable and three substituted versions of the disilazide ligand have produced Al_7 clusters of the formula $[Al_7(N(SiMe_2R)_2)_6]^-$ (where R = hexyl, butyl, isopropyl).

When the same reaction, $AlCl{\bullet}Et_2O$ reacts with Li(HMDS), is performed at room temperature, the reaction yields an $[Al_{12}HMDS_8]^{1-}$ cluster (Figure 1.5).

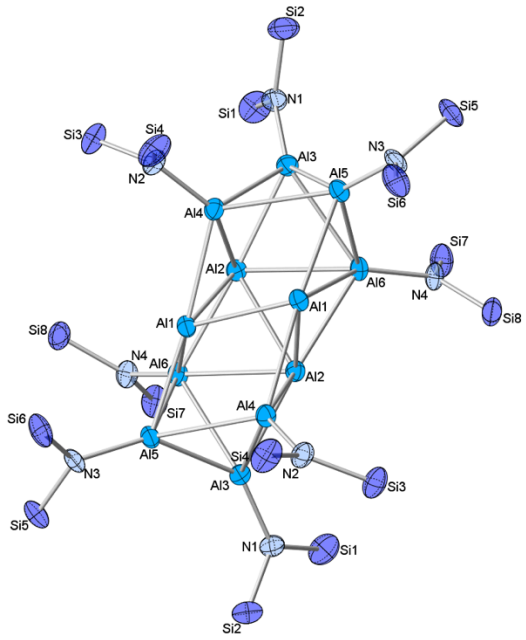

Figure 1.5. Crystal structure of $[Al_{12}(HMDS)_8]^-$, thermal ellipsoids depicted with 50% probability from reference [33], C and H have been omitted for clarity. Select Al–Al bond lengths: Al1–Al6 = 2.722 Å, Al6–Al5 = 2.757 Å, Al1–Al5 = 2.597 Å, Al5–Al3 = 2.542 Å, Al3–Al4 = 2.762 Å, Al2–Al1 = 2.679 Å, Al1–Al4 = 2.687 Å, Al4–Al2 = 2.719 Å, Al3–Al2 = 2.610 Å, Al1–Al1 = 2.630 Å.

In this cluster the average aluminum oxidation state is 0.58+. Within the cluster the Al atoms form either 4 or 6 bonds to other Al atoms, and eight of the Al atoms are bound to HMDS ligands (Al–N = 1.848 Å). The Al–Al bond lengths range from 2.598–

2.762 Å, averaging to = 2.652 Å, and are slightly longer than the bond lengths observed in $[Al_7(HMDS)_6]^{1-}$.

The two prototype Al metalloid clusters, $[Al_{69}(HMDS)_{18}]^{3-}$ and $[Al_{77}(HMDS)_{20}]^{2-}$, are prepared from similar reactions but at higher temperatures. A reaction of $AlCl•Et_2O$ with Li(HMDS) to 60 °C yields $[Al_{69}(HMDS)_{18}]^{3-}$ [31] (average Al oxidation state = + 0.217) whereas heating the reaction at 60 °C for a full week yields $[Al_{77}(HMDS)_{20}]^{2-}$ (average Al oxidation state = + 0.221) (Figure 1.6 a & b). The structures of these two clusters are fairly similar. Both contain a central Al atom surrounded by an icosahedral shell of 12 Al atoms, which are also coordinated by 9 atoms.[31] The two structures begin to differ beyond this core. In the Al_{69} cluster the next shell consists of 38 Al atoms, followed by an outer shell of 18 Al atoms (Figure 1.6 a & c).[31] For the Al_{77} structure, the outer most shell consists of 20 Al atoms and the second shell consists of 44 Al atoms (Figure 1.6 b & d).[31]

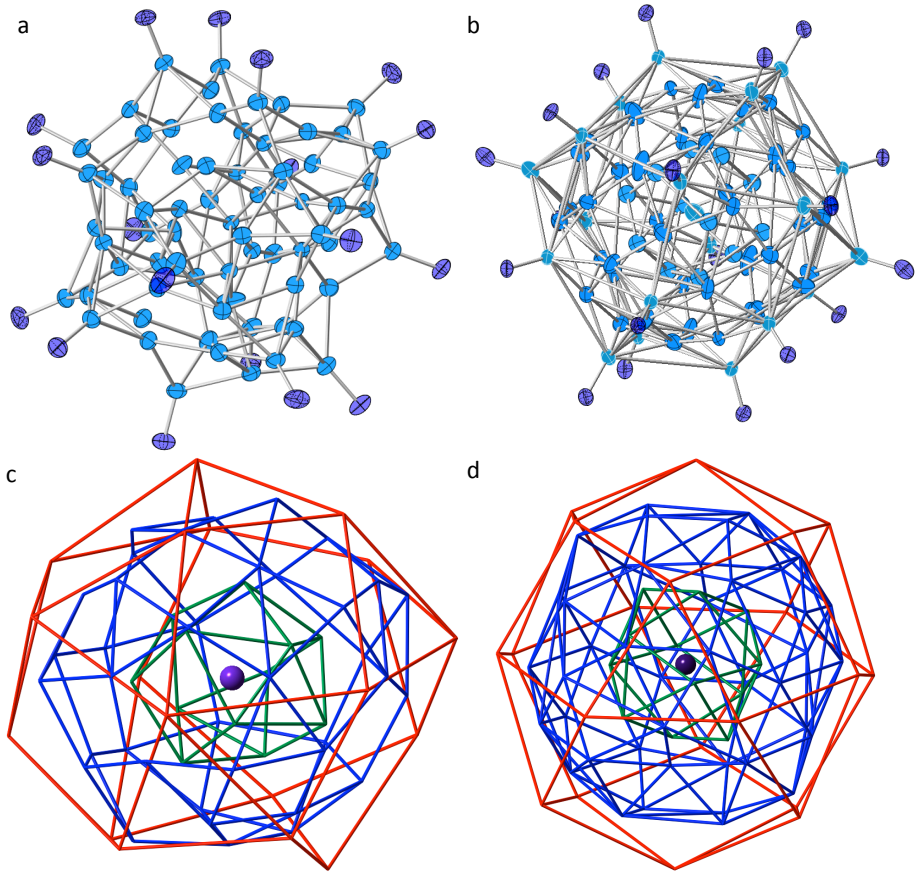

Figure 1.6. Comparison of the arrangement of Al atoms in Al_{69} and Al_{77} cores thermal ellipsoids depicted at 50% probability (a) $[Al_{69}(HMDS)_{18}]^{3-}$ (b) $[Al_{77}(HMDS)_{20}]^{2-}$ (Al = light blue, N = dark blue (C, Si, and H omitted for clarity)); Shell views of the two structures: (c) $[Al_{69}(HMDS)_{18}]^{3-}$ (d) $[Al_{77}(HMDS)_{20}]^{2-}$ (Purple = central Al, Green = Al_{12} (icosahedron, 1st shell), Blue = 2nd shell, Red = 3rd (outer shell))[31,34]

Reactions of HMDS with the less reactive AlI yields a partially substituted $[Al_{14}(HMDS)_6I_6]^{2-}$ [23] while brief heating of the reaction leads to the formation of $[Al_{77}(HMDS)_{20}]^{2-}$. The Al_{14} cluster is described as a nano-wheel structure; the main structural unit is two staggered, Al-centered, Al_6 rings (Figure 1.7).

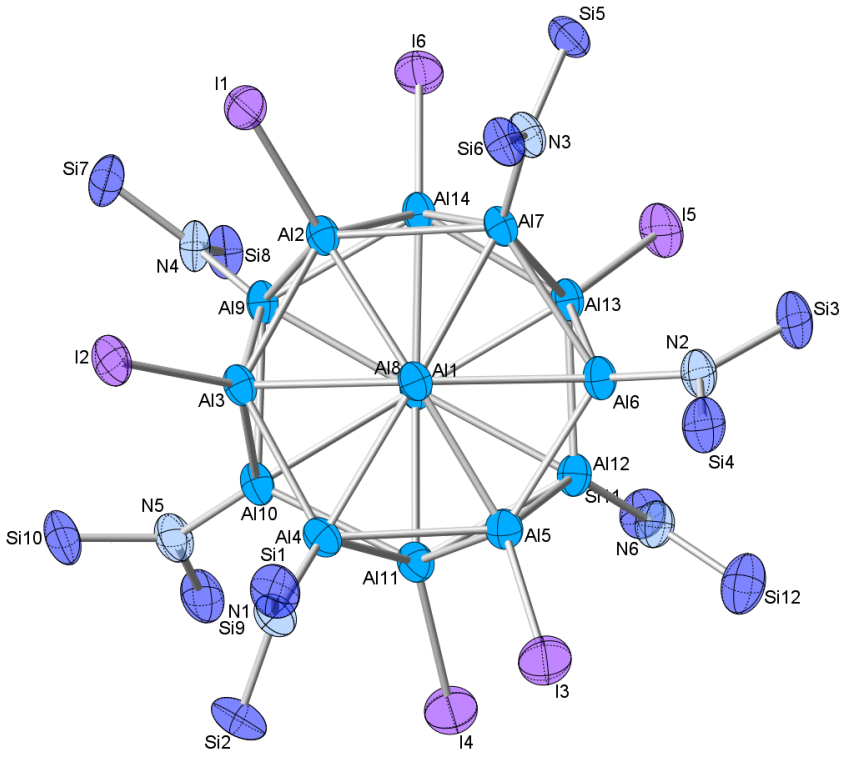

Figure 1.7. Molecular structure of $[Al_{14}(HMDS)_6I_6]^{2-}$, thermal ellipsoids depicted with 50% probability, H and C atoms omitted for clarity (taken from reference [23]).

The central Al-atoms (Al1 and Al8) in the rings deviate slightly from the plane of the rings and are separated by 2.728 Å. The other Al–Al distances range from 2.570 Å (between Al atoms with iodide ligands) to 2.910 Å (between Al atoms with HMDS ligands).

The metalloid aluminum clusters favor arrangement of close packing of the atoms, reminiscent of aluminum metal. Distortions from bulk aluminum metal FCC packing reflect the adaption of the cluster to be more molecular in nature.[14]

1.5.2 Donor/Halide Stabilized Metalloids

Disproportionation of the AlX solutions, in the absence of alkali salts, has led to the formation of aluminum subhalides, $Al_{12}[Al_{10}X_{20}D_{10}]\cdot D_2$ (where X = Cl, and D = THF, THP,[26] or X = Br and D = THF[27]), which contain two aluminum 'shells' (inner = Al(1), outer =Al(2)). The interior shell is an icosahedron of twelve aluminum atoms and is surrounded by an outer shell of ten $[AlX_2\cdot D]$ moieties (Figure 1.9a). The interior icosahedron is compressed along the C_5 axis similar to the $B_{10}C_2$ icosahedron in the *para*-carborane (refer to section 1.4.2) $B_{10}C_2(CCl_2H)_{10}\cdot 2H$ (Figure 1.8).[35]

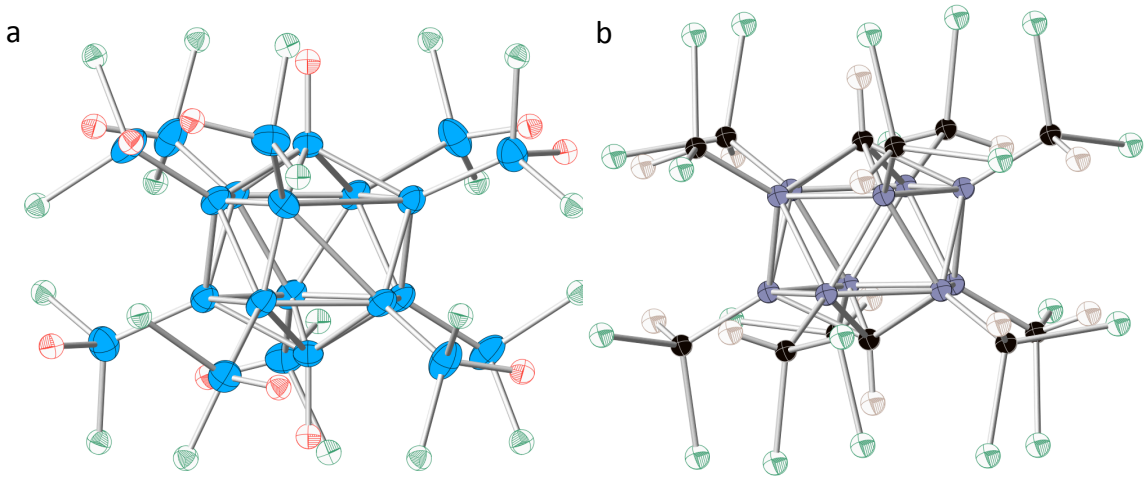

Figure 1.8. Side-by-side comparisons of *para* crystal structures of (a) $Al_{12}[Al_{10}Cl_{20}(THF)_{10}]\cdot(THF)_2$ (Al = light blue, Cl = green, O = red, C and H omitted for clarity) (b) $B_{10}C_2(CCl_2H)_{10}\cdot 2H$ (B = purple, C = black, Cl = green, H = pink) (taken from references [26,35]).

In the icosahedron the Al(1)–Al(1) bonds average 2.71(7) Å and the bonds from the inner shell to the outer shell (Al(1)–Al(2)) bonds average 2.55(2) Å. The related metalloid clusters $Al_{20}Cp^*_8X_{10}$ (X= Cl or Br) also have an inner Al_{12} icosahedron core with average Al(1)–Al(1) = 2.68(4) Å and Al(1)–Al(2) = 2.53(3) Å.[28]

1.5.3 Relationship of metalloid clusters and nanoparticles

Metalloid clusters essentially bridge the gap between large molecular clusters and small NPs, yielding insight into the process of NP growth; which is still poorly understood despite being a well-researched area in chemistry and engineering.[36] Clusters are in a position of size and regularity where they can be characterized by the same means as molecules (i.e. X-ray crystallography). These clusters can posses high coordination numbers and will give 'NP-like' structures.

The synthesis of small, uniform NPs can be promoted by the synthesis of relatively stable clusters. Such materials can be synthesized if close packed structures are synthesized, which promotes maximum metal-metal bonding and therefore maximizes cluster stability.[37,38] The regular packing of metal atoms around a central atom gives the cluster a regular form adopting a full shell when a magic number of atoms is present in the shell of a cluster. Such magic clusters can be represented by M_x where the number of atoms in each shell, *y*, is defined by (Eq. 1.11):

$$y = 10n^2 + 2 \qquad (1.11)$$

where *n* is the number of shells in the cluster. Each magic cluster contains *x* metal atoms where *x* is the sum of the atoms in each shell and the central atom. The fist magic cluster therefore contains the central atom and 12 surrounding atoms to give the magic number M_{13} (1+12). Based on equation 1.11, the second magic cluster has 42 atoms in the second shell, yielding a total of 55 metal atoms (42+13).[39] There are examples of aluminum metallic clusters with ligands have been synthesized with full shells such as: $SiAl_{56}(N(SiMe_3)Dipp)_{12}$ (Dipp =C_6H_3-2,6-*i*Pr_2), $[Al_{69}(HMDS)_{18}]^{3-}$, and $[Al_{77}(HMDS)_{20}]^{2-}$.[5] In these examples the innermost atoms demonstrate the proclivity for the M_{13} formation, a central atom surrounded by 12 atoms.

Although there is a limited number of aluminum clusters found, Schnöckel *et al.* have documented a continuum of cluster sizes from 4 up to 77 aluminum atoms; the latter of which approaches the nm range of measurement. The ability to characterize these discrete clusters has provided great insight into the rearrangement of aluminum atoms as they form the metallic phase. The relationship of the metalloids produced from AlX and bulk aluminum metal makes aluminum monohalide a logical precursor for Al-NP generation.

1.6 Aluminum nanoparticles

Aluminum NPs are widely studied due to the fact that aluminum has high energy density in terms of volume and mass, and its high abundance and low cost. There are a variety of methods in the literature describing the synthesis and isolation of aluminum nanoparticles (NPs). These include: evaporation-condensation method,[40,41] laser ablation,[42,43] arc discharge,[44] mechanochemical synthesis (i.e. ball milling),[45] exploding wire experiments,[46,47] titanium-catalyzed decomposition of alanes[48] and liquid phase methods employing chemical or electrochemical reduction methods.[49-51] Problems that often plague these routes are relatively large sized particles, large standard deviation of particle size, agglomeration of the particles, and an inherent oxide layer present on Al NPs. Controlling the size and stoichiometry of NPs is critical in nanoscience because the various characteristics of the solid-state materials (e.g. magnetic, catalytic, optical) are highly composition, structure, and size-dependent.[52] Monodisperisity among NPs is therefore crucial in eliciting consistent, uniform chemical and physical properties. The structure and shape of the particles affect their functionality in applications, therefore controlling the size of a particle and the uniformity in a sample of particles is important.

A way to overcome some of issues the issues plaguing Al-NPs synthesis is to support the Al-NPs on graphene. It has been calculated that AlX is adept at adhering to graphene, particularly where there are defects, to yield sites for NP growth.[53] These calculations help direct experiments in our lab and it has been found that well-dispersed, relatively uniform, faceted Al NPs do grow on graphene when AlX is used as the aluminum source (Chapter 5). The formation of small, uniform, discrete NPs is important for their potential application for in energetic materials.

It has been theorized that another viable alternative in overcoming rapid agglomeration effects of Al-NPs is the use of molecular scale aluminum clusters produced via the Schnöckel route in place of NPs. The outer layer of these clusters are stabilized with organic based ligands in place of the traditional oxide shell found on Al-NPs. [54] This means that these clusters may behave differently than their nanoparticle counterparts. It has been found in simulations that ligand/oxygen interactions are minimal and show no evidence of initial loss of aluminum ligand units.[55] The oxygen preferentially diffuses through the outer steric barrier of the ligand, split into atomic oxygen after coming into contact with the aluminum cluster, and forms product similar to Al_2O_3.[55] The materials produced via the Schnöckel route are unique candidates for use as additives in fuels due to the lack of an inherent oxide shell combined with the reduced oxidation state of aluminum, and may prove to be useful in increasing energetic output in fuels, and could ultimately surpass those fuels that use Al-NPs as an additive.

1.7 Overview of the thesis

In the remainder of the thesis, the synthesis and characterization of products produced from AlX solutions will are described. The synthesis and characterization of

Al^{3+} complexes $[Al(^{R}bpy)_3]$ (R= Me or tBu) will be described in Chapter 2. Chapter 3, will focus on the isolation and characterization of the $[LiOEt_2]_2[HAl_3(PPh_2)_6]$ trimeric cluster. In Chapter 4 reactions involving AlX solutions and thiolate ligands will be discussed. Chapter 5 focuses on the fabrication of Al nanoparticles supported on both graphene and GO, and the characterization of the materials via TEM and XRD spectroscopy. Lastly, Chapter 6 highlights the use of an aluminum cluster $[AlBrNEt_3]_4$ as an additive in a hydrocarbon fuel.

Chapter 2: The isolation and characterization of $[Al(^{R}bpy)_3]^0$ (R = Me or tBu)

2.1 Introduction

The 2,2'-bipyridine (bpy) ligand and its derivatives are some of the most commonly used bidentate nitrogen donor ligands in coordination chemistry (Figure 2.2a).[56] Its widespread use stems from its commercial availability and its propensity to form stable 5-member rings by coordinating in an N, N' fashion to main group, transition, and f-block metals.[56] In the past 50+ years, bpy coordination complexes have been extensively studied, including the $[M(bpy)_3]^n$ homoleptic tris-bpy complexes (M = transition metal, n = -3 to +3)[57-60] that include the well-known $[Ru(bpy)_3]^n$ series.[57,61] Interest in these complexes resides in their propensity to form helical assemblies, chiral molecular recognition properties, luminescent behavior devices, and unique electrochemical behavior that is often characterized by multiple accessible oxidation states.[56] These studies also revealed the redox-active nature of the bpy ligand and the extent of its 'non-innocence'. Wieghardt *et al.* have performed extensive studies of many structurally characterized homoleptic tris-bpy complexes and delineated the important diagnostic role that the C1–C1' intrachelate bonds have in identifying the redox state of the bpy ligand in these complexes.[56,58] The C1–C1' bond length can be used to differentiate between neutral, monoanionic, and dianionic bpy ligands (Figure 2.1), which can then be used to determine the oxidation state of the metal center. This analysis is applicable to both substituted and non-substituted bpy ligands.[58,60,62] For example the C1–C1' intrachelate bond length of 4,4'-substituted bpy ligands is a reliable indicator of oxidation states for those complexes that have been structurally characterized.[60]

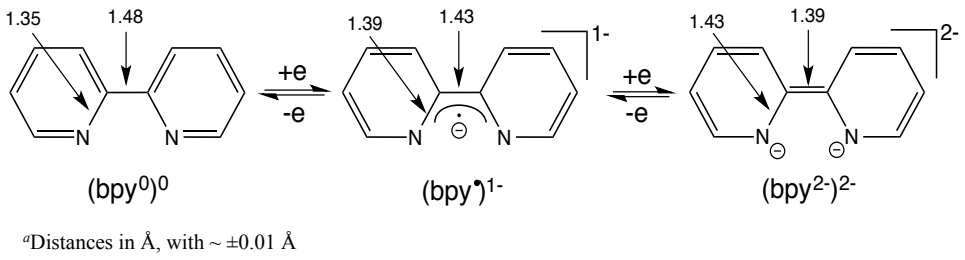

[a]Distances in Å, with ~ ±0.01 Å

Figure 2.1. Oxidation levels of bpy ligand, and relevant average crystallographically determined bond distances[a] adapted from reference [62])

Previous studies employing this analysis have been focused on transition metal bpy complexes, however, a DFT study of group 14 metals demonstrates that analogous bond length trends should also be exhibited in the group 14 bpy complexes.[63] The accuracy of the utilization of the intrachelate bond for oxidation state assignment has been further reinforced by the structural characterization of, $[Ga(bpy)_3]^{3+}$. As an example, the analysis of the $[Ga(bpy)]^{3+}$ complex indicates the presence of three neutral bpy ligands bound to a Ga^{3+} metal ion (Table 2.7).[64]

This structural analysis, coupled with DFT calculations, has been used to identify the oxidation states of the ligands and metals in a variety of the bipyridine complexes.[56,58,60,62] As a result, interpretation of the magnetometry, electrochemistry, and various spectroscopic methods of these complexes has been significantly advanced. These couplings of physical property measurements, structural studies (when available), and DFT calculations have facilitated oxidation state assignments for most of the known homoleptic tris-bpy complexes.

In contrast to the large number of transition metal tris-bpy complexes there are few examples of main-group metal tris-bipyridine complexes reported in the literature. The only example of a structurally characterized Group 13 homoleptic tris-bpy complex, $[Ga(bpy)_3]^{3+}$, was first described by Jones *et al.* in 2004.[64] Group 3 $[Sc(bpy)_3]^0$ and group

14 $[Si(bpy)_3]^n$ (where n = 4+ to 1+) have been described but not structurally characterized.[63,65] One hepta-coordinate tris-bpy complex of the thallium, $Tl(bpy)_3(dmso)$, has been prepared and crystallographically characterized.[66] Homoleptic aluminum tris-bpy, $[Al(bpy)_3]$ **(2.3)**, has also been described and characterized through calculations and magnetrometry but the crystal structure is not known.[62,67,68] The original report of **2.3** assigns an Al^0 center with neutral bpy ligands, but subsequent computational and spectroscopic studies suggest that the complex contains an Al^{3+} center coordinated by three monoanionic bpy ($[bpy^{\bullet}]^-$) ligands.[67] DFT calculations show a symmetrical D_3 structure with an S = $^1/_2$ ground state and an S = $^3/_2$ excited state that is only slightly higher in energy. This finding is in support of magnetrometry experiments performed from Horiba *et al.* showing the presence of three unpaired electrons at room temperature.[62]

There are numerous examples of neutral homoleptic tris-bpy complexes with various metal and ligand oxidation states (see Table 2.1), but relatively few have been structurally characterized. In contrast, many homoleptic tris-bpy metal complexes using the 4,4'- substituted bpy ligands, $R_2C_{10}H_6N_2$ (^{R}bpy where R= Me_2 or $^tBu_2$), Figure 2.2b, have been crystallographically characterized (see Table 2.2).

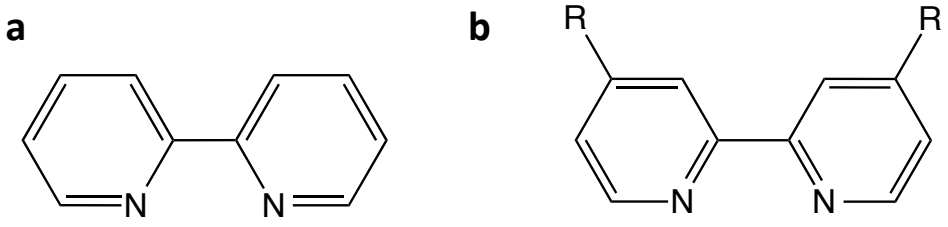

Figure 2.2.(a) 2,2'-bipyridine, bpy, ($C_{10}H_8N_2$) (b) 4,4'-di-R-2,2'-bipyridine, ^{R}bpy

Surprisingly, there is little data correlating structural and physical properties of the main group $[M(bpy)_3]^n$ complexes, and their relationships to the transition metal complexes remains to be firmly established. Here we describe the synthesis and characterization of the first structurally characterized aluminum homoleptic tris-bpy complexes $[Al(^{tBu}bpy)_3]$ **(2.1)** and $[Al(^{Me}bpy)_3]$ **(2.2)**. Both of these complexes were synthesized through the use of our unique starting material aluminum monohalide (AlX) solution where aluminum is in the 1+ oxidation state.[2] Structural, electrochemical, electrospray ionization mass spectrometry (ESI-MS), and magnetometry studies have been performed on both **2.1** and **2.2** and are described in detail. These studies show that the substituted bpy ligands in **2.1** and **2.2** are monoanionic and are best described as $[Al^{3+}(^{R}bpy^{\bullet})_3]$ complexes. Magnetometry experiments show that three unpaired electrons located on the ^{R}bpy ligands and are antiferromagnetically coupled to give S = $^1/_2$ ground states with low lying S = $^3/_2$ excited states that are populated above 110 K **(2.1)** and 80 K **(2.2)** in the solid state. In contrast to the solid-state behavior $M(bpy)_3$ complexes reside in their S = $^1/_2$ ground state at room temperature in CH_3CN solutions. Complex **2.1** shows unusual 3D antiferromagnetic interactions below 80 K in the solid state. Solution based experiments show 3 nearly-reversible ligand based oxidations and 3 quasi-reversible ligand based reductions.

Table 2.1 Selected homolepetic tris-bpy complexes [a]

Complex[b,c]	Structurally Characterized?	Ref.
$[Al^{III}(bpy^{\bullet})_3]^0$	No	68
$[Mg^{II}(bpy^{\bullet})_2(bpy^0)]^0$	No	69
$[Sc^{III}(bpy^{\bullet})_3]^0$	No	65
$[Y^{III}(bpy^{\bullet})_3]^0$	No	70
$[Ti^{III}(bpy^{\bullet})_3]^0$	Yes	71,72
$[Zr^{IV}(bpy^{\bullet})_2(bpy^{2-})]^0$	No	73
$[Hf^{IV}(bpy^{\bullet})_2(bpy^{2-})]^0$	No	74

$[V^{II}(bpy^{\bullet})_3(bpy^0)]^0$	No	75
$[Nb^{IV}(bpy^{2-})_2(bpy^0)]^0$	No	70
$[Ta^{V}(bpy^{\bullet})(bpy^{2-})_2]^0$	No	74
$[Cr^{III}(bpy^{\bullet})_3]^0$	No	76
$[Mo^{III}(bpy^{\bullet})_3]^0$	No	77
$[Mn^{II}(bpy^{\bullet})_2(bpy^0)]^0$	No	77
$[Re(bpy)_3]^0$	No	74
$[Fe^{II}(bpy^{\bullet})_2(bpy^0)]^0$	No	78,79
$[Ru^{II}(bpy^{\bullet})_2(bpy^0)]^0$	Yes	57
$[Os(bpy^{\bullet})_2(bpy^0)]^0$	No	57
$[Co(bpy)_3]^0$	No	80

a) Data from ref. [60] b) bpy = $C_{10}N_2H_8$; $bpy^{\bullet}$ = $[C_{10}N_2H_8]^-$ c) Oxidation states assigned by ref.[60]

Table 2.1. Selected examples of 4,4'-di-substituted homoleptic tris-bpy complexes

Complex	Ref.
$[Ti(^{Me}bpy)_3]^0$	60
$[V(^{Me}bpy)_3]^0$	60
$[Fe(^{tBu}bpy)_3]^{2+}$	81
$[Mo(^{Me}bpy)_3]^0$	82
$[Cr(^{Me}bpy)_3]^0$	60
$[V(^{tBu}bpy)]^n$ (n = 3+, 2+, 0, 1-)	59
$[Fe(dmbpy)]^{2+}$ (dmbpy = 5,5'-dimethyl-2,2'-bipyridyl)	83
$[Mo(^{tBu}bpy)_3]^{2+}$	84
$[Co(^{Me}bpy)_3]^{2+}$	85,86
$[Fe(^{Me}bpy)_3]^{2+}$	87
$[Ru(dcmb)_3]^{2+}$ (dcmb = 4,4'dimethyl-2,2'bipyridine)	88
$[Ru(^{tBu}bpy)_3]^{2+}$	88,89
$[Zn(tmamb)_3]^{2+}$ (tmamb = 4,4-triethylaminomethyl-2,2'bipyridine)	90
$[Fe(dabp)_3]^{2+}$ (dabp = 5,5'diamino-2,2'-bipyridine)	91
$[Ru(^{Me}bpy)_3]^{2+}$	92
$[Ru(dmesb)_3]^{2+}$ (dmesb = 4,4'-dimesityl-2,2'-bipyridine)	93
$[Ru(dadcb)_3]^{2+}$ (dadcb = N,N'-diallyl-4,4'dicarboxamide-2,2'-bipyridyl)	94
$[Zn(homb)_3]^{2+}$ (homb = 4,4'-bis(hydroxymethyl)-2,2'-bipyridine)	95
$[Zn(mob)_3]^{2+}$ (mob = 4,4'-bis(methoxy)-2,2'-bipyridine)	95

2.2 Results

2.2.1 Synthesis

The neutral tris-(bpy) complexes $[Al(^{tBu}bpy)_3]$ (**2.1**) and $[Al(^{Me}bpy)_3]$ (**2.2**) were synthesized by a reaction of $AlBr{\cdot}NEt_3$ with one equivalent ^{R}bpy (R = tBu or Me) in THF at room temperature (Eq. 2.1). Both **2.1** and **2.2** form as black needle-like crystals,

approximately 15 % crystalline yield. Copious amounts of black polycrystalline powders of **2.1** and **2.2** precipitate with the crystals and have been characterized via XRD-powder diffraction (see below). In addition, Al metal deposits on the sides of the flask during the synthesis.

$$3AlBr + 3(^{R}bpy) \xrightarrow{THF} [Al(^{R}bpy)_3]^0 + AlBr_3 + Al^0 \quad R = {}^{t}Bu, Me \qquad (2.1)$$

Single crystals of these complexes suitable for X-ray crystallography were grown at room temperature in the concentrated reaction mixture. The crystals of both **2.1** and **2.2** are soluble in THF and CH_3CN. Both complexes are air- and moisture-sensitive in solution and the solid state and have been characterized by single-crystal X-ray diffraction, X-ray powder diffraction, EPR, DC susceptibilities (SQUID magnetometry), electrochemistry, and ESI-MS.

2.2.2 Solid-State Structure

The $[Al(^{tBu}bpy)_3]$ (**2.1**) forms black rhombohedral needle-like crystals, space group $R\bar{3}$. The $[Al(^{Me}bpy)_3]$ (**2.2**) complex also forms black rhombohedral needle-like crystals but with $R\bar{3}c$ crystal symmetry. Summaries of the crystal data and selected bond distances and angles are given in Table 3.3-5. ORTEP drawings of the complexes are given in Figures 2.2 and 2.3.

The structures of **2.1** and **2.2** are quite similar, possessing aluminum atoms coordinated in slightly distorted octahedral environments.[60] Both have virtual D_3 point symmetry, and **2.2** is isomorphic with $[Cr(^{Me}bpy)]^0$ (Table 2.7).[60]

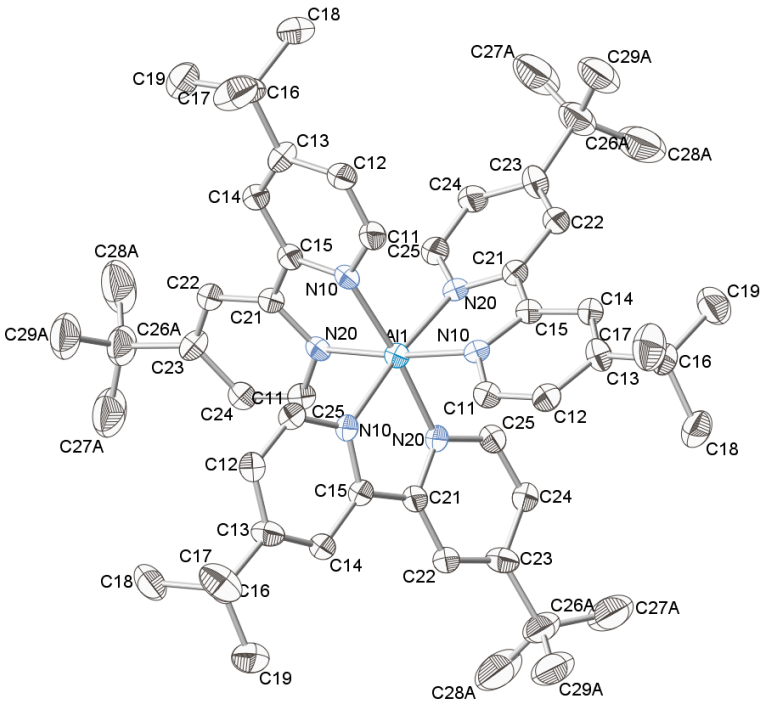

Figure 2.3. Structure of the neutral complex [Al(^{tBu}bpy)$_3$], thermal ellipsoids drawn at the 50% probability level. Hydrogen atoms have been omitted for clarity.

Table 2.2. Selected crystallographic data for [Al(^{tBu}bpy)$_3$] [a]

Compound	[Al(^{tBu}bpy)$_3$]
chem formula	$C_{54}H_{72}AlN_6$
fw	832.17 level
space group	$R\bar{3}$
a, Å	25.733(3)
b, Å	25.733(3)
c, Å	6.6434(7)
α, deg	90
β, deg	90
γ, deg	120
V, Å^3	3809.8(9)
Z	3
T, K	150(2)
ρ calcd g/cm^3	1.088
Reflns collected/2Θ$_{max}$	13559
F(000)	1353
R$_1$, GOF[b]	0.0570 / 1.000
R$_2$ ((I >2σ(I))	0.1347
Δρ$_{max}$, Δρ$_{min}$ (e/Å^3)	0.421, -0.353

[a]Observation criterion: I>2σ(I). $R_1 = \sum \| F_o| - F_c \| / \sum |F_o|$ [b] GOF = $\{\sum[w(F_o^2 - F_c^2)^2]/(n-p)\}^{1/2}$ [c] $wR_2 = \{\sum[w(F_o^2 - F_c^2)^2]/\sum[w(F_o^2)^2]\}^{1/2}$

Table 2.3. Selected Bond Lengths (Å) and angles (°) for Al(^{tBu}bpy)$_3$

Al1–N10	1.995(6)	C24–C25	1.379(4)
N10–C15	1.363(8)	Al1–N20	1.997(6)
C11–C12	1.380(4)	N10–C11	1.365(8)
C12–C13	1.384(7)	C13–C16	1.548(5)
C13–C14	1.390(7)	C16–C19	1.523(6)
C14–C15	1.416(4)	C16–C17	1.530(6)
C15–C21	1.420(5)	N20–C25	1.356(8)
N20–C21	1.368(8)	C21–C22	1.419(4)
C17–H17A	0.98	C23–C26	1.556(7)
C11–H11	0.95	C26–C27	1.529(7)
C26–C28	1.526(7)	C26–C29	1.524(7)
C22–C23	1.383(7)	N10–Al1–N20	78.66(18)
C23–C24	1.408(7)	C15–N10–Al1	116.9(6)
N10–C11–C12	123.4(3)	C11–N10–Al1	124.0(4)
C25–N20–Al1	124.3(4)	C21–N20–Al1	116.2(6)

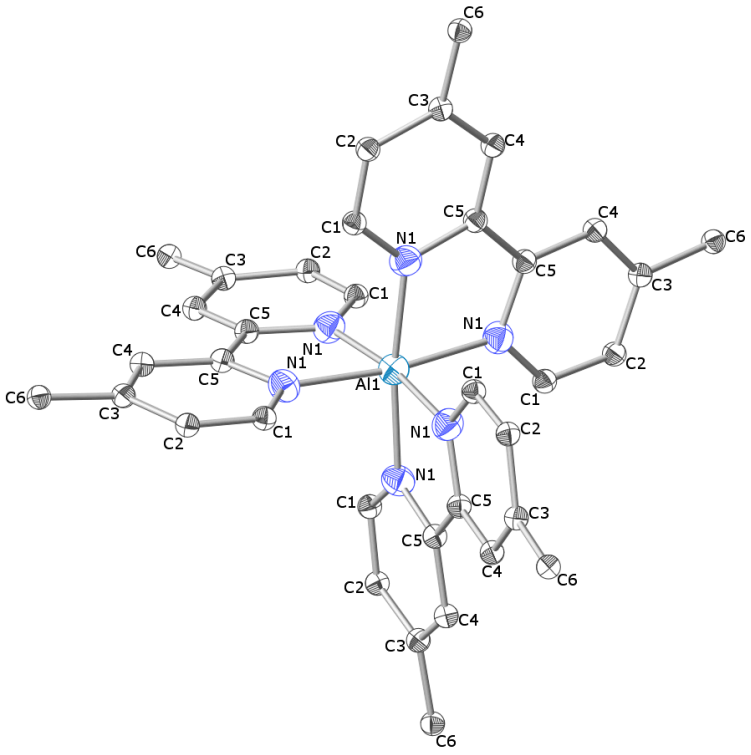

Figure 2.4. Crystal structure of the neutral complex [Al(^{Me}bpy)$_3$], thermal ellipsoids depicted at the 50% probability level. Hydrogen atoms have been omitted for clarity.

Table 2.4. Selected crystallographic data for $[Al(^{Me}bpy)_3]$ [a]

Compound	$[Al(^{Me}bpy)_3]$
chem formula	$C_{36}H_{36}AlN_6$
fw	579.69
space group	$R\bar{3}c$
a, Å	18.178(3)
b, Å	18.178(3)
c, Å	18.178(3)
α, deg	90
β, deg	90
γ, deg	120
V, Å^3	4458.8(19)
Z	6
T, K	150(2)
ρ calcd g/cm^3	1.295
Reflns collected/$2\Theta_{max}$	12008
F(000)	1842
R_1, GOF[b]	0.0373/1.036
R_2 ((I >2σ(I))	0.0779
$\Delta\rho_{max}$, $\Delta\rho_{min}$ (e/Å^3)	0.233/ -0.196

[a]Observation criterion: I>2σ(I). $R_1 = \sum \| F_o| - F_c \| / \sum |F_o|$ [b] GOF = $\{\sum[w(F_o^2 - F_c^2)^2]/(n-p)\}^{1/2}$ [c]$wR_2 = \{\sum[w(F_0^2 - F_c^2)^2]/\sum[w(F_o^2)^2]\}^{1/2}$

Table 2.5 Selected Bond Lengths (Å) and angles (°) for $Al(^{Me}bpy)_3$

Al1–N1	2.0002(12)	N1–Al1–N1	80.78(7)
N1–C1	1.3528(18)	N1–Al1–N1	171.90(7)
C1–C2	1.368(2)	N1–Al1–N1	92.58(7)
C2–C3	1.418(2)	N1–Al1–N1	93.59(4)
C3–C4	1.373(2)		
C4–C5	1.417(2)		
C5–C5	1.423(3)		
N1–C5	1.3902(18)		
C1–H1	0.970(17)		
C2–H2	0.978(16)		
C3–C6	1.504(2)		

The Al–N bond distances and N–Al–N chelate bond angles in **2.1** average 1.996(8) Å and 78.66(2)° respectively. For **2.2** the Al–N bond distances and N–Al–N chelate bond angles are equivalent at 2.000(1) Å and 80.78(7)° respectively, and equivalent to those of **2.1** within experimental error. The chelate angles are slightly compressed from the ideal 90° octahedral angles due to the constraints of ^{R}bpy ligand

ring structure. The intrachelate C–C bond distance for **2.1** (1.420(5) Å, ave.) and **2.2** (1.423(3) Å) are also equivalent within experimental error and are diagnostic of a $(^{R}bpy^{\bullet})^{1-}$ radical anions (Figures 2.3 and 2.4). To our knowledge, these are the first crystal structures containing $(^{R}bpy^{\bullet})^{1-}$ bound to aluminum.

The Al–N bond distances in **2.1** and **2.2** are similar to those of the $[AlCl_2(bpy)_2]^{1+}$ complex (Al–N = 2.0325(3) Å), which contains neutral bpy ligands and a central Al^{3+} ion. However, it is longer than Al–N contacts between dianionic bpy ligands $(bpy)^{2-}$ and Al^{3+} center ($[Al(bpy)_2]^{2-}$, Al–N = 1.8433(3) Å).[96,97] The shorter bonds to the $(^{R}bpy^{\bullet})^{1-}$ ligands are consistent with the trend observed in $[Cr(^{tBu}bpy)_3]^{n+}$ series, where n = 3, 2, and 1, containing both neutral and anionic bpy ligands.[98] However, the Al–N bond distances in general are not a good indicator of bpy oxidation state, due to poor distinction between aluminum bonds to neutral and monoanionic bpy ligands.

Table 2.6. Averaged Experimental C–C and C–N Bond Lengths (Å) of N,N'-Coordinated (bpy) Ligands in selected crystallographically characterized complexes (Refer to Bond labeling diagram). Adapted from [62].

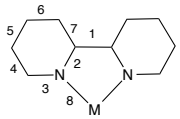

	bond number								
Complex	1	2	3	4	5	6	7	8	Ref.
$[Al(^{Me}bpy)_3]$	1.423(3)	1.3902(18)	1.3528(18)	1.368(2)	1.418(2)	1.373(2)	1.417(2)	2.0002(12)	this work
$[Al(^{tBu}bpy)_3]$	1.420(5)	1.3655(11)	1.3605(11)	1.3795(6)	1.396(10)	1.3865(10)	1.4175(6)	1.996(9)	this work
$[Ti(^{Me}bpy)_3]$	1.432(10)	1.388(10)	1.373(15)	1.362(16)	1.412(17)	1.379(15)	1.411(15)	2.103(7)	60
$[Cr(^{Me}bpy)_3]$	1.426(2)	1.384(1)	1.361(1)	1.372(2)	1.415(2)	1.378(2)	1.414(15)	2.018(1)	60
$[Ga(bpy)_3]^{3+}$	1.478(9)	1.353(9)	1.340(9)	1.39(1)	1.37(1)	1.395(10)	1.38(1)	2.07	64

In the solid state, the ^{Me}bpy rings of **2.2** pack with parallel offset π-stacking of the bpy ligands from neighboring molecules. In **2.2**, the methyl group (C6) is located directly above the centroid of an adjacent right with C6•••centroid distance of 3.701 Å (Figure 2.5).[99] This type of π-stacking is reminiscent of that observed in toluene and is also

present in the isomorphic [Cr(^{Me}bpy)$_3$] complex as well as the isostructural monoclinic analogs [Ti(^{Me}bpy)$_3$] and [Mo(^{Me}bpy)$_3$]. For these complexes the methyl C•••centroid distances are 3.582 Å, 3.515 Å, and 3.765 Å, respectively.[60] The similarities of these interactions among the four compounds suggest that π-stacking has a significant influence in the stability of the crystal lattices of these complexes, regardless of the central metal. Similar interactions are not observed in **2.1** or other ^{tBu}bpy complexes, presumably due to the sterics associated with the tert-butyl groups and general packing within the unit cell.

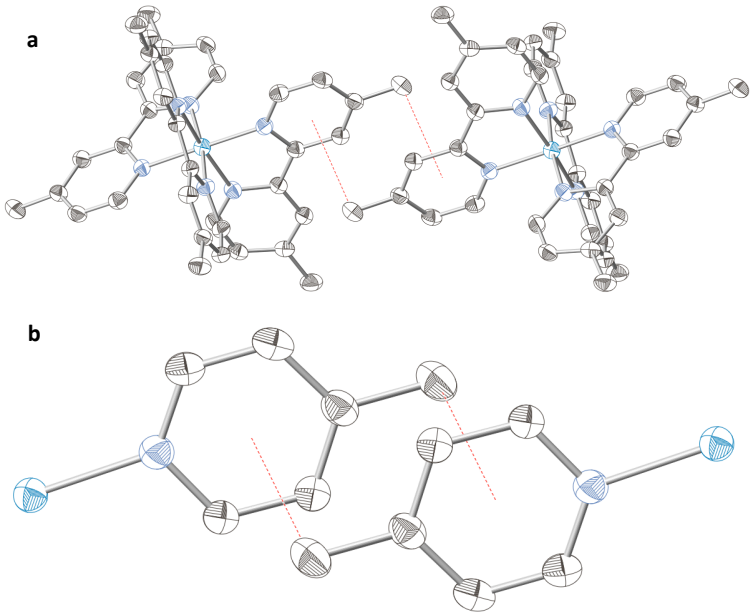

Figure 2.5. Me–π interactions (red dotted line) of 3.61Å between two adjacent 'chains' of [Al(^{Me}bpy)$_3$] within the crystal lattice (a) View down [111] (b) Zoomed in view of interaction between C_{Me} and the neighboring ligand (Me-π) (Al= teal; N = blue; C = gray, H atoms omitted for clarity)

The polycrystalline powders of both **2.1** and **2.2** were analyzed via X-ray powder diffraction. Due to the differences in the unit cells and subsequent packing within the cells, the diffraction patterns are distinctive for each complex. For complex **2.1** there are intense indicative peaks at 16.97°, 18.26°, and 21.92° representing the 1 $\bar{3}$ 1, 1 $\bar{5}$ 0, and

2 $\bar{5}$ 1 respectively (Figure 2.6(a)). In complex **2.2** there are more intense lower angle peaks to use for reference occurring at 12.67°, 15.93°, 18.75°, and 21.13° representing reflections at 0 1 2, 1 2 $\bar{1}$, 1 2 2, and 1 3 1 respectively (Figure 2.6(b)). Characterization in this manner assists in knowing the purity of the product.

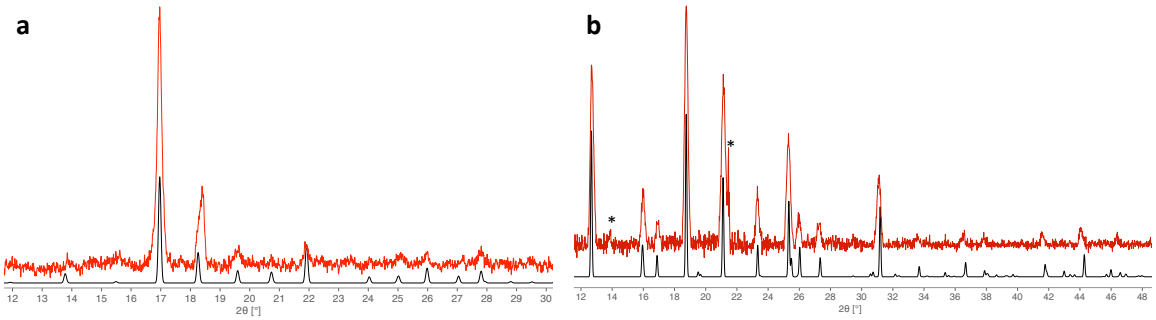

Figure 2.6. (a) XRD pattern for Al(^{tBu}bpy)$_3$; calculated (black) and observed (red) (b) XRD pattern for Al(^{Me}bpy)$_3$; calculated (black) and observed pattern (red) ; *denotes impurity present.

2.2.3 Mass spectrometry

A representative positive ion ESI-MS spectrum of [Al(^{tBu}bpy)$_3$] is shown in Figure 2.7. The parent ion [Al(^{tBu}bpy)$_3$]$^+$ is observed at 832.17 m/z with additional peaks representing [Al(^{tBu}bpy)$_2$]$^+$ and [Al(^{tBu}bpy)]$^+$ fragments at 563.77 and 295.38 m/z respectively, in much lower concentrations. Peaks representing [Al(^{tBu}bpy)$_2$]$^{2+}$, at 418.16, and a solvated adduct of [Al(^{tBu}bpy)$_3$]·THF solvate at 904.28 m/z are also observed.

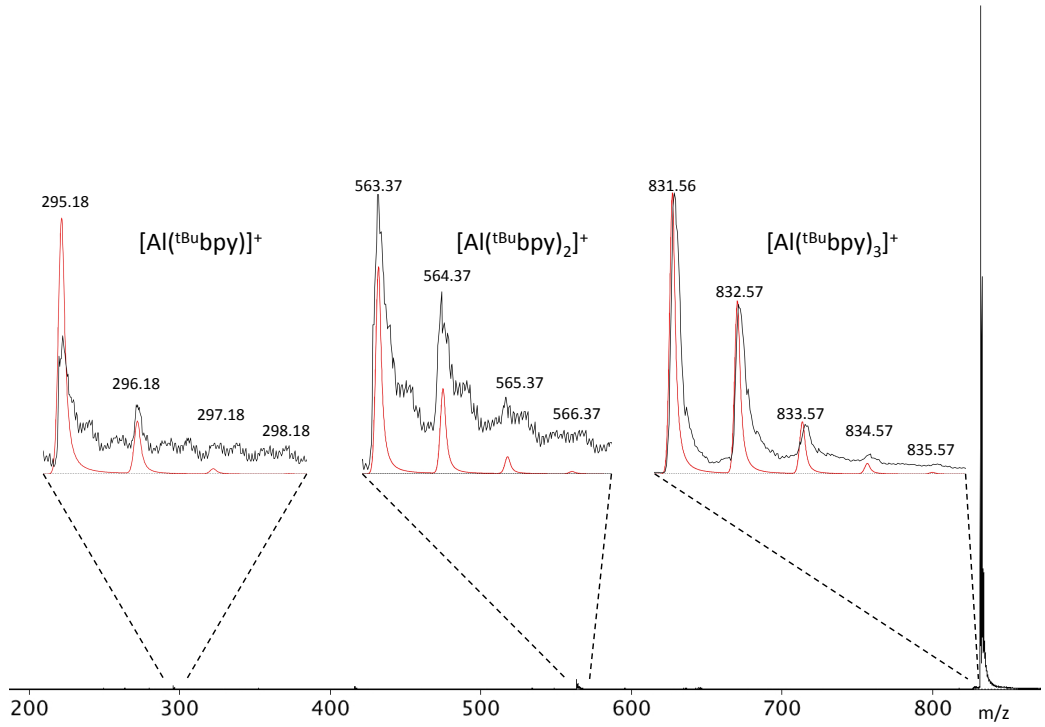

Figure 2.7. Positive ion ESI-MS of [Al(^{tBu}bpy)$_3$] recorded from crystalline material dissolved in THF. Insets show simulated (red) and observed (black) isotopic envelopes. [Al(^{tBu}bpy)$_3$]$^+$, [Al(^{tBu}bpy)$_2$]$^+$, and [Al(^{tBu}bpy)]$^+$.

Figure 2.8 shows a representative ESI mass spectrum for [Al(^{Me}bpy)$_3$] in THF, which contains the parent ion, [Al(^{Me}bpy)$_3$]$^+$ at 579.24 m/z and the related fragment [Al(^{Me}bpy)$_2$]$^+$ at 395.18 m/z.

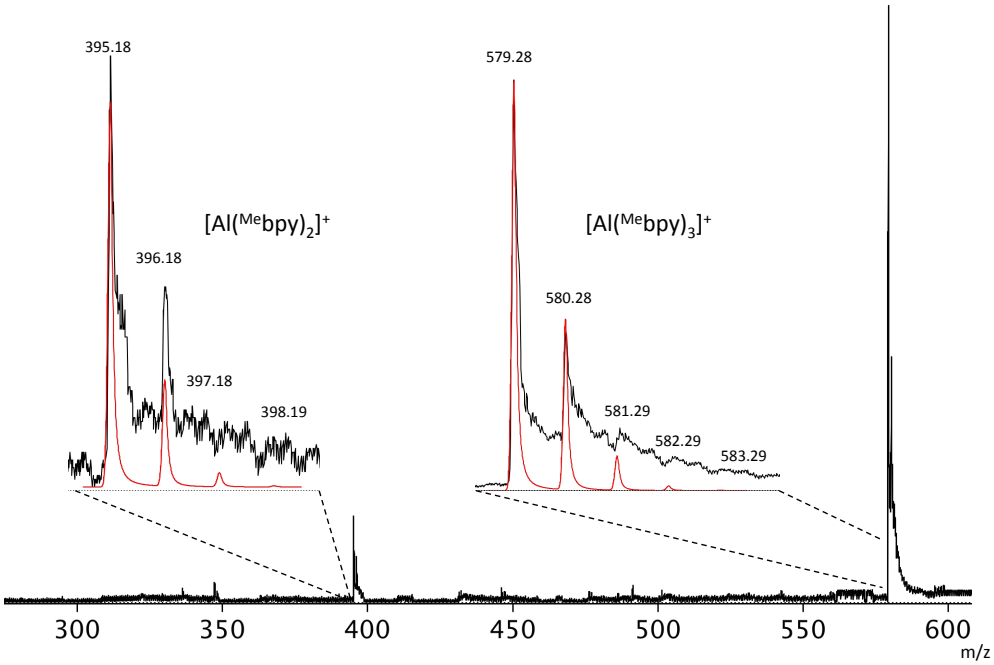

Figure 2.8. Positive ion ESI-MS of [Al(^{Me}bpy)$_3$] recorded from crystalline material dissolved in THF. Insets show simulated (red) and observed (black) isotopic envelopes. [Al(^{Me}bpy)$_3$]$^+$ and [Al(^{Me}bpy)$_2$]$^+$.

2.2.4 Electrochemistry

The cyclic voltammograms (CVs) and square wave voltammograms (SWVs) of **2.1** and **2.2** were recorded in the CH_3CN solution containing 0.1 M [N(*n*-Bu)$_4$]PF_6 as the supporting electrolyte, a glassy carbon working electrode, a platinum counter electrode, and a silver wire pseudo-reference electrode at ambient temperature. Control experiments of free ligand, solvent and electrolyte solution were recorded under the same conditions. The CVs and SWVs are shown in Figure 2.10 and the potentials ($E_{1/2}$) of the redox couples are listed in Table 2.8. All potentials are referenced to ferrocenium/ferrocene couple Fc^+/Fc. Evans method NMR, ESI-MS, and EPR studies (see next section) show that the complexes remain in the neutral, [Al^{3+}(^{R}bpy$^{\bullet}$)$_3$] state prior to electrochemical analysis. The free ^{tBu}bpy ligand in CH_3CN shows an irreversible peak at -1.68 V and a near-reversible peak at -2.72 V. For ^{Me}bpy there is an irreversible

peak at -1.66 V and quasi-reversible at -2.75 V. These redox potentials are distinct from those of **2.1** and **2.2** indicating the absence of free ligands in the analytes of the complexes.

The CV's of both **2.1** and **2.2** show two distinct regions of waves. For **2.1** (rest potential = -2.05 V), the first region exhibits three reversible oxidations at -1.38 V, -1.58 V, and -1.78 V (Figure 2.10 (a)) followed by a second region with two quasi-reversible reductions at -2.30 V and -2.65 V, and a non-reversible reduction at -3.00 V. For **2.2** (rest potential = -2.01 V), a similar pattern exists, except at slightly more positive values. The first region contains three reversible oxidations occurring at -1.32 V, -1.52 V, -1.72 V (Figure 2.10 (b)) and the second region has three quasi-reversible reductions occurring at -2.25 V, -2.48 V and -2.62 V. The $E_{1/2}$ values for **2.1** are slightly more negative than observed for complex **2.2**, presumably because the 4,4'-di-*tert*-butyl ligand is more electron donating than the 4,4'-dimethyl-bpy derivative. The separations in $E_{1/2}$ values (ΔE) for the oxidations in both **2.1** and **2.2** are constant at ≈ 0.20 V whereas for the last three waves the ΔE is more variable for the two complexes, but look to be greater than 0.30 V. These observations are further supported by the square-wave voltammograms collected for both **2.1** and **2.2** (Figure 2.10 (c) and (d)).

The electrochemical behaviors of **2.1** and **2.2** are quite similar to the corresponding Co(III) and Cr(III) complexes that contain redox-inert transition metal centers.[100,101] For **2.1** and **2.2** the first three waves positive to the rest potential are attributed to one-electron oxidations of $[Al^{3+}(^{R}bpy)_3]$ and the set of waves negative to the rest potential correspond to three successive one-electron reductions of **2.1** and **2.2**. The last reduction for $[Al^{3+}(^{R}bpy^{2-})_3]^{3-}$ is irreversible for **2.1**. Figure 2.9 illustrates these

electrochemical processes. Through these analyses, it appears that the fully reduced forms, $[Al^{III}(^{R}bpy)_3]^{3-}$, of both **2.1** and **2.2** are accessible.

$$[Al^{III}(^{tBu}bpy)_3]^{3+} \rightleftharpoons [Al^{III}(^{tBu}bpy)_2(^{tBu}bpy^{\bullet})]^{2+} \rightleftharpoons [Al(^{tBu}bpy)(^{tBu}bpy^{\bullet})_2]^{2+} \rightleftharpoons \quad (1)$$
$$\rightleftharpoons [Al^{III}(^{tBu}bpy^{\bullet})_2(^{tBu}bpy^{2-})]^{1-} \rightleftharpoons [Al^{III}(^{tBu}bpy^{\bullet})(^{tBu}bpy^{2-})_2]^{2-} \longrightarrow [Al^{III}(^{tBu}bpy^{2-})_3]^{3-}$$

$$[Al^{III}(^{Me}bpy)_3]^{3+} \rightleftharpoons [Al^{III}(^{Me}bpy)_2(^{Me}bpy^{\bullet})]^{2+} \rightleftharpoons [Al(^{Me}bpy)(^{Me}bpy^{\bullet})_2]^{2+} \rightleftharpoons \quad (2)$$
$$\rightleftharpoons [Al^{III}(^{Me}bpy^{\bullet})_2(^{Me}bpy^{2-})]^{1-} \rightleftharpoons [Al^{III}(^{Me}bpy^{\bullet})(^{Me}bpy^{2-})_2]^{2-} \rightleftharpoons [Al^{III}(^{Me}bpy^{2-})_3]^{3-}$$

Figure 2.9. Six complexes in the electron transfer series for $[Al(^{tBu}bpy)_3]$ **(1)** and $[Al(^{Me}bpy)_3]$ **(2)** as determined by electrochemistry.

Past the peaks representing the 2+/3+ couples there are there are two irreversible observable oxidation peaks for the both complex **2.1**, 0.362 V and 0.712 V, and complex **2.2,** 0.313 V and 0.662 V**,** that result in the decomposition of the analytes in solution. At that point, the dark solutions would lose color and white powder precipitates. The ΔE values between the oxidative currents are ≈0.35 V making them more similar to the reductive waves that are observe for the 1-/2- and 2-/3- couples observed for **2.1**.

The electronic coupling between the bpy redox centers can be evaluated through the analysis of comproportionation constant, K_c, defined by the representative equilibria shown in Scheme 2.1. The value of K_c can be calculated directly from the ΔE values according to Eq. 2.2. When using the ΔE form the SWV experiments, we obtain K_c values of $10^{3.38}$ for the oxidations of **2.1** and **2.2**. The average ΔE values for the reductive events for **2.1** and **2.2** yield K_c values of $10^{5.75}$ and $10^{4.56}$, respectively.[102]

$$K_c = e^{(\Delta E)F/RT} \quad (2.2)$$

$$[Al(^{R}bpy)_3]^0 + [Al(^{R}bpy)_3]^{2-} \overset{K_c}{\rightleftharpoons} 2[Al(^{R}bpy)_3]^{1-}$$

$$[Al(^{R}bpy)_3]^{1-} + [Al(^{R}bpy)_3]^{3-} \overset{K_c}{\rightleftharpoons} 2[Al(^{R}bpy)_3]^{2-}$$

Scheme 2.1. Process indicated by the comproportionation constants determined for the reductive events observed in the electrochemical data (based on ΔE).

The K_c values are indicative of weakly or non-coupled electrochemical oxidations in complexes **2.1** and **2.2** (class I mixed valent compounds)[102,103] whereas the reductions appear to be electronically coupled (class II mixed valent compounds)[102,103] as described below. Electrochemical studies performed on related Al^{3+} complexes with N-N bidentate ligands show ΔE values for one- electron processes at 0.19 V and 0.34 V corresponding to $K_c = 10^{5.8}$ and $K_c = 10^{3.21}$, respectively. The former is associated with class II mixed-valent compounds, in which the bpy ligands are electronically coupled through the Al center. The latter process ($K_c = 10^{3.21}$) is associated with class I behavior indicative of virtually non-existent coupling in these electrochemical events.[103] Based on studies, we classify the oxidations of **2.1** and **2.2** as class I mixed-valent processes, and the reductions as class II mixed valent processes (Scheme 2.1).[103]

Table 2.7. Ground State Reduction Potentials (SWV) for substituted Tris(bipyridine) aluminum complexes and free substituted bipyridine ligands

	$E_{1/2}$, V							
Complex	3+/2+	2+/1+	1+/0	ΔE	0/-1	-1/-2	-2/-3	ΔE
$[Al(^{tBu}_2bpy)_3]$	-1.38	-1.58	-1.78	≈0.20	-2.30	-2.67	-3.00 [b]	≈0.35
$[Al(^{Me}_2bpy)_3]$	-1.32	-1.52	-1.72	≈0.20	-2.28	-2.54 [c]	-2.67	N/A
$^{tBu}_2bpy$					-1.68	-2.71		≈1.03
$^{Me}_2bpy$					-1.66	-2.75		≈1.09

a) Potentials are Referenced versus the Ferrocenium/Ferrocene Couple, Fc^+/Fc
b) Irreversible
c) The -1/-2 and -2/-3 $E_{1/2}$ values are estimated due to overlap

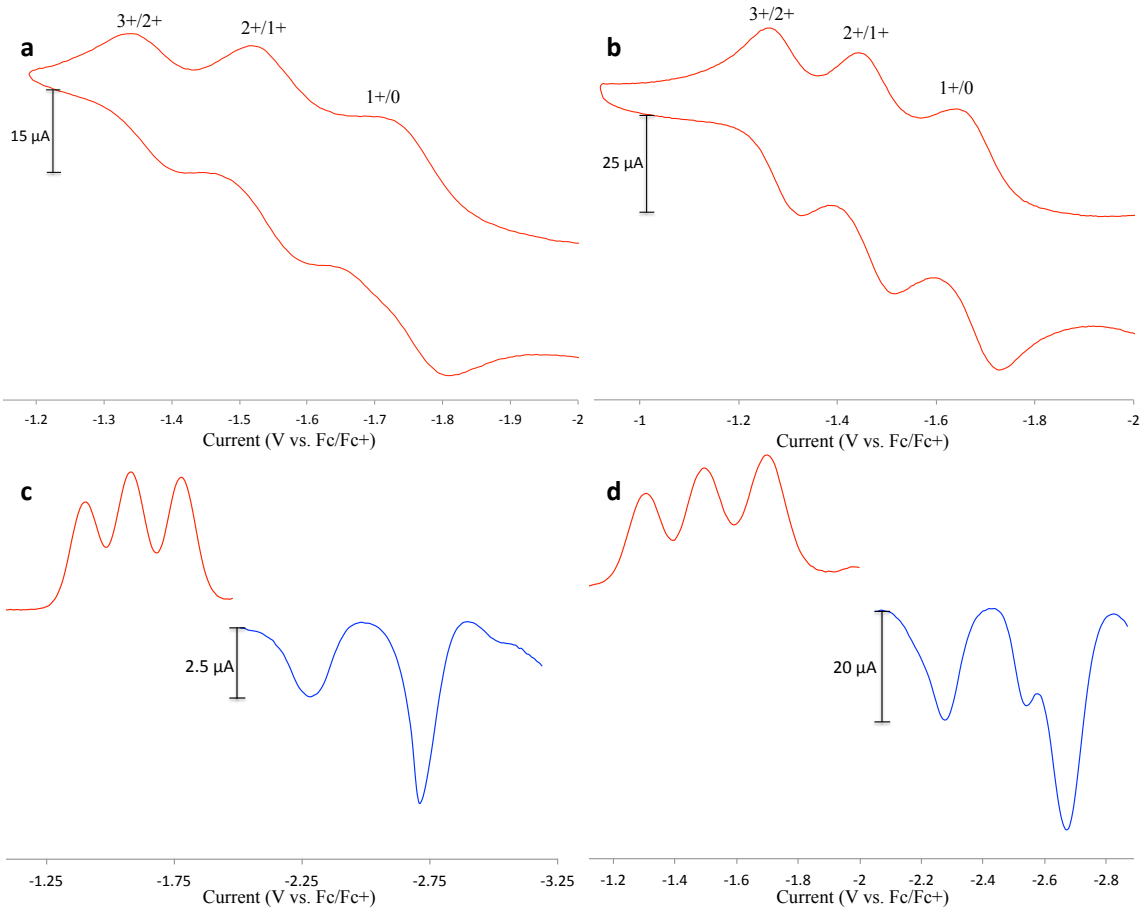

Figure 2.10. Cyclic voltammograms of (a) [Al(^{tBu}bpy)$_3$] (scan rate of 20 mVs^{-1}) and (b) [Al(^{Me}bpy)$_3$] (scan rate of 20 mVs^{-1}) Showing the near-reversible oxidative waves. (c) Square-wave voltammograms of [Al(^{tBu}bpy)$_3$] and (d) [Al(^{Me}bpy)$_3$] both recorded at a scan rate of 30 mVs^{2-} (red: oxidative processes, blue: reductive processes). All data was recorded at room temperature in CH_3CN solutions containing 0.1 M [N(*n*Bu)$_4$][PF_6]. Potentials are referenced vs. the Fc^+/Fc redox couple

2.2.5 Magnetic Properties

The magnetic properties of complexes **2.1** and **2.2** were measured in both the solid state (d.c. susceptibility) and in solution (EPR, Evan's method NMR). The d.c. susceptibilities of the both complexes (Figure 2.9) show Curie-Weiss behavior and large, negative Weiss constants (-526 K, **2.1** and -437 K, **2.2**) associated with strong antiferromagnetic coupling. Fits of the high temperature data to the Curie-Weiss law:

$$\chi = \frac{C}{(T-\theta)} \tag{2.3}$$

where C is the Curie constant and θ is the Weiss constant give effective magnetic moments of 3.78 BM (**2.1**) and 3.88 BM (**2.2**), which are indicative of S = $^3/_2$ spin states associated with the three unpaired electrons of the (^{R}bpy$^{\bullet}$)$^{-1}$ radical anions. Below 140 K, the effective magnetic moment of **2.1** steadily decreases from 3.78 BM to 0.78 BM at 5 K. This behavior is consistent with the predicted S = ½ ground state of the Al(bpy)$_3$ complexes and presence of low-lying S= $^3/_2$ excited states that are populated at room temperature.[67]

In addition to the strong antiferromagnetic coupling within the Al(^{R}bpy)$_3$ complexes, crystals of **2.2** also show three-dimensional antiferromagnetic ordering interactions below 80 K. To our knowledge, this behavior is the first example of three-dimensional magnetic ordering of a molecular bpy complex to be reported. Additional studies of the magnetic properties of **2.2** are in progress.

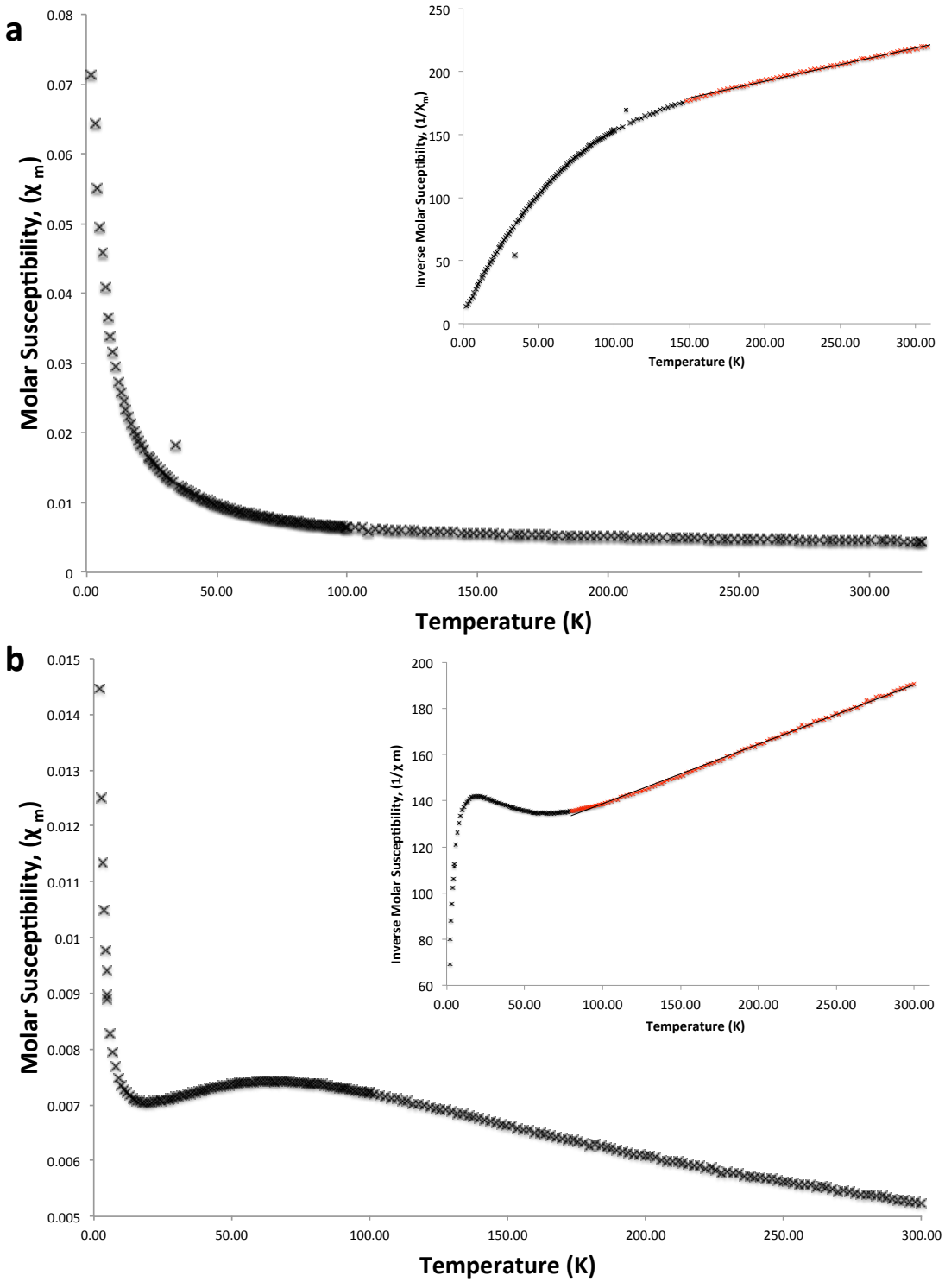

Figure 2.11. Magnetic susceptibility of (a) [Al(^{tBu}bpy)$_3$] and (b) [Al(^{Me}bpy)$_3$]; red = onset of Curie Weiss behavior indicating antiferromagnetic coupling for S=$^3/_2$ systems; black = non-Curie Weiss behavior.

The magnetic moments of the Al(^{R}bpy)$_3$ complexes were also measured in solution by way of the Evan's NMR method. Acetonitrile solutions of both complexes show strong paramagnetism in solution, however, the room temperature susceptibilities are indicative of S = $^1/_2$ spin states, which is in sharp contrast to the room temperature solid state S = $^3/_2$ spin states measured from the d.c. susceptibility studies described above.

The molar paramagnetic moment in solution can be calculated by way of Eq.2.4:

$$\chi_M^P = \frac{3\Delta\nu M^P}{4\pi\nu m^P} + \chi_0 M^P \frac{(d_0 - d_s^P)}{m^P} - \chi_M^{dia} \qquad (2.4)$$

Where $\Delta\nu$ is the resulting paramagnetic contact shift in Hz, ($|\nu - \nu_0|$), M^P is the molecular weight of the material in g/mol, ν is the NMR field strength in Hz, m^p is the concentration of the material in g/L, χ_0 is the paramagnetic susceptibility of the solvent, d_0 the density of pure solvent in g/mL, and χ_m^{dia} is the diamagnetic moment for the solute, calculated to be -363 × 10^{-6} emu for **2.1** and -321 ×10^{-6} emu for **2.2** using standard tables.[104] The internal capillary contains the same solvent as the outer capillary, correcting for the solvent susceptibility in the solution, thus making the second term of the equation trivial. It has also been established that with low concentrations of low-density solutes the third term approaches zero, as $|d_0 - d_s^p|$ approaches zero. Taking these assumptions into account Eq. 2.4 reduces to Eq. 2.5:

$$\chi_M^P = \frac{3\Delta\nu M^P}{4\pi\nu m^P} - \chi_M^{dia} \qquad (2.5)$$

Inserting both the observed and calculated values into the above equation yields a molar paramagnetic susceptibility in emu. Inserting these values for χ_M^P into Equation 2.6:

$$\mu_B = 2.828\sqrt{\chi_P \times T} \quad (2.6)$$

yields the calculated effective magnetic moment for reference the value for one free electron is equal to 1.73 Bohr Magneton where for one free electron S = $^1/_2$ and g = 2.0023 (gyromagnetic ratio of an electron).

The measured moment for **2.1** in CH_3CN (1.73 BM) is equal to the expected spin-only moment for a S = ½ system whereas the moment for **2.2** is somewhat low (1.39 BM), presumably due to its limited solubility and associated errors of concentrations. The magnetic moments are unchanged when supporting electrolyte (0.1 M of $[N(n\text{-}Bu)_4]PF_6$ in CH_3CN) was added to the solution.

The X-band EPR spectrum of **2.1** and **2.2** in THF at room temperature are similar to that reported for $[Al(bpy)]^0$ **(2.3)**, with $g_{iso} \approx 2.0064$.

2.3 Discussion

Reactions of $AlBr{\bullet}NEt_3$ with ^{R}bpy (R= Me or tBu) yield both $[Al(^{tBu}bpy)_3]$ **(2.1)** and $[Al(^{Me}bpy)_3)]$ **(2.2)**. The synthesis of these 'homoleptic tris-bpy' type complexes, **2.1** and **2.2** differ from previous reports for the analogous complex $[Al(bpy)_3]$ **(2.3)**. Both **2.1** and **2.2** represent the first structurally characterized main-group homoleptic tris-bipyridyl complex containing monoanionic bpy ligands. Traditionally **2.3** and similar transition metal complexes have been prepared via reductive methods, but **2.3**, as reported by Herzog *et al.* has never been structurally characterized. The difference in synthetic approach perhaps accounts for our ability to isolate these compounds in pure form. The structures and properties of **2.1** and **2.2** are consistent with the predicted properties of **2.3**. Both complexes, like many other isolated homoleptic tris-bipyridyl complexes, exhibit D_3 symmetry. The intrachelate bond distances, along with the electrochemical and magnetic

properties, within each complex are highly indicative of Al^{3+} and $^{R}bpy^{\bullet}$, oxidation state assignments.[62,81]

Complexes **2.1** and **2.2** were prepared utilizing the disproportion pathway characteristic of metastable AlX·L (X= Cl or Br; L = donor solvent) solutions. The redox active bidentate bpy ligands appear to be prone to stabilizing monomeric Al^{3+} ion rather than lower or mixed valent aluminum products. We have employed the same synthetic procedures to prepare $[Al(bpy)_3]^0$, but to date crystals have not been isolated. A similar low-valent GaX starting material has been previously applied to the synthesis of $[Ga(bpy)_3]^{3+}$, however the Ga complex contains neutral bpy ligands. As a result aluminum has the unique distinction of being the only main group metal in which all three bpy redox states have been isolated and structurally characterized: $(bpy)^0$, $(bpy^{\bullet})^-$, and $(bpy)^{2-}$.[96,97] For reference, the N,N'-coordinated $(bpy^{2-})^{2-}$ dianion has only been structurally characterized three times.[58]

McGrady and Goicoechea *et al.* first established that C_{py} –C_{py} bond distances in first row transition metal bpy complexes do not vary significantly with the d^n electron configuration of the metal ion.[105,106] It was found that the C_{py}–C_{py} bond distances do vary based on the charge of the ligand, as reported by Wieghardt *et al.*[62] Structural data for $[B^{III}(bpy^{\bullet})Cl_2]^0$, $[B^{III}(bpy^0)Cl_2]Cl$, and $[Ga(bpy)_3]^{3+}$ uphold the trends and assignments put forth by Wieghardt *et al.* based on their observations of intrachelate bond distances in transition metal homoleptic tris bpy complexes. [64,107] This work gives us confidence in the assignments of oxidation states of Al^{3+} in **2.1** and **2.2** (Table 2.7), and demonstrates that oxidation state assignments based on C_{py}–C_{py} bond distances extends to 4,4'-disubstituted-2,2'-bpy complexes for main group homoleptic tris-bpy complexes.

The electrochemistry of both **2.1** and **2.2** demonstrate that six other oxidation states of the complexes are accessible from the neutral species: $[Al(^{R}bpy)]^{3+}$, $[Al(^{R}bpy)]^{2+}$, $[Al(^{R}bpy)]^{1+}$, $[Al(^{R}bpy)]^{1-}$, $[Al(^{R}bpy)]^{2-}$, $[Al(^{R}bpy)]^{3-}$. These interconversions occur through a series of single electron oxidations and reductions. The oxidation processes are occurring through the addition and removal of electrons from the ligand-based π^* orbital (SOMO) of the $(bpy^{\bullet})^{-}$ ligands.[81] The reduction processes observed for both **2.1** and **2.2** are weakly coupled through the ligand-based orbitals and the aluminum center, as indicated by the comproportionation constants K_c of $10^{5.8}$.

Previous studies of **2.3** demonstrated that the antiferromagnetic interactions give rise to a ground state doublet that is slightly more stable than the low-lying quartet excited state, with a gap of 230-240 cm^{-1} (-3 J/k_B = 330-345 K).[108] For reference the scandium analogue's gap is more than double that 420 cm^{-1} (-3 J/k_B = 600 K).[108] In **2.3** the lone pair electrons of bpy nitrogens are partly donated to aluminum 3s, 3p, and 3d orbitals, while each bpy traps an electron in its lowest vacant π orbital. Ultimately the 3^{+} charge on aluminum is effectively neutralized due to the σ-donation from the N on the ligand and according to calculations the π-type back bonding is what yields the gap between the doublet and the quartet.[108] As previously stated in **2.3** these two states are extremely close in energy.

More recent calculations have shown that S = $^1/_2$ ground state is attained through an intramolecular antiferromagnetic exchange coupling between two of the $(bpy^{\bullet})^{-}$ anions through the diamagnetic central metal ion. These exchange pathways are available because the $(bpy^{\bullet})^{-}$ anions are not orthogonal to one another.[81] Therefore in both

complexes with three empty t_{2g} metal orbitals (d^0), the radical-radical coupling is antiferromagnetic.

Inoue *et al.* showed that **2.3** obeyed Curie-Weiss law at the high temperature with μ_B = 3.24 B.M., which is close to the expected spin-only value for three unpaired electrons. At T < 40 K the moment is suppressed to μ_B = 1.73 B.M. which is consistent with the S = $^1/_2$ ground state electronic configuration. These experiments, first demonstrated that the three spins within the complex were antiferromagnetically coupled at low temperatures.

Both **2.1** and **2.2** show antiferromagnetic coupling below 130 K (**2.1**) and 80 K (**2.2**) respectively, consistent with the expected S = $^1/_2$ ground state. Above these temperatures, the data show S = $^3/_2$ spin states that are indicative of thermally populated low-lying quartet excited states with three unpaired electrons. This behavior is similar to that of **2.3**, however, the low magnetic properties differ at lower temperatures. For **2.1** the antiferromagnetic behavior below 40 K gives rise to an effective moment of 0.78 μ_B, which is less than half of what would be expected for a spin $^1/_2$ system. At this point, we can only speculate that the difference in the expected ground state behavior has to do with intermolecular interactions that further reduce the magnetic moment.

The low temperature magnetic data for **2.2**, is even more unusual in that it shows an apparent long range ordering below 80 K. While long-range ordering is ubiquitous in solid-state chemistry, magnetic ordering between discrete molecules above 10 K is not common.[109] Similar interpretations for the magnetic data of $[Ru(bpy)_3]^0$ have been proposed for extremely broad 'sub-Curie' tail displayed by this compound.[110] However, more recently it has been reported that the spins of the two $(bpy^{\bullet})^-$ radicals in

$[Ru^{II}(bpy^{\bullet})_2(bpy^0)]$ are strongly antiferromagnetically coupled to one another.[81] The observed coupling is through the diamagnetic Ru^{II} center, and are not intermolecular in nature due to subprime π–π contacts, yielding a diamagnetic ground state (S=0) and excited triplet state (S=1).[81] It is our belief that our narrower 'sub-Curie' tail in **2.2** is the result of the intermolecular interactions between the bpy ligands due to the presence of the π–π stacking. This stacking coupled with the closeness in energy between the ground and excited state due to the Al-center results in the unexpected 'ordering' observed at low temperatures. Further studies of this system are in progress.

2.4 Conclusion

The utilization of the unique AlX precursor solutions gives crystalline homoleptic tris-bpy complexes **2.1** and **2.2** in good yields. These compounds represent the first structurally characterized homoleptic tris-bpy Al complexes and the first main group metal complex of any type to contain mono-anionic bpy ligands. Aluminum is one of the only metals to have structural characterization involving all three oxidation state of bipyridine type ligands: $[Al^{III}Cl_2(bpy^{0)}_2]Cl{\cdot}CH_3CN$[97], $[Li^+(THF)_4][Al^{III}(bpy^{2-})_2]$[96], $[Al(^{R}bpy^{\bullet})_3]$ (where R= Me or tBu).

Both complexes **2.1** and **2.2** S= $^1/_2$ ground states and low-lying excited S= $^3/_2$ excited states which is similar to that previously reported for $[Al(bpy)_3]$. In solution both **2.1** and **2.2** reside in their S = $^1/_2$ ground state, which presumably results from solvent stabilization of the ground state, destabilization of the excited state, or both. In **2.2** there is apparent long range magnetic ordering in the solid-state below 80 K, which has not been reported in similarly ligated transition metal ^{Me}bpy complexes. In all of these tris ^{Me}bpy complexes pi-stacking interactions are apparent, suggesting that this magnetic ordering is

due to ligand-ligand interactions in conjunction with having an Al-center as opposed to a transition metal center. Similar behavior, has not been observed in **2.1** due to the bulkiness of the tert-butyl substituents. In **2.3** it is possible that solvate impurities interrupt potential interactions between the [$Al(bpy)_3$] molecules.

Electrochemical experiments of both **2.1** and **2.2** show similar behavior to one another in solution and show that it may be possible to isolate other oxidation states of these complexes. To date this is the most complete report of a main-group centered homoleptic tris-bpy complex.

2.5 Experimental Details

General considerations. All air and water free manipulations were performed using standard Schlenk techniques. Solvents were dried over proper drying agents according to literature procedures: toluene, THF, and hexane over sodium benzophenone, and triethylamine over calcium hydride. Bipyridyl (bpy), 4-4'-di-*tert*-butyl-2,2'-bipyridine (^{tBu}bpy), and, 4-4'-di-*methyl*-2,2'-bipyridine (^{Me}bpy) were purchased from Sigma Aldrich and dried in vacuo before use.

$AlBr•(NEt_3)_n$. Aluminum metal (0.5514 g, 20.4 mmol) was reacted with gaseous HBr (24.29 mmol) over 3 h at approximately 1200 K in a modified Schnöckel-type metal halide co-condensation reactor. The resultant gas-phase AlBr was co-condensed with a mixture of toluene: triethylamine (3:1 v/v) at approximately 77 K. The solvent matrix was thawed to -80°C and the resultant yellow-brown solution stored at that temperature prior to use. Titration of the $AlBr•(NEt_3)_n$ via Mohr's method determined a bromide concentration of 152 mM an Al:Br ratio of 1:1.19.

$AlCl•(Et_2O)_n$. Aluminum metal (0.5514 g, 20.4 mmol) was reacted with gaseous HCl (37.28 mmol) over 3 h at approximately 1200 K in a modified Schnöckel-type metal halide co-condensation reactor. The resultant gas-phase AlBr was co-condensed with a mixture of toluene: diethyl ether (3:1 v/v) at approximately 77 K. The solvent matrix was thawed to -80°C and the resultant yellow-brown solution stored at that temperature prior to use. Titration of the $AlCl•(Et_2O)_n$ via Mohr's method determined a chloride concentration of 187 mM an Al: Cl ratio of 1:1.25.

[Al(^{tBu}bpy)$_3$] [2.1]. THF (15 mL) was added to a 50-mL Schlenk vessel containing ^{tBu}bpy (0.4310 g; 1.61 mmol). Once the ^{tBu}bpy was dissolved resulting a clear solution $AlBr·(NEt_3)_n$ (1.61 mmol, 10.6 mL of a 152 mM solution in toluene: triethylamine 3:1) was added via syringe at room temperature. The dark green reaction mixture was stirred for 12 hours and subsequently concentrated under vacuum to ¾ its original volume, filtered via cannula, and stored at room temperature. After a period of 3 days dark green needles crystallized from the reaction mixture.

[Al(^{tBu}bpy)$_3$] [2.1]. $AlCl·(Et_2O)_n$ (0.5 mmol, 2.2 mL of a 233 mM solution in toluene: diethylether 3:1) was added via syringe at room temperature to an Schlenk vessel charged with ^{tBu}bpy (0.1340 g; 0.5 mmol). The dark green reaction mixture was stirred for 1 hour at room temperature and subsequently concentrated under vacuum to ¾ its original volume and filtered via cannula and stored at room temperature for 1 week. The reaction mixture was then transferred into a vial in the glovebox and subsequently layered with hexane. After 3 weeks large dark green crystals formed on the walls of the vial. Preliminary structure analysis supports the formation of [Al(^{tBu}bpy)$_3$].

[Al(^{Me}bpy)$_3$][2.2]. THF (15 mL) was added to a 50-mL Schlenk vessel containing ^{Me}bpy (0.3721 g; 2 mmol). Once the ^{Me}bpy was dissolved resulting a clear solution $AlBr\cdot(NEt_3)_n$ (2 mmol, 13.2 mL of a 152 mM solution in toluene: triethylamine 3:1) was added via syringe at room temperature. The dark pink-red reaction mixture was stirred for 12 hours and subsequently concentrated under vacuum to ¾ its original volume, filtered via cannula, and stored at room temperature. After a period of 3 days black needles crystallized from the reaction mixture.

Physical Methods.

Single Crystal Data: Peter Zavalij at the University of Maryland College Park collected crystallographic data. Graphite monochromated Mo Kα radiation (λ= 0.71073 Å) from a Mo-target rotating-anode X-ray source was used throughout. Data were corrected for absorption effects using the multi-scan methods, the structure was solved and refined using the Bruker transmission coefficients (based on crystal size) are 0.8910 and 0.9950.

Powder X-Ray diffractions (XRD) patterns were obtained on a Bruker D8 advance diffractometer equipped with Lynxtec detector using a monochromatic Cu Kα radiation source biased at 40 kV and 40 mA. The XRD patterns were background corrected. For air-free collection, a dome supplied by Bruker was used to for the samples

Powder X-ray diffraction (XRD): patterns of samples were obtained on a Bruker C2 Discover diffractometer equipped with a VÅNTEX-500 detector using a monochromatic Cu kα radiation source biased at 40 kV and 40 mA. For air-free collection, samples were loaded into 0.7 mm capillaries and sealed with epoxy.

Evan's method experiments: consisted of two set-ups. A standard of just CH_3CN and another of CH_3CN containing 0.1 M of $[N(n\text{-}Bu)_4]PF_6$, the electrolyte used in the

electrochemical experiments, was prepared. Separately, a small amount of **2.1** and **2.2** (10.5 mg, 0.01126 mmol) were dissolved in 2.5 mL of prepared standard and sealed in a J. Young NMR tube containing a capillary filled with prepared standard.

Electrochemical measurements: were performed using a Pine WaveNow potentiostat inside a glovebox under Ar atmosphere. The electrochemical cell consisted of a modified three-electrode set-up with a glassy carbon working electrode, a platinum counter electrode and a silver wire pseudo-reference electrode. Ferrocene was used as an internal reference and introduced at the end of the experiment and potentials are referenced versus the Fc^{+}/Fc couple.

Zero field-cooled magnetometry: Superconducting quantum interference device (SQUID) magnetization data of crystalline samples were recorded with a SQUID magnetometer at 1 T.

Mass spectra: were collected on ACCUTOF ESI-MS at 3000 V in a THF solution utilizing our in-house introduction source (see-Appendices).

Chapter 3: Synthesis and characterization of $[LiOEt_2]_2[HAl_3(PPh_2)_6]$

3.1 Introduction

Reduced oxidation state chemistry of main group elements has undergone rapid development in recent years, [4,5,111-114] and focus has been centered on clusters of heavier group 13 elements containing metal–metal bonds of formula $(MR)_n$ (M = Al-Tl; R = hydrocarbyl). The clusters can be isolated in various degrees of aggregation, including dimers,[15-17,115] tetramers featuring M_4 tetrahedra,[113,116,117] and weakly bound hexamers.[113,118] The number of trimeric frameworks, $(MR)_3$ (containing M–M bonds) are fewer than that of dimers, but more recent examples of group 13 and 14 trimeric clusters have been reported. In 1995 Robinson *et al.* reported the first stable examples, $[RGa]_3Na_2$ and $[RGa]_3K_2$ (R=$(Mes_2C_6H_3)$); which were isolated from the sodium or potassium metal reductions of $(Mes_2C_6H_3)$-$GaCl_2$ in diethyl ether.[118] In 1996, Schnöckel *et al.* isolated the trigonal bipyramidal structure $As_2(AlCp^*)_3$, and in 2000 Wiberg reported a stable radical, $[Al_3(tBu_3Si)_4]^\bullet$, from thermolysis of $Al_2(tBu_3Si)$.[8,14] Sekeguchi isolated the 'cyclotrisilenylium' ion in $[Si_3R_2R']$ (R=Si^tBu_3, R' = $SiMe_2{}^tBu$) in 2003, and in 2006 'cyclotrialuminene' $(AlAr")_3^{2-}$ (Ar" = $Mes_2C_6H_3$) was reported by Power *et al.*[119,120] Among these examples the presence of 2 delocalized π electrons in $[GaAr"]_3^{2-}$ and $[AlAr"]_3^{2-}$ suggested that cyclotrialuminene and cyclogallene are aromatic, and nucleus independent chemical shift (NICS) calculation confirmed the metalloaromaticity of $Na_2[GaAr"]_3$. Although the number of main-group cluster compounds is increasing the scope of ligands to produce clusters with multiple Al–Al bonds is limited.[5,14]

Schnöckel *et al.* have previously explored PR_2 ligands (where R = tBu) yielding the series of clusters $[Al_4(P(tBu)_2)_mX_{6-m}]$.[121] This group of clusters has been shown to be related to the Al_4H_6 cluster.[121]

We describe here expansion of the exploration of the PR_2 ligands through the synthesis and characterization of the $[LiOEt_2]_2[HAl_3(PPh_2)_6]$ complex (herein denoted the $[HAl_3(PPh_2)_6]^{2-}$ cluster) with a D_{3h}–HAl_3P_6 core. This compound has been extensively characterized by single-crystal X-ray diffraction, X-ray powder diffraction, EPR, zero-field cooled magnetometry, NMR, and electron spray ionization mass spectrometry (ESI-MS).

3.2 Results

3.2.1 Synthesis

The species $[LiOEt_2]_2[Al_3(PPh_2)_6H]$ (**3.1**) was synthesized via a reaction of $AlCl{\cdot}Et_2O$ with two equivalents of $LiPPh_2$ at room temperature (eq. 3.1).

$$4AlCl \bullet Et_2O + 6LiPPh_2 + H \cdot \xrightarrow{65^\circ C} [LiOEt_2]_2[HAl_3(PPh_2)_6] + Al^0 + 4LiCl \qquad (3.1)$$

The complex crystallizes as dark orange-red crystals in 15% yield after heating. The hydrogen atom originates from the solvent and or ligand degradation during the synthesis (see below). Aluminum metal precipitates on the sides of the flask during the reaction. Single crystals of this cluster suitable for X-ray crystallography were grown over a three day period at 65°C in the concentrated reaction mixture. They are air- and moisture-sensitive in both solution and solid-state phases, and soluble in THF and DMF. Cluster **3.1** has been characterized by single-crystal X-ray diffraction, X-ray powder diffraction, EPR, zero field cooled magnetometry via SQUID, and electron spray ionization mass spectrometry (ESI-MS).

3.2.2 Solid-state structure

The $[LiOEt_2]_2[HAl_3(PPh_2)_6]$ cluster is triclinic, space group $P\bar{1}$, and contains two $[LiOEt_2]^+$ cations, one $[HAl_3(PPh_2)_6]^{2-}$ dianion, and a single disordered toluene solvate molecule. An ORTEP drawing of **3.1** is given in Figure 3.1 and a summary of crystallographic data and selected bond distances are listed in Tables 3.1 and 3.2. Analysis of the diffraction data revealed that the structure was highly disordered, and **3.1** exhibits full molecule disorder (Figure 3.2). The location of the H atom remains unknown, but is proven through other means of characterization described in sections 3.2.3 and 3.2.4.

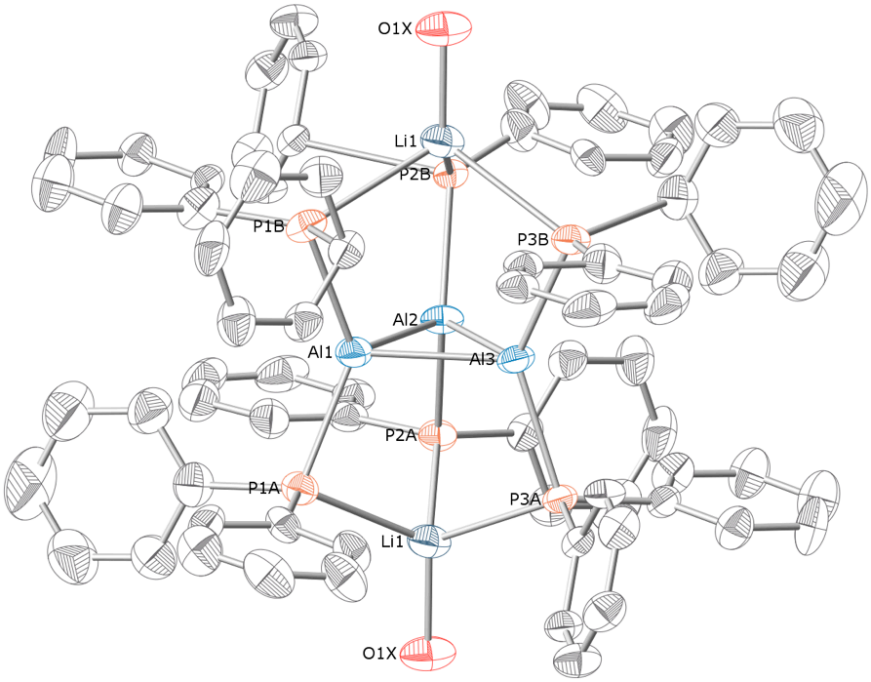

Figure 3.1. Single crystal X-ray strucutre of $[LiOEt_2]_2[HAl_3(PPh_2)_6]$, drawn at 50% probability level; Al = light blue, P = orange, Li = dark blue, O = red, C = gray, hydrogen has been omitted for clarity. Only one of the two orientations is shown for clarity.

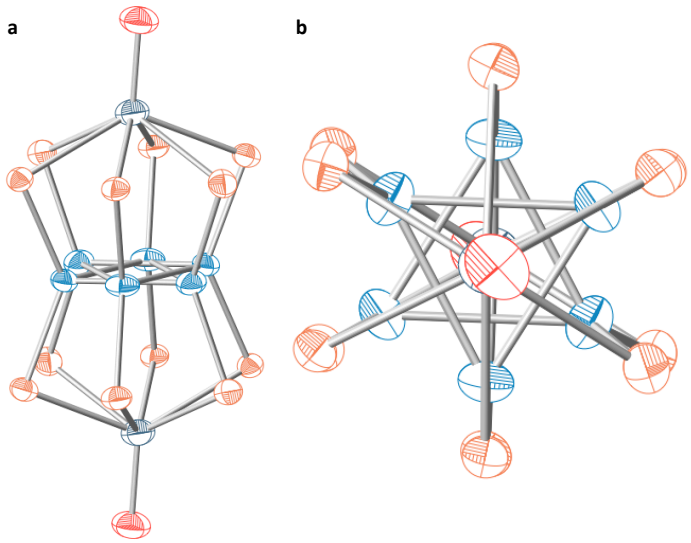

Figure 3.2. The equally populated orientations of the aluminum phosphide core (Al = light blue, P = orange, Li = gray, O = red), $Al_3(PPh_2)_6$, highlighting the dual orientations of aluminum and phosphorus (a) Vertical view (b) View down the Li-OEt_2 axis (only one orientation for oxygen shown, for clarity).

The cluster exhibits virtual D_{3h} point symmetry; the principal 3-fold rotation axis resides along the Li–O bonds and passes through the center of the Al_3 trimeric core. There are two equally populated orientations of the aluminum phosphide core that are offset by a 60° rotation about the 3-fold rotation axis of the cluster (Figure 3.2). The only atoms within the structure that do not exhibit disorder are the Li^+ ions. The solid-state structure was refined against data collected at the UMD X-ray facility and the X-ray synchrotron facility at Argonne National Lab (ANL).

The aluminum phosphide core consists of a planar Al_3 trimer with average Al–Al distances of 2.625(8) Å and an average Al–Al–Al bond angle of 60.0±0.3°. Each Al atom is four-coordinate, bound to the other two aluminum atoms in the ring and two phosphide ligands above and below the Al_3 plane. These Al atoms display distorted tetrahedral geometry as well. The six four-coordinate phosphorous atoms exhibit distorted tetrahedral geometry. Each phosphorous atom is coordinated to two phenyl rings, one

aluminum atom and a Li atom (P–Li bond distance averages 2.704(7) Å). The lithium atoms are also bound in a distorted tetrahedral geometry, coordinated by three PPh_2^{1-} ligands and a disordered Et_2O (Li–O bond distance = 1.926(1) Å) molecule, which caps both sides of the Al_3 plane (Figure 3.1). The average Al–Al distances are similar to those in the Al_3 plane of the $[Al_7(N(SiMe_2Ph)_2)_6]$ cluster. Within this structure there are two Al_3 planes, which have equal bond lengths (2.61 Å) as opposed to shorter distances in the Al_3 planes in the anionic $[Al_7(HMDS)_6]^{1-}$ (2.54 Å) complexes. The different Al–Al bonding in the Al_3 subunits of the Al_7 structures is attributed to the additional electron present in the neutral Al_7 complex.[21]

The $[HAl_3(PPh_2)_6]^{2-}$ cluster anion is best described as an 18 electron cluster complex containing three Al^{1+} atoms in a 6 electron Al_3 ring. Counting the hydrogen as H^+ (zero electron donor), each PPh_2^{1-} and Al^{1+} contributes 2 electrons to give 18 total electrons. The six-electron Al_3 ring contain contains 3 Al–Al two-center, two-electron (2c–2e) bonds and is similar to other known Al_3 rings.[120,122] The cluster is diamagnetic with metric parameters that are in agreement with DFT studies performed by calculations performed by Boggavarapu and Kandalam (not included in this thesis).[123]

Because the hydrogen atom was not crystallographically located, the $Al_3(PPh_2)_6^{2-}$ cluster without the H atom appears to contain 17 electrons (12 e^- from the 6 PR_2^{1-}, 5 e^- from 2 Al^{1+} and 1 Al^{2+}), giving each Al an average oxidation state of +1.33. The resulting Al_3 ring would contain a non-integral bond order and would be a spin $^1/_2$ radical species with a 5 e^- trimeric core. This radical core should make it directly comparable to the previously documented radical Al_3 cluster, isolated by Wiberg *et al.* in 2000. However, in Wiberg's structure the Al_3 core undergoes the expected Jahn-Teller

distortion, yielding two elongated Al–Al bonds and one short Al–Al bond. The absence of any structural distortion from D_{3h} symmetry in **3.1** and the extensive analytical data given below clearly shows that a hydrogen atom is present in the isolated complex and the cluster is not paramagnetic.

Table 3.1. Selected crystallographic data for $[LiOEt_2]_2[HAl_3(PPh_2)]$[a]

chem formula	$C_{87}H_{88}Al_3P_6Li_2O_2$
fw	1446.21
space group	$P\bar{1}$
a, Å	12.8213(10)
b, Å	13.7634(11)
c, Å	13.9032(11)
α, deg	95.5268(13)
β, deg	107.2191(12)
γ, deg	117.4940(12)
V, Å^3	1998.7(3)
Z	1
T, K	80(2)
ρ calcd g/cm^3	1.202
Reflns collected/$2\Theta_{max}$	27162
F(000)	761
R_1, GOF[b]	0.0722/1
R_2 ((I >2σ(I))	0.1407
$\Delta\rho_{max}$, $\Delta\rho_{min}$ (e/Å^3)	0.244/ -0.512

[a]Observation criterion: I>2σ(I). $R_1 = \sum \| F_o| - F_c \| / \sum |F_o|$ [b] GOF = $\{\sum[w(F_o^2 - F_c^2)^2]/(n-p)\}^{1/2}$ [c]$wR_2 = \{\sum[w(F_0^2 - F_c^2)^2]/\sum[w(F_o^2)^2]\}^{1/2}$

Table 3.2. Selected bond distances and angles in $[LiEt_2O]_2[Al_3(PPh_2)_6]$

Atoms	Bond Distance Å	Atoms	Bond Distance Å	Atoms	Bond Angle °
Al1-Al2	2.617(2)	Al3-P3B	2.367(1)	Al-Al-Al	60.0 ± 0.3
Al2-Al3	2.633(2)	P1A-Li	2.646(2)	P-Al-P	134.0±0.5
Al1-Al3	2.617(2)	P1B-Li	2.689(1)	C-P-C	109.8±1.3
Al1-P1A	2.368(1)	P2A-Li	2.702(2)	P-Li-P	102.9±1.6
Al1-P1B	2.368(2)	P2B-Li	2.720(1)		
Al2-P2A	2.369(2)	P3A-Li	2.677(2)		
Al2-P2B	2.379(1)	P3B-Li	2.788(4)		
Al3-P3A	2.368(3)	Li-O	1.926(1)		
		P-C	1.833(12)		

The powder form of **3.1** was analyzed via XRD, and the complexity of the crystal structure is reflected in the corresponding XRD-pattern. The pattern is complex, with numerous reflections. There are distinct identifying peaks at 14.50°, 15.58°, 16.79°, 17.24°, 17.90°, 18.79°, 19.64°, 20.18°, 20.59°, 21.04°, 28.70°. These angles correspond to reflections of the 2 0 0, 2 0 $\bar{2}$, 2 $\bar{1}$ 1, 1 0 2, $\bar{1}$ 2 2, 0 1 $\bar{3}$, 2 1 $\bar{2}$, 3 $\bar{1}$ 1, and $\bar{4}$ 1 2 respectively (Figure 3.3).

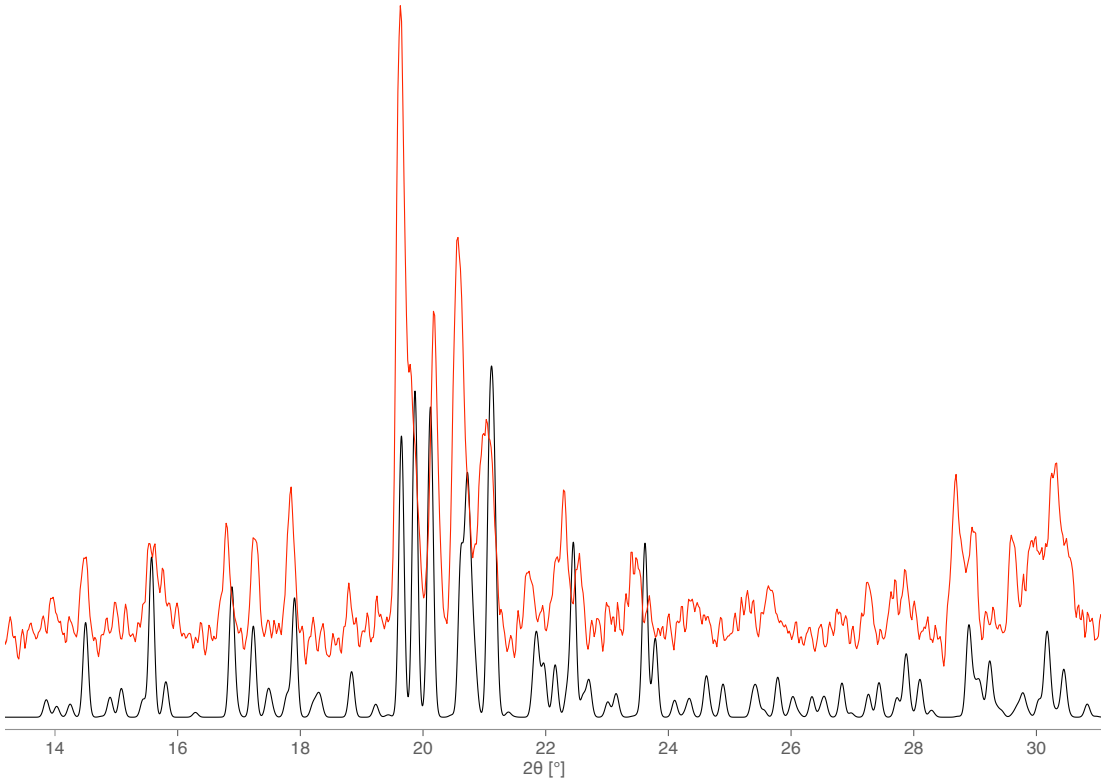

Figure 3.3. XRD pattern for powder of $[LiOEt_2]_2[HAl_3(PPh_2)_6]$ calculated (black) observed (red).

3.2.3 Electron-spray Ionization Mass Spectrometry (ESI-MS)

Electrospray ionization mass spectrometry was performed on the samples of **3.1** dissolved in THF and THF-d8. A representative negative ion ESI-mass spectrum of $[LiOEt_2]_2[HAl_3(PPh_2)_6]$ in THF is shown in Figure 3.4.

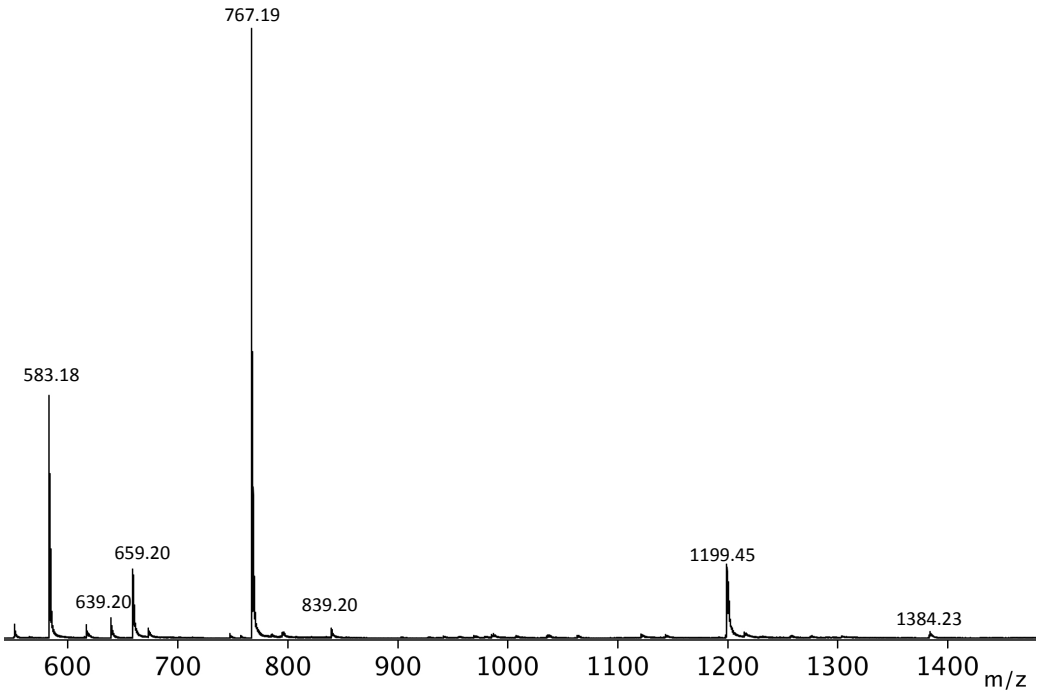

Figure 3.4. Negative ion ESI mass spectrum of in $[LiOEt_2]_2[HAl_3(PPh_2)_6]$ in THF.

Data were collected from multiple samples that were prepared from crystalline material of **3.1** dissolved in THF. The full spectrum shows extensive fragmentation of the cluster. The most intense monoanion is observed at ≈ 767 m/z which corresponds to the $[Al(PPh_2)_4)]^{1-}$ ion. This envelope also serves as an internal standard with each data collection. The largest mass envelope appears at 1384 m/z, which is attributed to the anion $[Li_2H_6Al_6(PPh_2)_6(C_7H_8)]^{1-}$ (Figure 3.5 (a) & (c)). The largest peak that is directly attributable to the solid-state state structure is 1199 m/z, which has been attributed to the anion $[LiHAl_3(PPh_2)_6]^{1-}$ (Figure 3.5 (b) & (d)).

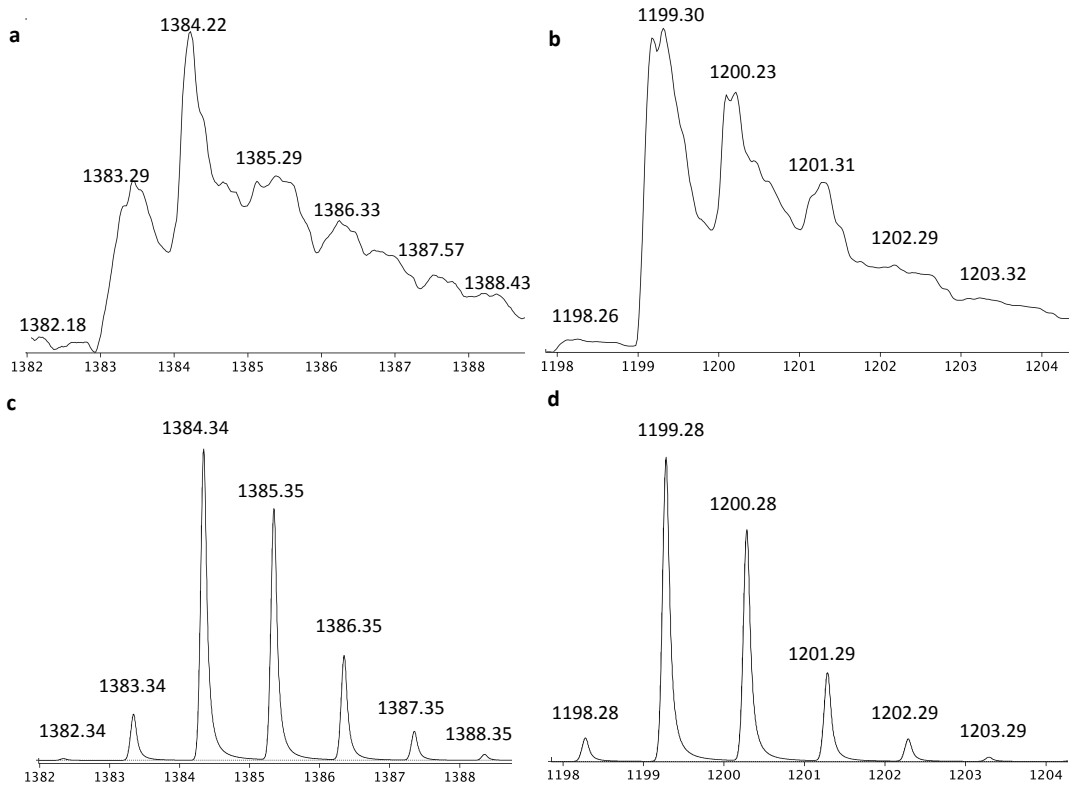

Figure 3.5. High molecular weight peaks from $[LiOEt_2]_2[HAl_3(PPh_2)_6]$ dissolved in THF (a) 1384 m/z (b) 1199.30 m/z (c) Calculated spectrum for $[Li_2H_6Al_6(PPh_2)_6(C_7H_8)]^{1-}$ (d) Calculated spectrum for $[LiHAl_3(PPh_2)_6]^{1-}$ (y-axis = m/z).

De-convolution of the mass envelopes through simulation provides reasonable estimates of the constituent cluster species. Smaller mass peaks at 583 and 639 m/z are attributed to $[Al(PPh_2)_3H]^{1-}$ and $[Al_3(PPh_2)_3H_3]^{1-}$. In order to exclude that hydrogen abstraction of THF is occurring when **3.1** is dissolved THF, the mass spectrum of **3.1** dissolved in THF-d8 was collected. The spectrum in deutero-THF shows no shift from samples dissolved in proteo-THF, leading to the conclusion that the H present is part of the solid-state structure of **3.1** and not due to solvent effects. This experiment demonstrates that the H atom of $[LiOEt_2]_2[HAl_3(PPh_2)_6]$ is present in the crystalline material is not a result of hydrogen abstraction from the THF solvent when dissolved in solution.

3.2.4 NMR Studies

Multinuclear, multidimensional (^{1}H, ^{31}P, ^{13}C, and ^{7}Li) NMR experiments of **3.1** in THF-d8 reveal the presence of a diamagnetic complex containing coordinated PPh_2 ligands and an Al–H moiety. In addition, ^{31}P, ^{7}Li, and ^{1}H diffusion-ordered spectroscopy (DOSY) and ^{31}P NMR titration experiments were performed on both $LiPPh_2$ and **3.1**.to confirm the composition of cluster and resolve a complicated accidental degeneracy of a free ligand peak.

3.2.4.1 1D NMR

The ^{31}P spectrum of **3.1** contains a single peak at -23 ppm that is coincidental with the $LiPPh_2$ starting material. The literature values for $LiPPh_2$ in ^{31}P NMR range from δ = -21.5 to -38 ppm depending on the starting material, preparation, and solvent environment for the salt.[124-126] In our lab, the $LiPPh_2$ salt, in THF-d8, routinely appears in the range of -21 to -24 ppm, depending on concentration, and is coincident with the peak observed for **3.1**. Titration experiments and DOSY experiments described below confirm this conclusion.

3.2.4.1.1 ^{1}H NMR experiments

^{1}H spectra of **3.1** show peaks in the same regions as $LiPPh_2$, including a convoluted aromatic region. The only major difference between **3.1** and $LiPPh_2$ in ^{1}H NMR is a broad peak at 4.40 ppm due to the aluminum hydride (* Figure 3.6).[127] This peak is not due to unreacted phosphine, $HPPh_2$, which appears as a doublet, at 5.40 and 4.90 ppm.

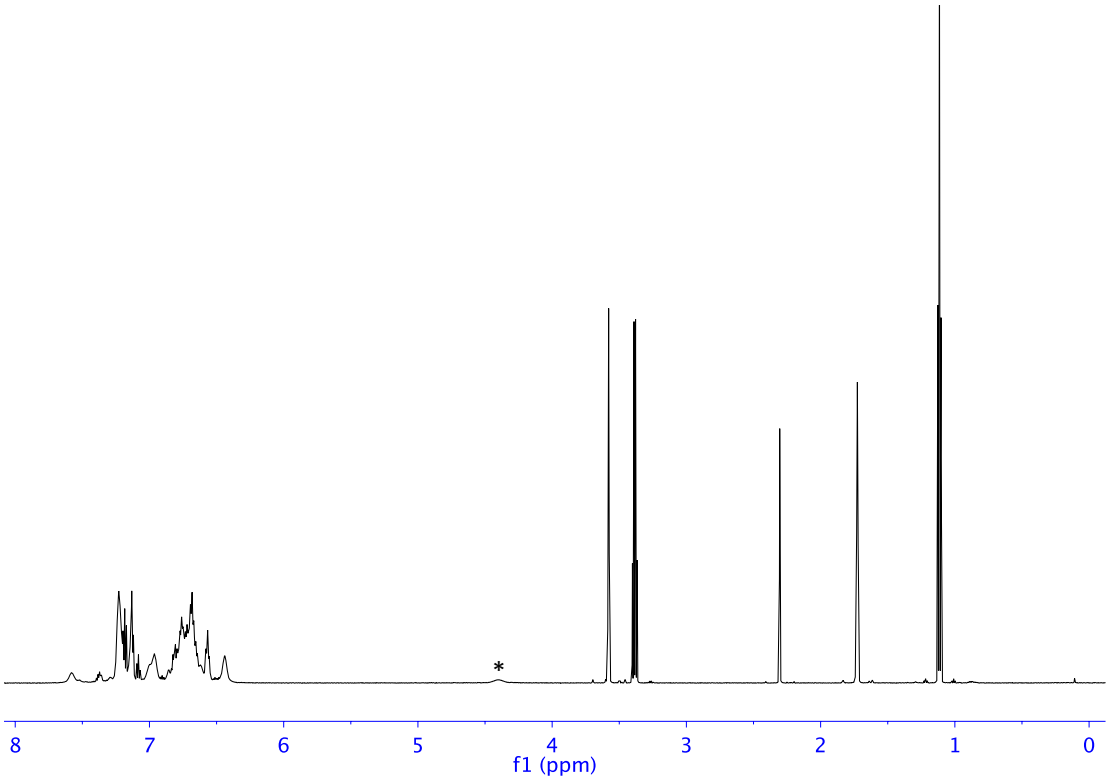

Figure 3.6. ^{1}H-NMR of $[Al_3(PPh_2)_6]^{2-}$ in THF-d8, * indicates broad peak (4.40 ppm) being attributed to Al-H bond.

The Al-H peak integrates to a value of one hydrogen relative to the Et_2O and the toluene solvate (Table 3.3).

Table 3.3. Proton assignments and associated integrations for chemical shift (aromatic region excluded due to inability specifically identify peaks)

Signal	Proton	Shift (ppm)	Integration	Expected Integration
H	Al-H	4.40	1.00	1.00
Et_2O	CH_3	3.38	10.03	9.00
	CH_2	1.11	6.66	8.00
Tol	CH_3	2.31	2.91	3.00

3.2.4.2 ^{31}P NMR titration experiments

Titration experiments were employed to probe whether the ^{31}P peaks for $LiPPh_2$ and **3.1** occur at the same chemical shift. In these titration experiments a known amount

of **3.1** or $LiPPh_2$ were dissolved in THF-d8 containing a known amount of an internal standard (PPh_3). The expected molar values were calculated based on the masses of material added and corroborated with the integration values determined from the control spectra. Subsequently, an experiment was performed on a mixture of all three reagents. In this set-up a known amount of **3.1** was dissolved in THF-d8 containing a known amount PPh_3, the spectrum was collected and integrated (Figure 3.7a & b), after data collection a known amount of $LiPPh_2$ was dissolved in the sample creating a mixture of **3.1**, $LiPPh_2$, and PPh_3. In this spectrum, the peak of interest (≈-23 ppm) grows proportionally in intensity, broadens and shifts 0.2 ppm (Figure 3.7c).

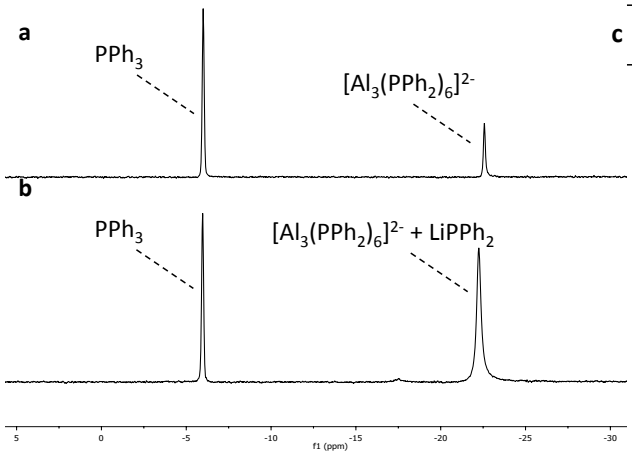

c

Peak	Integration	Expected Integration
PPh_3	1.00	1.00
$[Al_3(PPh_2)_6]^{2-}$	0.36	0.36
PPh_3	1.00	1.00
$[Al_3(PPh_2)_6]^{2-} + LiPPh_2$	1.21	1.16

Figure 3.7. ^{31}P titration experiments at room temperature: (a) Mixture of PPh_3 and $[LiOEt_2]_2[Al_3(PPh_2)_6]$ (b) Mixture of PPh_3, $[LiOEt_2]_2[Al_3(PPh_2)_6]$, and $LiPPh_2$. (c) Signal assignments and associated integrations for chemical shift. The peak at ≈ -20 ppm grows correspondingly with addition of $LiPPh_2$.

This finding demonstrates that both compound **3.1** and $LiPPh_2$ give ^{31}P NMR signals at ≈-23 ppm. Because of the accidental degeneracy of chemical shift, we were unable to discern if the PPh_2 ligands of **3.1** are in dynamic exchange with free ligand.

3.2.4.3 Diffusion NMR studies

Due to the extreme similarities in the ^{1}H and ^{31}P NMR spectra of both the cluster **3.1** and $LiPPh_2$, diffusion ordered spectroscopy (DOSY) NMR studies were performed on the independent species (**3.1** and $LiPPh_2$), and also a mixture of the cluster and ligand together. It was found that $LiPPh_2$ and **3.1** do diffuse at different rates and have correspondingly different hydrodynamic radii (r_H).

DOSY NMR is (a 2-dimensional method) is a way to visualize the diffusion coefficients in solution via NMR pulse gradient spin echo experiments (PGSE) to provide particle size of the molecules.[128] Diffusion coefficients (D) have proven to be a useful tool; D is a unique identifier for different substances.[129] Diffusion coefficients share a connection with the structural properties of a substance, and is dependent upon friction factors, a relationship is demonstrated through the Debye-Einstein theory (Eq. 4.2).

$$D = \frac{k_b T}{f_T} \tag{3.2}$$

where k_B is the Boltzmann constant, T, is the absolute temperature (K), and f_T is the friction factor, which is, dependent on the size and shape of the molecule.[129,130] For instance, if it is assumed that the particle is spherical and has a radius r_H in a solvent of viscosity η, the friction factor is given by Eq. 4.3.[129,130]

$$f_T = 6\pi\eta r_H \tag{3.3}$$

The PGSE NMR method was first introduced by Stejskal and Tanner.[131] The simplest method of this experiment is based on spin-echo sequence, described above. This sequence consists a 90° pulse followed by a 180° pulse, along with two pulsed field gradients, separated by a waiting time (Figure 3.8(a)). The purpose of the two gradients is to defocus and subsequently refocus the magnetization. If during the waiting time (delta) the molecules diffuse from their original positions after the first gradient, the

effective magnetic field experienced by the spins will be different during both gradients.[131,132] The result of this is an incomplete refocusing of the spins and consequent decrease in the intensity of the resulting NMR signals (Figure 3.8 (b)).

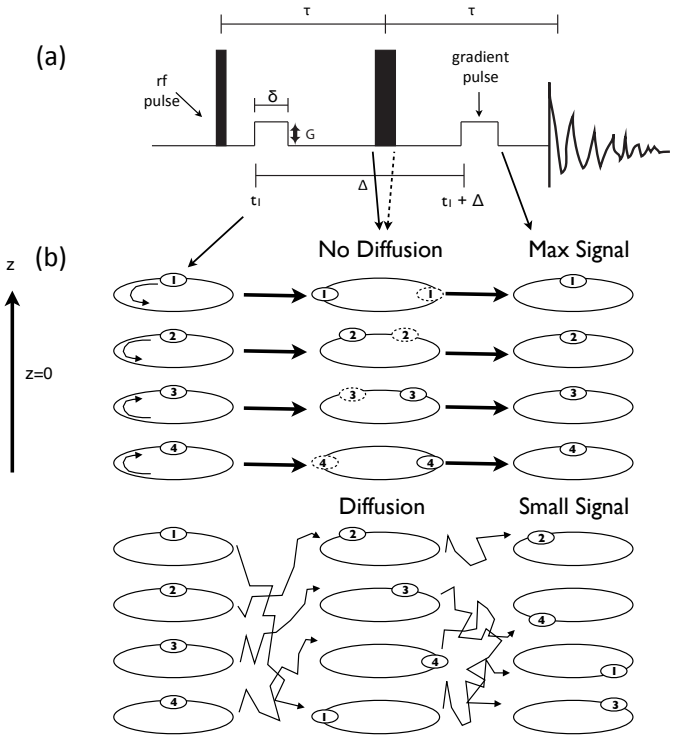

Figure 3.8. (a) Standard Stejskal-Tanner pulse sequence for PGSE (b) The effect of gradient pulse when there is no diffusion (top) and whenre there is diffusion (bottom).

Repetition of the experiment with increasing gradient strengths G affords a set of signal intensities from which the diffusion coefficient D can be obtained (Equation 3.4).[131,133]

$$\ln\frac{I}{I_0} = \gamma_x \delta^2 G^2 \left(\Delta - \frac{\delta}{3} \right) D \tag{3.4}$$

Where I is the observed intensity, I_0 the reference intensity, γ_x is the gyromagnetic ratio of the X nucleus, δ is the length of the gradient pulse, G is the gradient strength, Δ is the delay between the midpoints of the gradients, and D is the diffusion coefficient. Molecules (or ions) that possess larger volumes will diffuse slower than smaller species

and afford smaller slopes in the corresponding plots. DOSY is observed as being the two-dimensional visualization of PGSE NMR experiments. This technique provides a 2D map in which one axis is the chemical shift with the vertical axis is the diffusion coefficient.

^{1}H, ^{7}Li, and ^{31}P DOSY data collected for **3.1** and $LiPPh_2$ and a mixture of the two, a summary of these results are listed in Table 3.4.

Table 3.4. Diffusion constant values and r_H (Å) of $LiPPh_2$ and **3.1** in THF-d8

Sample	Nucleus	D ($m^2 sec^{-1}$)[a]	r_H[b]
$LiPPh_2$ (10 mM)	^{7}Li	1.13×10^{-9}	4.20[c]
	^{1}H	1.80×10^{-9}	1.32[d]
	^{31}P	7.09×10^{-9}	0.67
$[LiOEt_2]_2[Al_3(PPh_2)_6]$ (10 mM)	^{7}Li	8.70×10^{-10}	5.45[c]
	^{1}H	2.22×10^{-9}	1.94
	^{31}P	2.52×10^{-9}	1.88
$[LiOEt_2]_2[Al_3(PPh_2)_6]$ + $LiPPh_2$ (20 mM)[e]	^{7}Li	--	--
	^{1}H (4.40 ppm)	1.22×10^{-9}	3.88
	^{31}P	--	--

[a]Values from SimFit program from Bruker based off of PGSE fitting reports; [b]r_H determined from Stokes Einstein equation, $D = kT/6\pi\eta r_H$; [c]Diffusion constant is significantly smaller for both the ligand and **3.1** leading to a larger r_H value, a similar phenomena was found in Pregosin's study [d]Based off of the aromatic region, hard to get a good fit to solve for D [e]Mixture analyzed was at twice the concentration of the pure ligand and **3.1** analyses, ^{7}Li and ^{31}P could not be accurately determined due to coincident peaks

When analyzing the ^{31}P spectra of **3.1**, it was found that only one species could be attributed to the peak in the ^{31}P DOSY (at ≈ -23 ppm) with r_H = 1.88 based on the diffusion coefficient of 2.52×10^{-9} m^2s^{-1}. This value is more than two times that determined through a similar analysis performed on $LiPPh_2$ (r_H = 0.67, D = 7.09×10^{-9} m^2s^{-1}) at the same concentration. An exhaustive ^{31}P DOSY study by Pregosin *et al.* found

an r_H value of 4.7 for $LiPPh_2$ when dissolved in THF, but these analyses were performed on a 60 mM sample. Our analyses were performed on 10 mM $LiPPh_2$ samples differing from those in the Pregosin study.[134] Further, diffusion rates are concentration dependent.[135]

In the ^{7}Li DOSY studies both **3.1** and $LiPPh_2$ had larger r_H values (Table 3.4), and that **3.1** diffuses slower than $LiPPh_2$ indicative of a larger species in solution as observed in a Stejskal–Tanner plot of the experimental peak areas, (Figure 3.9).

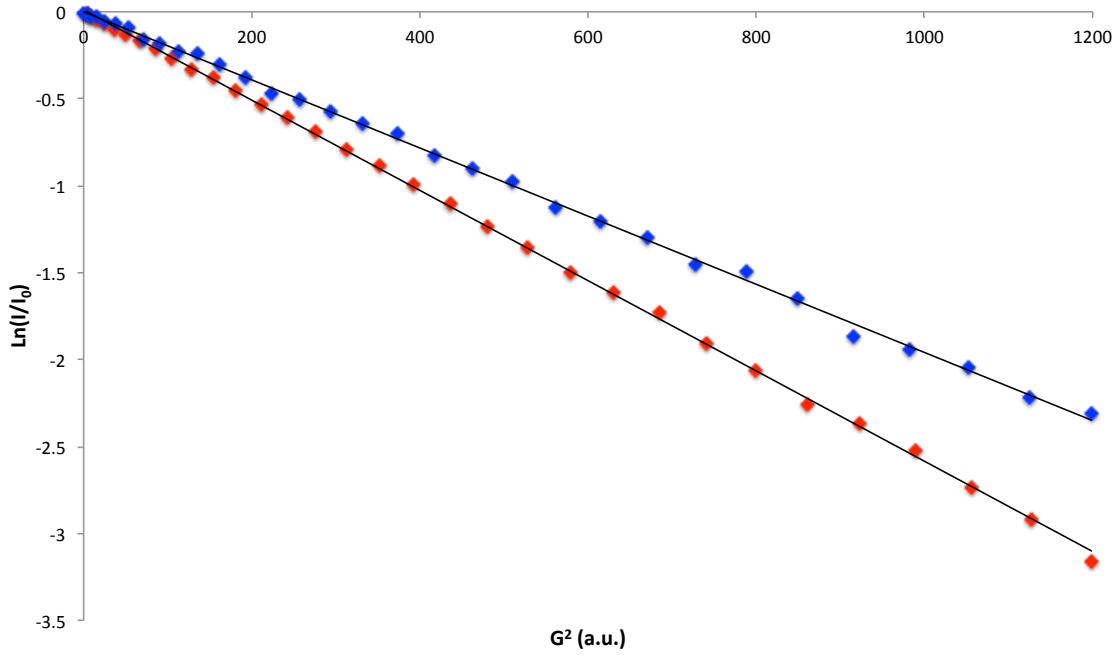

Figure 3.9. A Stejskal-Tanner plot of experimental peak areas for the ^{7}Li DOSY NMR: I = observed intensity, I_0 = reference intensity, G = square of the gradient amplitude; Blue = $[LiOEt_2]_2[Al_3(PPh_2)_6H]$, Red = $LiPPh_2$, both data sets collected in THF-d8.

Because of the difficultly of measuring diffusion coefficients on a coincident peaks via DOSY, we employed ^{1}H DOSY on 1:1 mixture of **3.1** and $LiPPh_2$ where the peaks are discernable. Our analysis focused on the peak at 4.40 ppm that is unique to **3.1** (Figure 3.10 *). In analyzing the mixture via DOSY there are three distinct regions of diffusion. In decreasing order of diffusion coefficient we have: **3.1**, $LiPPh_2$ and solvents (toluene,

Et_2O, and THF). It has been established in other DOSY experiments that there is a linear correlation between diffusion and molecular weight, when comparing different species in a mixture.[136] When using the diffusion values obtained from the mixture's ^1H DOSY and corresponding molecular weight a near linear plot arises ($R^2 = 0.98448$) as shown in Figure 3.11.

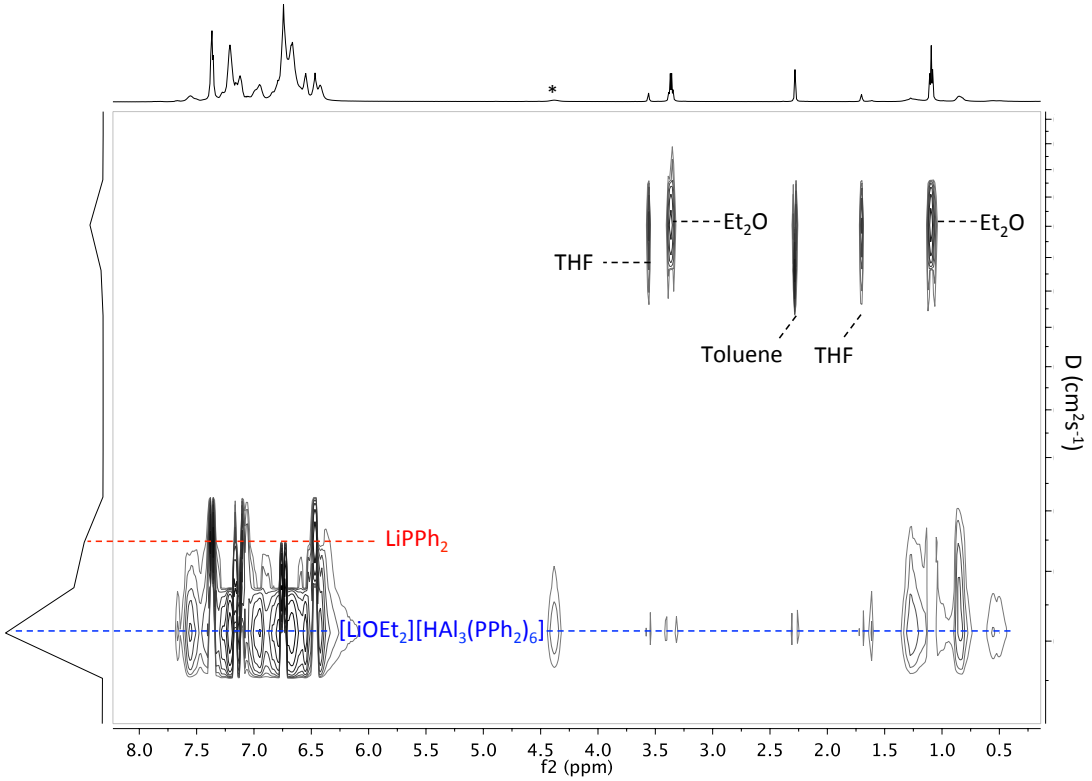

Figure 3.10. ^1H DOSY spectrum of $[LiOEt_2]_2[HAl_3(PPh_2)_6]$ and $LiPPh_2$ in d8-THF. X-axis represents the ^1H chemical shift, and the y-axis represents the diffusion rate (cm^2s^{-1}).

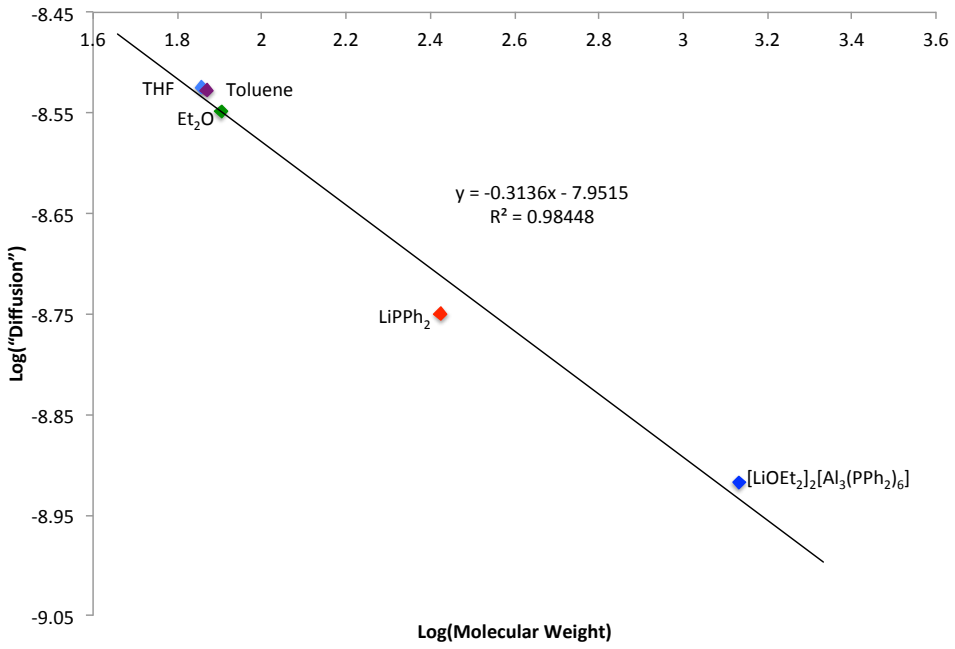

Figure 3.11. Log–log plot of mobility (diffusion, D) of different species in a mixture of as a function of formula weight (FW) [a], demonstrates the difference in diffusion of the various species present in the mixture, the relationship should be linear. [a]Formula weight of $LiPPh_2$ is for $LiPPh_2 \bullet Et_2O$

The DOSY experiments show that:

- **3.1** has a larger r_H and diffuses at a slower rate than $LiPPh_2$ at similar concentrations (10 mM) in THF.
- The peak in ^1H NMR attributed to the Al–H hydride diffuses at the same rate as the coordinated Et_2O and PPh_2 groups as **3.1** and slower than the solvents and the peaks associated with $LiPPh_2$ in solution in the aromatic region (refer to Figure 3.10). This observation further confirms the peak assignment of an Al hydride.

3.2.5 Magnetic Studies

3.2.5.1 Evan's method

The magnetic susceptibility of **3.1** was measured in solution by way of the Evan's NMR method. The cluster **3.1** is soluble in both THF and DMF, and demonstrates partial

solubility in less polar solvents (i.e. toluene and benzene). Crystalline **3.1** dissolved in pure DMF or DMF solvent mixtures degrade slowly over time as indicated by a loss of color in solution. In the Evans Method experiment, **3.1** is dissolved in proteo-THF and a capillary containing pure solvent is inserted into the sample as an internal reference. No shift in the solvent resonances is observed, indicating the absence of any paramagnetic species. When **3.1** was dissolved in DMF solvent mixtures, paramagnetic species are sometimes observed during decomposition.

3.2.5.2 Electron paramagnetic resonance (EPR)

EPR analyses of **3.1** were performed in both the solid state and in THF solutions. No EPR signals were observed aside from one air-stable impurity in one of the crystalline samples.

3.2.5.3 Zero-field cooled d.c. magnetic susceptibility experiments

The magnetic properties of **3.1** were furthered studied via temperature dependent magnetic susceptibility from 2-300 K via superconducting quantum interference device (SQUID) magnetometry. Samples were sealed *in vacuo* in quartz capillaries and evaluated by powder XRD before and after the susceptibility measurements. Multiple analysis of different crystalline samples showed only diamagnetism at all temperatures studied. No discernible decomposition was observed after analysis.

3.3 Discussion

Reaction of $AlCl{\cdot}Et_2O$ with $LiPPh_2$ repeatedly yields $[LiEt_2O]_2[HAl_3(PPh_2)_6]$ in ca. 15% of crystalline material. The complex contains Al in the +1 oxidation state and contains three 2-center, 2-electron Al–Al bonds (Figure 3.12a). When modeling bonding

of **3.1** based on the idealized $[Al_3H_6]^{2-}$ the irreducible representations from symmetry operations for D_{3h} are obtained (Table 3.5):

Table 3.5. Irreducible representations for atomic orbitals in $[Al_3H_6]^{2-}$

D_{3h}		E	$2C_3$	$3C_2$	σ_h	$2S_3$	$3\sigma_v$	Mulliken symbols
3Al	s	3	0	1	3	0	1	e', a_1'
	p_z	3	0	1	3	0	1	e', a_1'
	p_x,p_y	6	0	-2	0	0	0	a_2', a_2",e',e"
6H	s	6	0	0	0	0	2	a_1', e', a_2", e"

The lowest energy orbitals inhabit six orbitals in Al–H bonding (12 electrons), the remaining 6 electrons occupy the Al–Al bonding orbitals. The HOMO for **3.1** is a filled e' set of orbitals (Figure 3.12b) and is supported by calculations performed by Boggavarapu and Kandalam.[123]

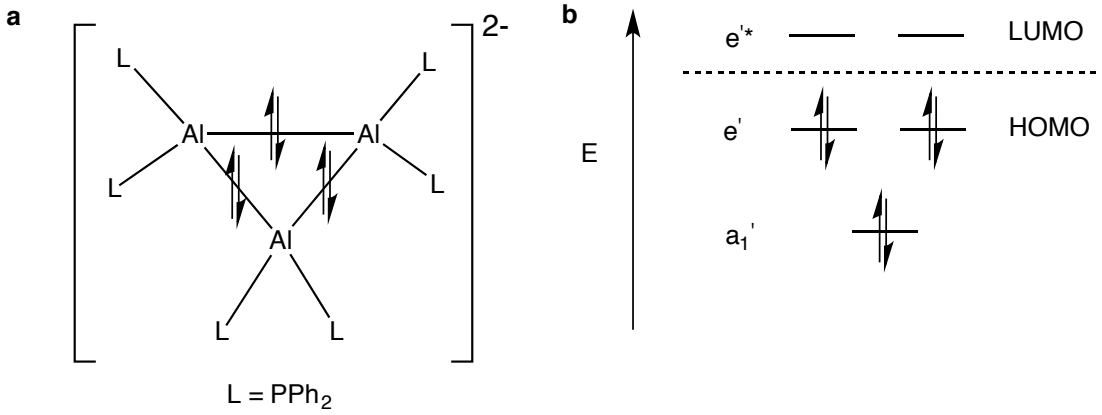

Figure 3.12. (a) Electron occupations in $[Al_3(PPh_2)_6]^{2-}$ core, 6 e^- in D_{3h}–Al_3 core resulting in 2c–2e bonding (b) Representation of the Al–Al bonding orbitals based on the irreducible representations for atomic orbitals isn $[Al_3H_6]^{2-}$, and calculations performed by Kiran and Anil.[123]

The symmetrical nature of **3.1** coupled with magnetic experiments and exhaustive NMR analyses support that **3.1** is diamagnetic. The aluminum trimer is not NMR silent and displays no properties associated with paramagnetism in the solid state. Diamagnetism of **3.1** can be attributed to a proton in the system that is not detected in the

solid-state structure. We believe this hydrogen is seen in the ^{1}H NMR at 4.40 ppm as a broad peak: this peak arises in a region similar to that of an Al–H bond in an aluminum hydride complex $[Al(NC_5H_6)_4][AlH_2(NC_5H_5)_4]$ (Al–H broad signal = 4.58, THF-d8).[127] This hypothesis is further supported by ESI-MS experiments run in both deutero- and proteo-THF where there is not discernable difference in the mass spectrum between the two samples, indicating the H is not due to solvent effects.

The formation and repeatable isolation of **3.1** on multiple occasions suggest high stability of the $[LiOEt_2]_2[HAl_3(PPh_2)_6]$ unit, which is an unusual feature of low oxidation state Al chemistry. This cluster is reminiscent of the $[Al_4(P(tBu)_2)_mX_{6-m}]$ clusters reported by Henke *et al.* (m = 5,6 X = Br; m = 5 X = Cl).[121] However, the average oxidation state of aluminum in these clusters is +1.5, in contrast to the 1+ oxidation state in **3.1**.[121] All three $Al_4(PtBu_2)_6$ compounds are synthesized using different AlX precursor solutions (all varying in concentration), yet all three have markedly similar structures. The clusters produced by Henke *et al.* have been cited as being phosphide derivatives of the Al_4H_6 structure that exists in the gas phase, and we believe that **3.1** is related these derivatives.[121]

At first glance the Al_3 core is structurally similar to $Na_2[AlAr"]_3$ (Ar"= C_6H_3-2,6-(C_6H_2-2,4,6-Me_3)$_2$), reported by Power *et al.* (Figure 3.13).

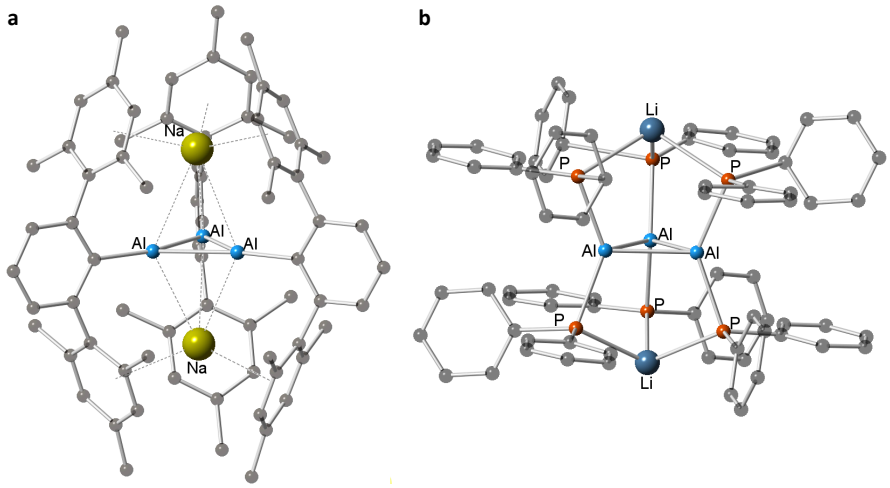

Figure 3.13 Side-by-side comparison (ball and stick model) of (a) $[AlAr"]_3^{2-}$ and (b) $[HAl_3(PPh_2)_6]^{2-}$ (C = black, H omitted for clarity). Comparison clearly shows the difference in the templating of the Al_3 cores by the alkali metals. Data for $[AlAr"]_3^{2-}$ from reference [122].

Both structures are highly symmetric, and the alkali cations are viewed as an integral part of the structure. Closer inspection highlights the distinction between **3.1** and $[AlAr"]_3^{2-}$. In Power's complex the Al_3 core directly interacts with sodium atoms. These sodium atoms are viewed as being an intrinsic part of the structure and participate in cation-π interactions with the Ar" ligands (average Na–$C_{centroid}$ = 3.177(2) Å) (Figure 3.12 (a)). [122] In **3.1** the lithium atoms are also considered to be part of the cluster structure, but do not directly interact with the aluminum core. The Li-atoms serve as template the formation of the Al_3 core, sharing electron density with the phosphorous atoms of the ligand.

The coordination environments of the aluminum atoms in each respective structure are also different. As discussed each Al-atom in **3.1** is 4-coordinate, pseudo-tetrahedral, bound to two PPh_2 ligands and two aluminum atoms to form the trimeric core. In $[AlAr"]_3^{2-}$ the Al-atoms are less coordinately saturated than in **3.1**. Each Al-atom

is described as having distorted trigonal-planar geometry, is bound to two Al-atoms and to an Ar" ligand through the *ipso*-C atom of the central aryl ring. These differences in structure and coordination explain why the Al–Al bonding in **3.1** is significantly different than that in $[AlAr"]_3^{2-}$ (Figure 3.12 (a) & (b)). If one were to only consider the covalent radii of aluminum atoms in **3.1** and $[AlAr"]_3^{2-}$ based on the average oxidation state, it would be expected that the bonds in **3.1** to be approximately the same to those in $[AlAr"]_3^{2-}$. In fact, the Al–Al bond lengths in **3.1** (2.625(8)Å) are significantly longer than the 2.520(1) Å Al–Al distances in $[AlAr"]_3^{2-}$ (Figure 3.14a & c). This discrepancy is largely due in part to the higher bond order in $[AlAr"]_3^{2-}$ (bond order = 1.33).

Although there is a difference in the Al–Al bonding both **3.1** and $[AlAr"]_3^{2-}$ demonstrate highly symmetrical Al_3 cores, and do not undergo Jahn-Teller distortion due to their diamagnetic nature (Figure 3.14). It should be noted that Jahn-Teller theorem predicts that any molecule with degeneracies in its ground state electronic structure will undergo a distortion to remove the degeneracy.[137] These distortions are termed first-order Jahn-Teller (JT) distortions.[10] This distortion, or lack thereof, has proved to be extremely important in the characterization of **3.1**. In the solid-state structure it is not immediately apparent that there is a H-atom present, but without its presence the structure would contain a radical $5e^-$ core similar to that of $[Al_3(SitBu_3)_4]^{\bullet}$ (two longer sides = 2.756 Å, shorter side = 2.703 Å) (Figure 3.13c). The expectation would be that the core of **3.1** would undergo JT distortion from the observed D_{3h} symmetry to that of C_{2V}.[8] This distortion has not been observed in the structural studies of **3.1**. Furthermore, in the solid-state structure of **3.1**, the thermal parameters of the Al-atoms are 'normal', indicating that there is not a 3-fold disorder of JT distorted structure.

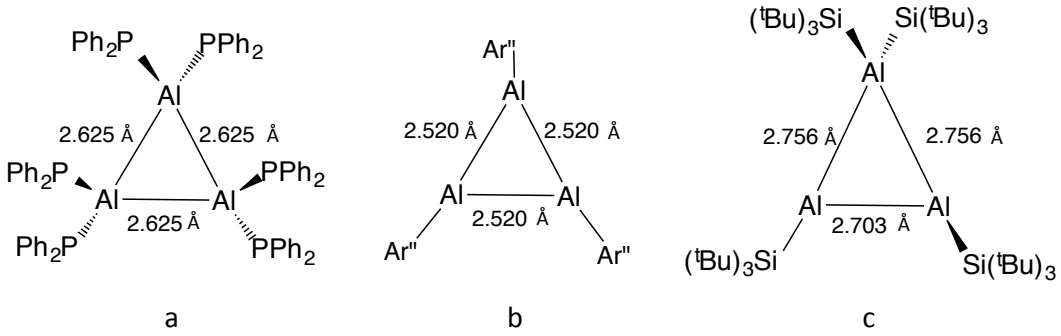

Figure 3.14. Comparison of the different trimeric cores (a) $[Al_3(PPh_2)_6]^{2-}$ (b) $[AlAr"]_3^{2-}$ (c) $[Al_3(S^tBu_3)_4]^{\bullet}$

Ultimately, the position of the H atom is still under investigation. The proton may be delocalized but appears to be bound to Al according to our NMR studies (i.e. broad peak at 4.40 ppm). This H atom is why **3.1** demonstrates diamagnetic properties instead of paramagnetism in both solid and solution states, yielding a final structural solution of $[LiOEt_2]_2[HAl_3(PPh_2)_6]$.

3.4 Conclusion

We have described the synthesis and characterization of $[LiOEt_2]_2[HAl_3(PPh_2)_6]$, an $18e^-$ aluminum trimeric cluster consisting of a $6e^-$ Al-core made up of 2c–2e bonds. The cluster is reproducible and is relatively high yielding when compared to other aluminum clusters isolated via the 'Schnöckel' route. The solid-state structure is highly symmetrical, and demonstrates unusual full molecule disorder.

The cluster, **3.1**, is a diamagnetic cluster, contradicting the expected paramagnetism that one would presume based on chemical formula deduced from the solid-state structure. However, the presence of an H atom makes **3.1** diamagnetic; which is supported by the lack of distortion that the core exhibits in the solid-state. Diamagnetism is further supported by NMR experiments that show that there are NMR

signals that are associated with **3.1** (^{1}H NMR peak at 4.40 ppm), and ESI-MS experiments demonstrate that the H that is present is not due to solvent effects. Experiments to determine the location of H within the structure of **3.1** are ongoing.

3.5 Experimental Details

General considerations: All reactions are performed under a dinitrogen atmosphere in a glovebox using standard Schlenk techniques. Toluene and diethyl ether were purified by distillation from sodium benzophenone ketyl under a dinitrogen atmosphere. All purified solvents were stored in modified Schlenk vessels over 3 Å molecular sieves under dinitrogen atmosphere. AlCl•Et_2O solutions were generated at 1100 K in a modified Schnöckel-type metal halide co-condensation reactor and stored at -80°C. The chloride content of the AlCl•Et_2O solutions was determined by Mohr titration.

$LiPPh_2$: $LiPPh_2$ was prepared using a modified procedure.[125] A solution of n-butyllithium (30 mmol, 12 mL of a 2.5 M solution in hexanes) was added dropwise to a solution of diphenylphosphine (28.7 mmol, 5.35 g) in diethyl ether (30 mL) at -78°C for 4 hours and then warmed room temperature and stirred overnight. The yellow solution was removed *in vacuo* and the yellow powder was pumped to dryness and washed with hexanes

$[LiEt_2O]_2[Al_3(PPh_2)_6]$ **(3.1)**: AlCl•Et_2O (1.56 mmol, 6.3 mL of a 248 mM solution 3:1 toluene:Et_2O (v:v), Al:Cl ratio 1:1.34) was added to $LiPPh_2$ (3.13 mmol, 0.6022 g) at room temperature and mixed overnight. The reaction mixture was then subsequently concentrated to $^2/_3$ its volume *in vacuo*. The resultant dark orange mixture was filtered via cannula, and heated to 65°C for 3 days. After 48 hours orange crystals of **3.1** formed on the walls of the Schlenk (15%).

Physical methods

Mass spectra: were collected on ACCUTOF ESI-MS at 3000 V in a THF solution utilizing our in-house introduction source (see-Appendices).

X-ray crystallographic analysis: Performed by Dr. Peter Zavalij at the University of Maryland. Graphite monochromated Mo Kα radiation (λ= 0.71073 Å) from a Mo-target rotating-anode X-ray source was used throughout. Data were corrected for absorption effects using the multi-scan methods, the structure was solved and refined using the Bruker transmission coefficients (based on crystal size) are 0.8720 and 0.9540.

Evan's Method experiments: Were performed in a mixed solvent of C_6D_6:DMF 5:1. A small amount of $[LiEt_2O]_2[HAl_3(PPh_2)_6]$ (16.6 mg, 0.0115 mmol) was dissolved in 2.5 mL of prepared standard and sealed in a J. Young NMR tube containing a capillary filled with blank solvent.

NMR: The ^1H NMR spectra were recorded at 294 K on a Bruker AM-400 spectrometer operating at 400.1 MHz using a BBI probe. ^1H and ^{31}P NMR spectra were recorded at 294.5 K on a Bruker DRX-500 MHz using a BBO probe. DOSY NMR experiments were recorded at 294 K, -54 K, -78 K, and -94 K and were performed on a Bruker AVIII-600MHz equipped with a BBO probe.

Chapter 4: Synthesis of low oxidation state Aluminum Thiolates from AlX precursors

4.1 Introduction

Aluminum cluster formation is highly dependent on the makeup of the precursor solution (both the identity of the halide and metal:halide ratio), the temperature of the reaction, order of the reaction steps, and ligand type. Part of the scope of this project was to explore ligand sets that had not been previously studied. Studies employed by Schnöckel *et al.* have investigated a variety of ligand types including η^5-carbon and carbon/phosphorus, amide, phosphide, and alkoxides ligands. In gold-cluster chemistry monodentate thiol ligands have proven to be fruitful in the isolation of high nuclearity gold clusters. In particular thiols have been shown to stabilize some of the largest known metalloid type clusters such as $Au_{102}R_{44}$ (R = *p*-MBA = *p*-Mercaptobenzoic Acid = *p*-S-C_6H_4COOH).[138] The success of these ligand types with gold led to the pursuit for similarly isolated metalloid aluminum clusters.

Fully oxidized aluminum, Al^{3+}, is considered a 'hard' acid due to its high charge and small ionic radius. Subvalent forms of aluminum, Al^{2+} and Al^{1+}, are softer in nature, and should pair well with softer ligands such as the thiolates. Reactions with the alkali salts of isopropyl thiol, t-butyl thiol, and substituted thiophenols were attempted (Figure 4.1).

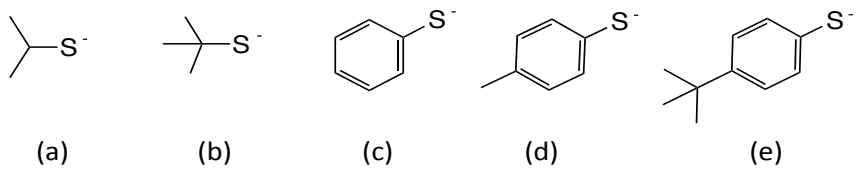

Figure 4.1. Various thiolate ligands reacted with AlX solutions in this study, counter-ions will be Li^+ or Na^+ (a) isopropyl thiolate (b) tert-butyl thiolate (c) thiophenolate (d) 4-methylthiophenolate (e) 4-tert-butylthiophenolate

To date, no low-valent aluminum thiolate clusters have been isolated. Reactions of aluminum with thiols via traditional reductive routes have been attempted in the literature. A large number of aluminum thiolate complexes have been prepared via salt elimination routes or reactions involving triorganoaluminum compounds, but there are few examples of homoleptic aluminum thiolate complexes.[139] Hoffman *et al.* reported an aluminum alkane thiolate complex, $[iPr_2NH_2][Al(StBu)_4]$ (Figure 4.2a). Soon after, Carmalt *et al.* reported reactions between alanes and thiols, which typically yield tetrahedrally coordinated Al^{3+} complexes.[140] In the reaction of $[AlH_3(NMe_2Et)]$ with 2,6-$Me_2C_6H_3SH$ the product was $[HNMe_2Et][Al(2,6\text{-}Me_2C_6H_3S)_4]$ (Figure 4.2b).[140]

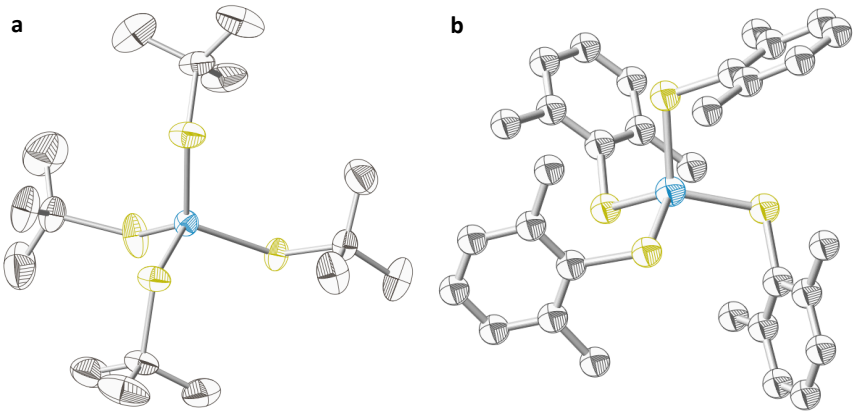

Figure 4.2. (a) $[Al(StBu)_4]^{-1}$ (b) $[Al(2,6\text{-}Me_2C_6H_3S)_4]^{-1}$ (Al = light blue , S = yellow, C = gray) [139, 140].

More, recently Power *et al.* have performed studies utilizing sterically hindered lithium terphenyl thiolates, $LiSAr^{Me6}$, (Ar^{Me6}= C_6H_3-2,6-(C_6H_2-2,4,6-Me_3)$_2$) with the goal of isolating low-valent aluminum complexes containing Al–Al bonding, but were unsuccessful and only able to isolate monomeric tetrahedrally-coordinated Al-complexes.[141] The dearth of structurally characterized low-valent aluminum thiolate complexes led to thiolate studies with the AlX solutions.

Described here are the synthesis and characterization of the aluminum (III) complex $Na[Al(SPh)_4]$ and solution studies of reactions of AlBr and Li(StBu) via ESI-MS. These studies have led to the identification of $[Al_{17}Br(StBu)_{10}S_3]^{1-}$, $[Al_{10}(StBu)_4S_5]^{1-}$, $[Al_{13}(StBu)_4BrS]^{1-}$, and $[Al_5(StBu)_7Br]^{1-}$ in solution.

4.2 Results

4.2.1 Na[Al(SPh)$_4$]

4.2.1.1 Synthesis of Na[Al(SPh)$_4$]

The complex $Na[Al(SPh)_4]$ (**4.1**) was synthesized through a reaction of $AlCl{\cdot}(Et_2O)_n$ with a 10% excess of NaSPh at room temperature (eq. 4.1).

$$3AlCl \bullet Et_2O + 4NaSPh \xrightarrow{65^\circ C} Na[Al(SPh)_4] + 2Al^0 + 3NaCl \qquad (4.1)$$

Colorless, needle-like crystals suitable for X-ray crystallography were grown over a three day period at 65 °C. Formation of aluminum metal was indicated by mirroring on the sides of the flask. Complex **4.1** has been characterized by single-crystal X-ray diffraction.

4.2.1.2 Solid-state structure of Na[Al(SPh)$_4$]

The single thiolate compound that has been both successfully isolated and structurally characterized from reactions with low-valent aluminum solution is **4.1**; which is isolated as triclinic colorless needles in spacegroup $P\bar{1}$ (Figure 4.3).

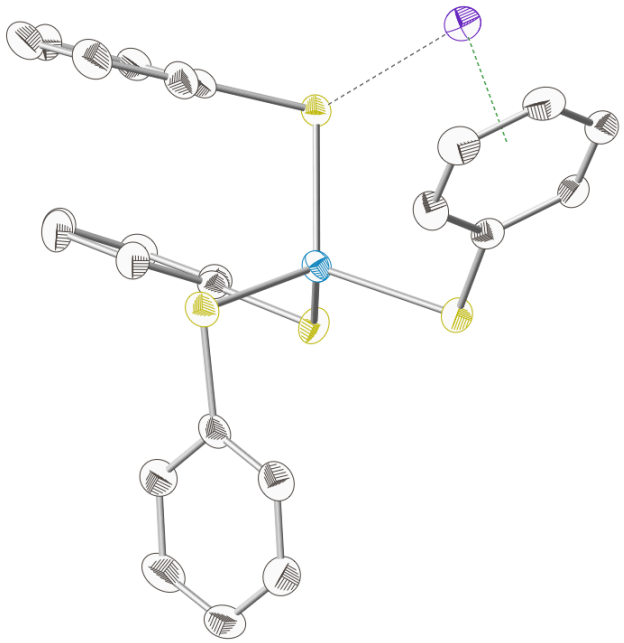

Figure 4.3. Structure of the salt $Na[Al(SPh)_4]$, thermal ellipsoids depicted at the 50% probability level. Hydrogen atoms have been omitted for clarity (Al = teal, S= yellow, C= gray, Na = purple)

The complex contains a central Al^{3+} atom tetrahedrally coordinated to four thiophenolate ligands, a formal charge of -1, that is balanced by a Na^+ ion. The average Al–S bond is 2.2552(7) Å and average S–Al–S bond angle of 109.38(3)°. The Al–S bond lengths are quite similar to the bond lengths in $[Al(SC_6H_3Me_2\text{-}2,6)_4]^-$ (average Al–S = 2.2573(5) Å) and $[Al(S\text{-}t\text{Bu})_4]^{1-}$ (average Al–S = 2.2588(15) Å).[139,140] A summary of the crystallographic data is given in Table 4.1.

Table 4.1. Selected crystallographic data for $Na[Al(SPh)_4]$[a]

Compound	$Na[Al(SPh)_4]$
chem formula	$C_{24}H_{20}AlNaS_4$
fw	486.61
space group	$P\bar{1}$
a, Å	8.2175(4)
b, Å	10.5599(6)
c, Å	13.5182(7)
α, deg	92.1832(8)
β, deg	96.1214(9)
γ, deg	97.4454(8)

V, Å^3	1154.93(11)
Z	2
T, K	150(2)
ρ calcd g/cm^3	1.399
Reflns collected/2Θ$_{max}$	5308
F(000)	504
R$_1$, GOF^b	0.0315/1.000
R$_2$ ((I >2σ(I))	0.0653
Δρ$_{max}$, Δρ$_{min}$ (e/Å^3)	0.354/ -0.233

[a]Observation criterion: I>2σ(I). $R_1 = \sum \| F_o| - F_c \| / \sum |F_o|$ [b] $GOF = \{\sum[w(F_o^2 - F_c^2)^2]/(n-p)\}^{1/2}$ [c] $wR_2 = \{\sum[w(F_0^2 - F_c^2)^2]/\sum[w(F_o^2)^2]\}^{1/2}$

Select bond distances and angles are in Table 4.1. The $NaAlPh_4$ unit repeats in a regular fashion, forming an extended solid linked by pi stacking and interactions with the Na^+ ion (Figure 4.4).

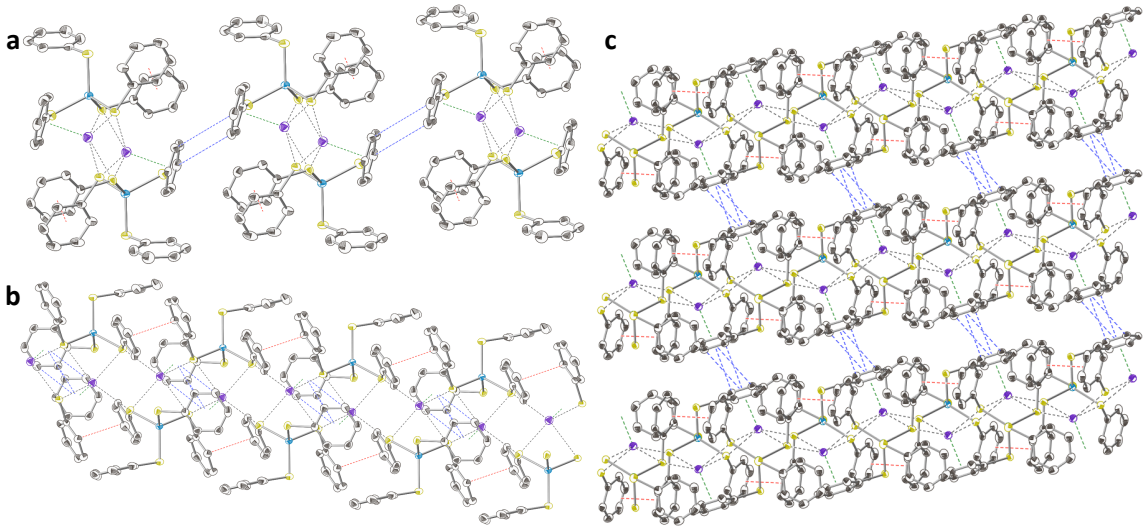

Figure 4.4. Interactions found between $Na[Al(SPh_4)]$ units within crystal lattice. View down (a) a-axis (b) b-axis (c) c-axis. Red dotted line indicates π—π (3.607 Å) interaction between $[Al(SPh)_4]^{1-}$ units in a single chain, blue dotted lines represent parallel offset between the two chains η^2 interactions (4.144 Å); Green dotted line represents Na-ion interaction with neighboring phenyl ring (2.644 Å); Gray dotted lines demonstrate pseudo square pyramidal orientation of Na (Al = teal, S = yellow, C = gray, Na = purple, H has been omitted for clarity).

This long range ordering further influences the orientation of the phenyl rings within the complexes. Pi-stacking interactions between neighboring complexes are propogated down the c-axis (Figure 4.4). Views down the b-axis shows that a Na-chain extends

infinitely down the length of the a-axis (Figure 4.4b). The Na–$C_{centroid}$ distance averages 2.644 Å (Figure 4.4, green dashed lines), and helps position the Na-atom so that it is the 'cap' of pseudo square pyramidal orientation with 4 neighboring sulfur atoms (Figure 4.4, gray dashed lines), average Na–S distances 2.989 Å. There are π–π interactions occurring between the thiophenol rings of neighboring complexes with a centroid to centroid distance of 3.607 Å (Figure 4.4 (b) and (c), red dashed lines). Furthermore, there are pi stacking interactions in parallel offset fashion between the 'polymeric' chains where the rings network in an η^2 mode with an average distance of 4.144 Å from the neighboring centroid (Figure 4.4c, blue dashed lines).[99,142] The polymeric nature of this species is analogous to the Al^{3+} phenyl, $LiAlPh_4$, complex isolated within our lab by Lauren Stevens.

4.2.2 Reactions of AlBr with Li[StBu]

4.2.2.1 Synthesis of $[Al_{17}Br(StBu)_{10}S_3]^{1-}$

The cluster $[Al_{17}Br(StBu)_{10}S_3]^{1-}$ (**4.2**) was produced from a reaction AlBr·THF with LiStBu at elevated temperature (65°C), represented in Eq.4.2.

$$AlBr + LiStBu \xrightarrow{65^{\circ}C} [Al_{17}Br(StBu)_{10}S_3]^{1-} \quad (4.2)$$

The cluster **4.2** was observed via ESI-MS.

4.2.2.2 Synthesis of $[Al_{10}(StBu)_4S_5]^{1-}$ and $[Al_{13}(StBu)_4BrS]^{1-}$

The clusters $[Al_{10}(StBu)_4S_5]^{1-}$ (**4.3**) and $[Al_{13}(StBu)_4BrS]^{1-}$(**4.4**) were produced from a reaction of AlBr· with LiStBu at room temperature, represented in Eq. 4.3.

$$AlBr + LiStBu \rightarrow [Al_{10}(StBu)_4S_5]^{1-} + [Al_{13}(StBu)_4BrS]^{1-} \quad (4.3)$$

These clusters **4.3** and **4.4** were observed via ESI-MS.

4.2.2.3 Synthesis of $[Al_5(StBu)_7Br]^{1-}$

The cluster $[Al_5(StBu)_7Br]^{1-}$ (**4.5**) was produced from a reaction of AlBr·THF with LiStBu at low temperatures (-78°C), represented in Eq 4.4.

$$AlBr + LiStBu \xrightarrow{-78^{\circ}C} [Al_5(StBu)_7Br]^{1-} + [Al(StBu)_2Br_2]^{1-} \quad (4.4)$$

This cluster **4.5** along with the complex $[Al(StBu)_2Br_2]^{1-}$ were observed via ESI-MS.

4.2.3 Electron Spray Ionization Mass Spectroscopy (ESI-MS) Studies

ESI-MS studies of reactions of AlBr with Li(StBu) has been employed. Preheating the AlBr·THF:Tol solution prior to the addition of Li(StBu) showed the presence of a metalloid cluster at 1525 m/z by ESI-MS, which matches the isotopic envelope of the anion $[Al_{17}Br(StBu)_{10}S_3]^{1-}$ (**4.2**) (Figure 4.5). Each aluminum atom has a +1 oxidation state and the presence a naked S^{2-} ion in the cluster, suggesting that ligand degradation occurred during the reaction. In the full spectrum some of the observed fragmentation peaks can be attributed to loss S^{2-} and $S(tBu)_2$, which further supports ligand decomposition. This degradation is also noted by isotopic envelopes at 1491 and 1557 m/z, which can be attributed to the loss of S^{2-} gain of S^{2-} to **4.2** respectively (Figure 4.5).

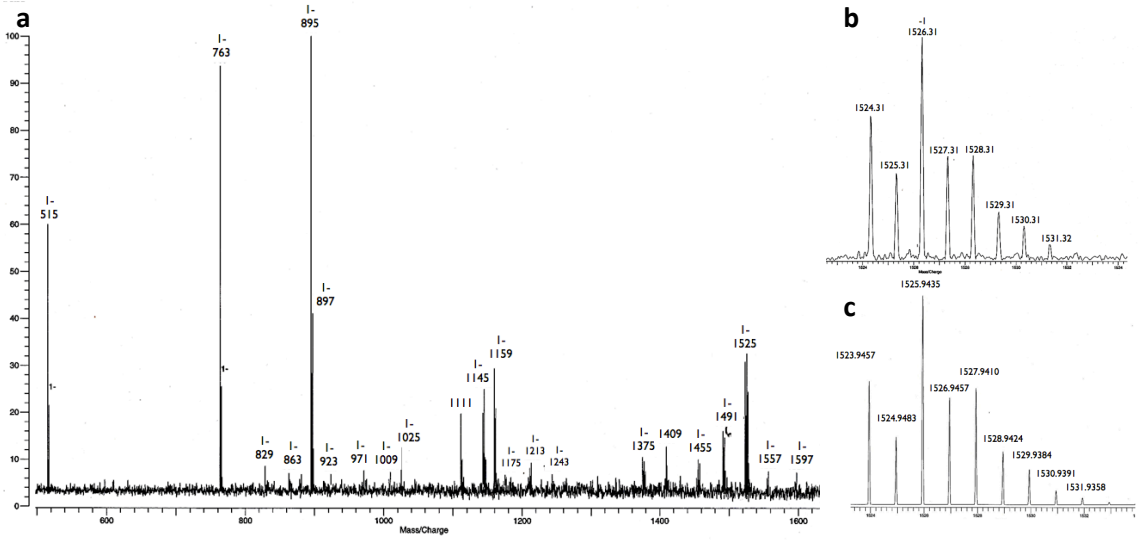

Figure 4.5 (a) Full spectrum of pre-heated AlBr·THF reacted with Li(StBu) (b) Experimental spectrum focused on envelope at 1525 m/z (c) Calculated spectra for anion $[Al_{17}Br(StBu)_{20}S_3]^{1-}$

The reaction of LiStBu and AlBr·THF at room temperature shows the presence of two different clusters $[Al_{10}(StBu)_4S_5]^-$ (**4.3**) (average Al oxidation state = +1.3) and $[Al_{13}(StBu)_4BrS]^-$ (**4.4**) (average Al oxidation state = +0.46) respectively (Figures 4.6).

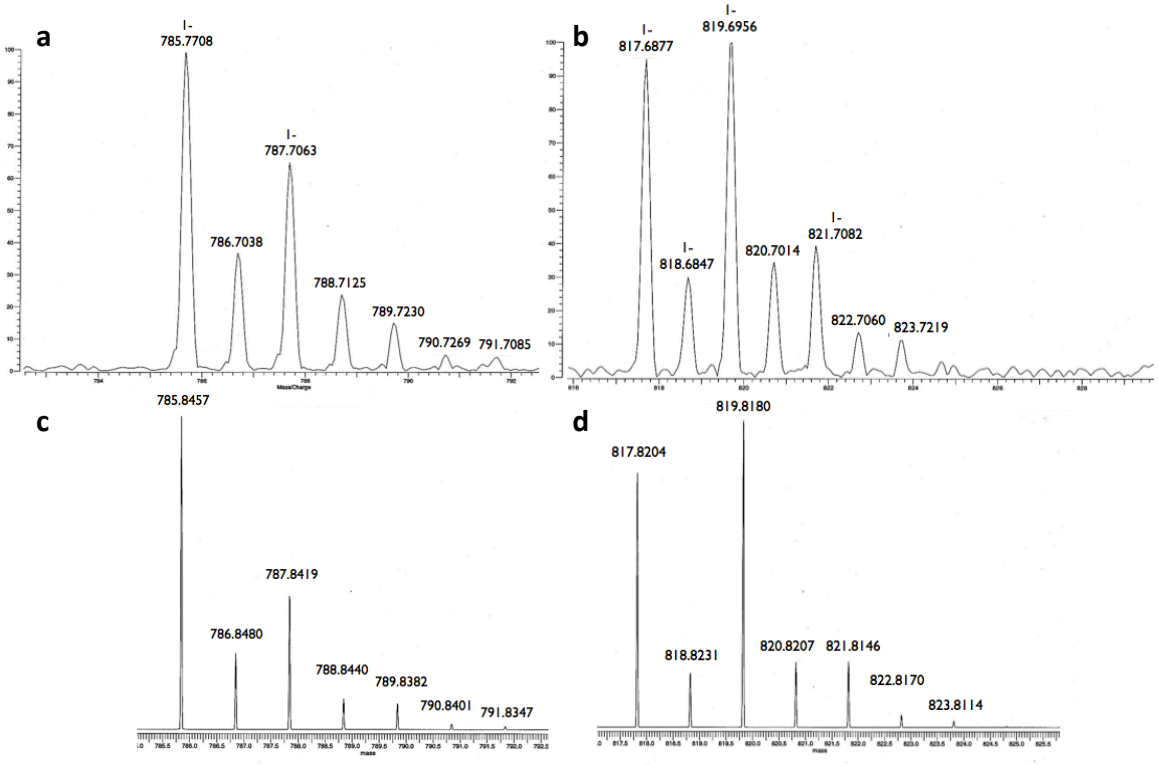

Figure 4.6. Isotopic envelopes from room temperature reaction of AlBr·THF and Li(StBu) at: (a) 785.77 m/z (b) 817.69 m/z (c) Calculated spectrum for anion $[Al_{10}(StBu)_4S_9]^{1-}$ (d) Calculated spectrum for anion $[Al_{13}(StBu)_4BrS]^{1-}$ (y-axis = m/z).

When AlBr·THF was added to LiStBu at low temperature, the parent ion $[Al_5(StBu)_7Br]^{1-}$ (**4.5**) (average Al oxidation state = 1.5+) at 839.17 m/z was detected. A tetrahedrally bound Al^{3+} product $[Al(StBu)_2Br_2]^{1-}$ is observed at 364.90 m/z (Figure 4.7).

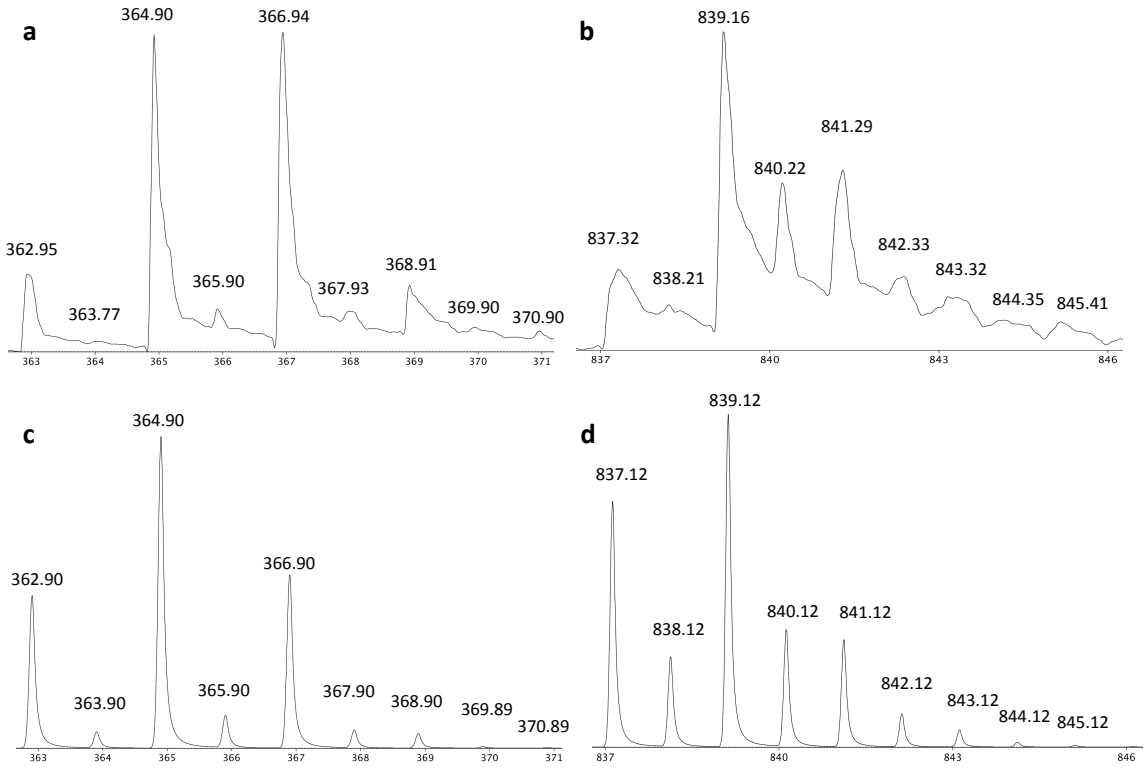

Figure 4.7. Isotopic envelopes from the reaction mixture of low temperature reaction of AlBr·THF and Li(StBu) at: (a) 362.95 m/z (b) 837.32 m/z (c) Calculated spectrum for anion $[Al(StBu)_2Br_2]^{1-}$(d) Calculated spectrum for anion $[Al_5(StBu)_7Br]^{1-}$ (y-axis = m/z).

As observed with the reactions involving pre-heated AlBr·THF solution, the full spectrum shows multiple isotopic envelopes indicating a wide variety of products from the reaction mixture.

The characterization provided by ESI-MS demonstrates that metathesis of AlX with thiolate ligands not only produces clusters, but promotes ligand decomposition yielding a large mixture of products.

4.3 Discussion

The isolation of $[Al(SPh)_4]^{1-}$ delineates similarity between AlBr-thiolate reactions and AlBr-phenylate reactions performed by Lauren Stevens in our lab who isolated $[Al(Ph)_4]^{1-}$. When $[Al(Ph)_4]^{1-}$ was isolated, it co-crystallized with an $[Li_4Al_5Ph_{12}]^{1-}$ complex, which is a mixed-valent aluminum product, leading us to believe that further pursuit of thiolate reactions may lead to the isolation of another mixed-valent aluminum product. The ESI-MS study of t-butyl thiolates supports this assertion through the identification of high nuclearity aluminum clusters in solution.

The formation of **4.1** along with the observed mirroring in the preheated AlBr reaction, and the formation of the Al_5 anion and Al^{3+} cation in the solution studies perfectly illustrates the nature of the aluminum (I) solutions. AlX solutions are metastable and are prone to undergo disproportionation reactions, yielding the thermodynamically more preferable aluminum metal and aluminum trihalides when at temperatures greater the -78 °C. Thus the goal is to utilize anionic ligands, such as the thiolates, to stabilize the Al–Al bonds that form during the disproportionation of the AlX solution and trap metalloid clusters before full disproportion occurs. There are two potential synthetic routes for ligand metathesis. Metathesis may occur prior to disproportionation of the AlX solution (Equation 4.2, R = anionic ligand).[5] It is also possible that the reaction is already proceeding via disproportionation and is then followed by ligand metathesis (Eq. 4.3).[5] Also these processes may be occurring concurrently. There is no evidence to support one mechanism over another but the continued isolation and characterization of Al^{3+} products with obvious mirroring supports the disproportionation of metastable aluminum.

$$AlX + LiR \xrightarrow{-LiX} AlR \xrightarrow{\Delta} Al + AlR_3 + Al_nR_m \quad (4.5)$$

$$AlX + LiR \xrightarrow{\Delta} Al + AlX_3 + Al_nX_m \xrightarrow{+LiR} Al_nR_m + AlR_3 + Al \quad (4.6)$$

At this time we cannot propose which mechanism is more likely than the other but the ESI-MS studies of the reactions with LiStBu thiolate with our low-valent AlX solutions does support that the ligand decomposition is occurring, and that heating the Al(I) precursor induces disproportionation of the starting material. The ESI-MS studies have yielded insight in to the importance of the initial reaction conditions, in particular temperature to the formation of unique Al-thiolate clusters in solution. The highest temperature reaction, which used pre-heated AlBr solution to 65°C, yielded the highest nuclearity Al-cluster in solution, $[Al_{17}Br(SC_4H_9)_{20}S_3]^{1-}$ (**4.2**). In the corresponding room temperature reaction, two envelopes were identified, corresponding to $[Al_{10}(SC_4H_9)_4S_9]^{1-}$ (**4.3**) and $[Al_{13}(SC_4H_9)_4BrS]^{1-}$ (**4.4**). It has been hypothesized that the structure of **4.4** could be analogous to the previously reported $[Ga_{13}R_6]^{1-}$ (R=Si^{t}Bu$_3$ and R =Si(SiMe$_3$)$_3$) clusters.[143] In the $Ga_{13}R_6^-$ cluster architectures there are seven naked gallium atoms arranged in a cubic fashion with one missing corner (Figure 8a). The three complete square faces of the cube are capped with GaR groups and the three incomplete square faces are shielded by a $(GaR)_3$ group whose center is directed towards the missing corner of the cube.[14,143]

Since $[Al_{13}(SC_4H_9)_4BrS]^{1-}$ is ligated to three different ligand, it may form similarly, but will have a lower symmetry than Ga_{13} (Figure 2.8a). We are proposing that in the metal core in $[Al_{13}(SC_4H_9)_4BrS]^1$ cluster will be a distorted type aluminum cube, as observed in the $[Ga_{13}R_6]^{1-}$. This assumption is based on the similarities observed in AlX and GaX cluster chemistry observed in Schnöckel type chemistry.[5]

At low temperature, the nuclearity, of Al atoms in the parent-ion peak decreases further. The ion observed at 837.12 m/z is attributed to a cluster with the formula of $[Al_5(S^tBu)_7Br]^{1-}$ (**4.5**) , the core of which can be compared to the core of $[Al_5Br_6THF_6]^+[Al_5Br_8THF_4]^-$ salt or comparable to another "Al_5" cluster prepared in our lab by Lauren Stevens: $[Li_4Al_5Ph_{12}]^{1-}$.[144] The formation of Al_5 shows congruency between reactions of monodentate thiolates the reaction with phenylates in our lab. This tetrahedral architecture appears to be stable for group 13 structures, and is also found in a series of gallium clusters of the structure type: $[Ga_5X_7L_5]$ (where X = Cl or Br, and L = Et_2O, THF and $NHEt_2$) $[Ga_5Cl_7(NEt_3)_4]$ (Figure 4.8).[145]

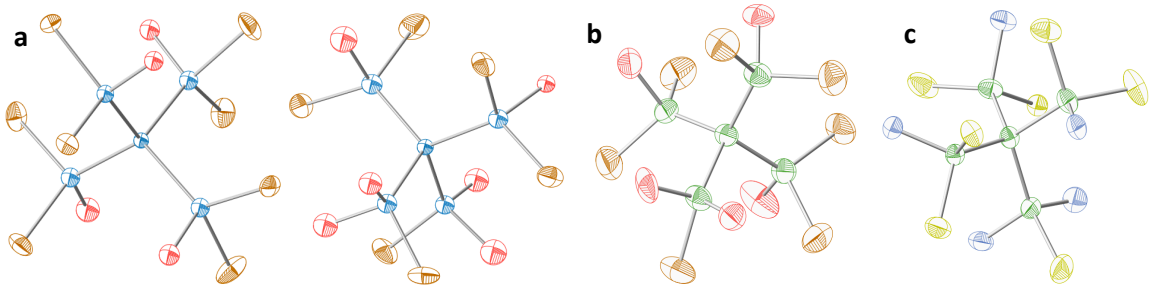

Figure 4.8 Examples of structurally characterized clusters of the E_5 tetrahedral structure type: (a) $[Al_5Br_6THF_6][Al_5Br_8THF_4]$ (b) $[Ga_5Br_7THF_5]$(c) $[Ga_5Cl_7(NHEt_2)_5]$ (Al=teal, Ga = green, N = blue, O= red, Cl = yellow, Br = brown, C and H omitted for clarity; thermal ellipsoids shown at 50% probability)

We hypothesize that the 837.12 m/z anion will contain and central Al atom tetrahedrally bound to four aluminum atoms. Three of the terminal aluminums will be ligated to two StBu groups, while the fourth bound to a single StBu group and a bromide ion (Figure 4.9).

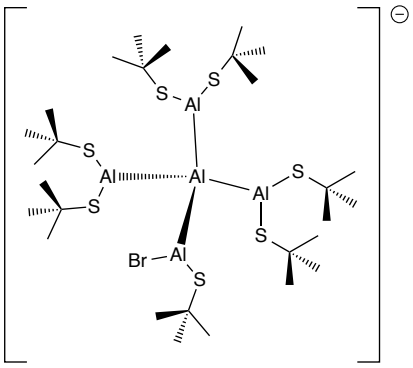

Figure 4.9. Proposed structure for ion observed at 837.32 m/z in negative mode via ESI-MS: $[Al_5Br(SC_4H_9)_7]^{1-}$.

It can be further postulated that the central aluminum will be more metallic in nature, Al^0, and the terminal aluminum groups would have an average oxidation state of 1.75^+ as is observed in other Al_5 and Ga_5 complexes. A possible formation mechanism can be proposed that is derived from the proposed formation mechanism of the salt $[Al_5Br_6THF_6][Al_5Br_8THF_4]$ (Scheme 4.1).

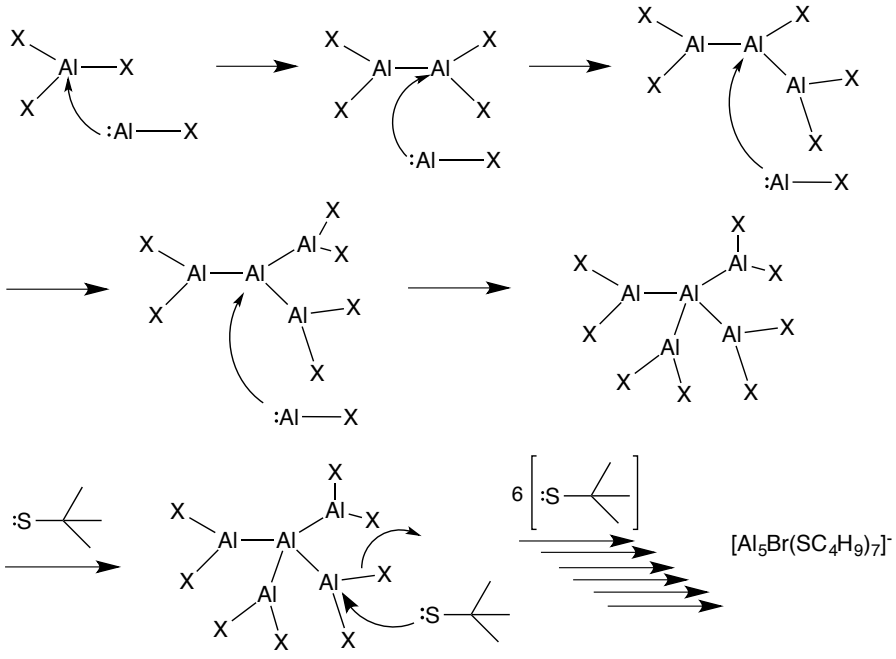

Scheme 4.1. Proposed mechanism for the formation of $[Al_5Br(SC_4H_9)_7]^{1-}$ as observed in ESI-MS based on previously reported formation mechanism for $[Al_5Br_6THF_6][Al_5Br_8THF_4]$.[144]

Starting from the trivalent AlX_3 (where X = Br), which is present in solution, the successive comproportionation products $[Al_2X_4]^{1-}$, $[Al_3X_5]^{1-}$, $[Al_4X_6]^{1-}$, $[Al_5X_6]^{1-}$ can be formed by successive insertion of: $Al^{I}X$. This oxidative insertion mechanism has been proposed for both Al and Ga chemistry.[144] In our proposed mechanism, the final product is produced by successive reactions (possibly SN2), substituting thiolate ligands for bromide ions, yielding **4.5** in solution. It is possible that this compound has not been isolated due the absence of a suitable cation in solution, and the sterics of the tert-butyl groups limiting the ability of donor solvents to ligate to the terminal atoms.

4.4 Conclusion

Monodentate thiolate ligands were chosen for low-valent aluminum reactions due to their soft nature, which should compliment the 'softer' quality of reduced oxidation state aluminum, assisting in the formation of novel aluminum clusters and, perhaps aluminum metalloid clusters. At this time, the Al^{3+} complex $Na[Al(SPh)_4]$ has been isolated, and many additional metalloid species including $[Al_{10}(SC_4H_9)_4S_9]^{1-}$, $[Al_{13}(SC_4H_9)_4BrS]^{1-}$, $[Al_{17}Br(SC_4H_9)_{20}S_3]^{1-}$, and$[Al_5Br(SC_4H_9)_7]^{1-}$ have been identified through ESI-MS analysis.

Therefore, these ligand types show great promise for the formation of metalloid clusters. When suitable reaction conditions are found, a plethora of clusters and complexes can be formed from reactions of thiolates with AlX solutions.

4.5 Experimental Details

General considerations: All reactions are performed under an argon atmosphere in a glovebox or under dinitrogen using standard Schlenk techniques. Toluene, diethyl ether,

and THF were purified by distillation from sodium benzophenone ketyl under a dinitrogen atmosphere. All purified solvents were stored in modified Schlenk vessels over 3 Å molecular sieves under dinitrogen atmosphere. Dr. Peter Zavalij at UMD performed X-ray crystallographic analysis.

$LiS(C_4H_9)$: HSC_4H_9 (3.607 g, 50 mmol) (purchased from Sigma Aldrich) was dispersed in THF and cooled to 0°C. Once cooled, nBuLi (45 mmol) was added drop-wise over a period of 15 minutes. The reaction was kept at 0°C for 3 hours then warmed to room temperature, and white powder precipitated out. The final product was washed with hexanes.

$Na[Al(C_6H_5)_4]$: $NaSC_6H_5$ (Sigma Aldrich) (0.5306, 4.01 mmol) was wetted with approximately 15 mL of Et_2O. Metastable AlCl•Et_2O (24 mL, 3.61 mmol) solution (3:1 toluene:Et_2O, 160 mL, Al:Cl ratio 1:1.13) was added to the $NaSC_6H_5$ at room temperature, the resultant dark brown solution was allowed to mix overnight. The next morning the Et_2O was removed from the reaction mixture in *vacuo*, and subsequently filtered to remove NaCl. It was then heated at 60°C. Twenty-four hours later a mirror formed on the walls of the Schlenk; it was heated for a total of 3 days until noticeable crystalline material had formed on the bottom of the Schlenk.

$[Al_{17}Br(StBu)_{10}S_3]^{1-}$: AlBr•THF (3:1 toluene:THF, 120 mL, Al:Br 1:1.03), 12.5 mL (4.5 mmol), was transferred to a prepared Schlenk and stored under nitrogen. The Schlenk was then transferred to an oven set at 60 °C. After 10 minutes there was visible mirroring on the walls of the flask, and it was removed from the oven and transferred to a Schlenk line. The pre-heated AlBr was added to room temperature Li*S*t*Bu (0.482 g, 4.96 mmol) and mixed overnight. After 15 hours, the solution was concentrated by $^1/_3$ and filtered to

remove precipitated LiBr. To prepare the sample for mass spec 0.5 mL of the reaction solution was added to approximately 20 mL of dry THF. Mass envelope attributed to $[Al_{17}Br(StBu)_{10}S_3]^{1-}$ is observed at 1525 m/z.

$[Al_{10}(StBu)_4S_5]^{1-}$ and $[Al_{13}(StBu)_4BrS]^{1-}$: AlBr•THF (3:1 toluene:THF, 120 mL, Al:Br 1:1.03) 12.5 mL (4.5 mmol) was added to lithium t-butyl thiolate (0.458 g, 4.7 mmol) at room temperature. The next morning the reaction mixture was filtered to remove LiBr salt and concentrated. Sample for the ESI mass spec was made by diluting 0.5 mL of reaction mixture in approximately 20 mL of dry THF. Mass envelopes attributed to $[Al_{10}(StBu)_4S_5]^{1-}$ and $[Al_{13}(StBu)_4BrS]^{1-}$are observed at 785.77 and 817.82 m/z respectively.

$[Al(StBu)_2Br_2]^{1-}$ and $[Al_5(StBu)_7Br]^{1-}$: AlBr•THF (3:1 toluene:THF, 160 mL, Al:Br 1:1.1) 12.5 mL (2.0 mmol) was added to a cooled solution of lithium t-butyl thiolate (0.2225 g, 2.5 mmol) at -78 °C. The next morning the reaction mixture was filtered to remove LiBr salt and concentrated. Sample for ESI-MS was made by diluting 0.5 mL of reaction mixture in approximately 20 mL of dry THF. Mass envelopes attributed to $[Al(StBu)_2Br_2]^{1-}$ and $[Al_5(StBu)_7Br]^{1-}$ are observed at 362.90 m/z and 837.12 m/z respectively.

Physical methods

X-ray crystallographic analysis: Was performed by Dr. Peter Zavalij at the University of Maryland. Graphite monochromated Mo Kα radiation (λ= 0.71073 Å) from a Mo-target rotating-anode X-ray source was used throughout. Data were corrected for absorption effects using the multi-scan methods, the structure was solved and refined using the Bruker transmission coefficients (based on crystal size) are 0.8720 and 0.9540.

Mass spectra: were collected on ACCUTOF ESI-MS at 3000 V in a THF solution utilizing our in-house introduction source (see-Appendices)

Chapter 5: Fabrication of unsupported and supported Al nanoparticles from AlX precursors

5.1 Introduction

Micron-sized aluminum particles have been utilized as an energetic material and as an additive in solid propellants since the turn of the 19th century.[146] Many studies have indicated that the addition of nanoparticles to fuels can increase the burning rate significantly. The premise governing this effect is that the rate of energy release is directly related to the transport of oxidizer to the particle, where smaller grains will lead to faster overall energy release. Therefore nano sized aluminum particles hold great promise for greater energy release. An important factor of these nanomaterials is that they are expected to have size dependent properties and have benefits over micron sized materials and the bulk material (Eq. 5.1 and 5.2).[44]

$$Al_{bulk} + O_2 \rightarrow Al_2O_{3(s)} \quad \Delta H = -1675 \ kJ/mol \tag{5.1}$$

$$Al_{atom} + O_2 \rightarrow Al_2O_{3(s)} \quad \Delta H = -2324 \ kJ/mol \tag{5.2}$$

Particles with sub-100 nm diameters are particularly attractive due to their high surface area to mass ratio. Several different methods have been employed over the years to synthesize Al-NPs of this size or smaller. These methods include: evaporation-condensation method,[40,41] laser ablation,[42,43] arc discharge,[44] mechanochemical synthesis (i.e. ball milling),[45] exploding wire experiments,[46,47] titanium-catalyzed decomposition of alanes[48] and liquid phase methods employing chemical or electrochemical reduction methods.[49-51]

An important aspect of nanoparticle chemistry is support material; the material on which the nanoparticles are supported on can enhance certain NPs properties.[147] A possible support material for NPs can be found in graphene and graphene oxide (GO). A

variety of defects and surface functional groups exist on both graphene sheets and graphene oxide, with more instances of occurrence in the latter (Figure 5.1).

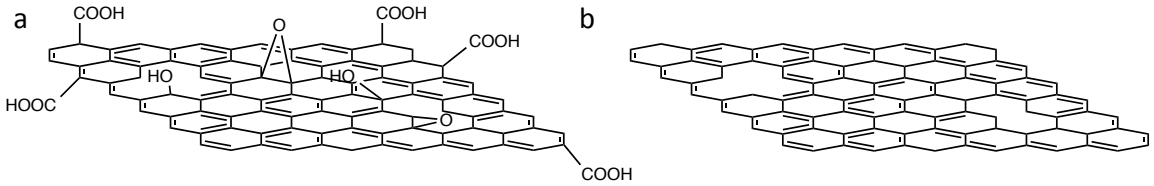

Figure 5.1. Visualization of (a) Graphene oxide (b) Graphene sheet with minor defects

These functional groups and structural defects act as nucleation points for templated growth of nanoparticles with specific sizes and topologies. Among the various successfully synthesized graphene derivatives, functionalized graphene sheets (FGS) formed via thermal exfoliation of graphene oxide (GO) have shown promise as a molecular template for a variety of applications.[148] Properties of graphene, including its high electrical conductivity, large surface area and mechanical strength have spurred research interest in this area. FGS also has a high concentration of defects that presumably serve a NP nucleation points and stabilization sites. Practical large-scale production method for pristine graphene has not yet been realized, but rGOs (slightly defected forms of graphene) are available on the small scale from solution routes. However graphene oxide (GO) can be produced on a large scale via Hummer's method and its variations, but unlike graphene, GO is electronically insulating and hydrophilic.[149]

Traditional nanoparticle (NP) synthesis typically uses materials such as surfactants to prevent oxidation and control the particle size. These methods also utilize energy intensive processes and/or strong reducing agents. Creation of a generic methodology where small, well-disperse nanoparticles are directly grown without the use of surfactants and/or reducing agents is, to our knowledge, an untapped area of aluminum

NP synthesis research. Utilizing graphene as a support for PtSn NPs by Eichhorn et al. has shown unique and enhanced properties when compared to unsupported PtSn NPs.[147] Further expansion of synthetic methods to another support, such as graphene oxide, has also been demonstrated in the literature. As mentioned above GO can be more readily synthesized with high yields, making it a cheaper and more available source. Using GO as a support for Ag and Au nanoparticles has been recently performed, and when these particle types are compared to their graphene supported congeners they show new properties.[150-152]

This chapter will describe the synthesis Al NP deposited on graphene and graphene oxide utilizing AlX solution as the aluminum source. First, a protocol was designed for the production of Al nanoparticles from AlX solutions. This method was then extended to routes for depositing Al on both FGS and GO, which will be delineated in this chapter. TEM/HRTEM, and XRD are used to characterize the composition and morphology of all samples from different synthetic routes.

5.2 Results

5.2.1 Synthesis and characterization of unsupported Al-NPs

Aluminum NPs were synthesized through reductive methods at low temperatures. Lithium aluminum hydride (LAH) was dispersed in toluene to form a slurry, which was subsequently cooled to -78°C. Once cooled, AlX was quickly added, and a black colloid was noticed immediately. The suspension mixed overnight while slowly warming to room temperature. The particles that formed were characterized via XRD-powder diffraction and TEM (Figure 5.2). Analysis of the aluminum nanoparticles via XRD showed the successful production of aluminum as indicated by the distinctive lattice

fringes with 1 1 1, 0 0 2, 0 2 2, 1 1 3, and 2 2 2 facets (38.5°, 44.7°, 65.1°, 78.2°, and 82.4° respectively); the most prominent peak corresponding to the 2.34 Å d-spacing is associated with the 111 lattice plane (Figure 5.2c). The signals in the pattern are much broader when compared to commercially bought Al NPs, which is an indication that they are smaller than commercially available particles. In support of this assessment Rietveld refinement on the patterns were performed.

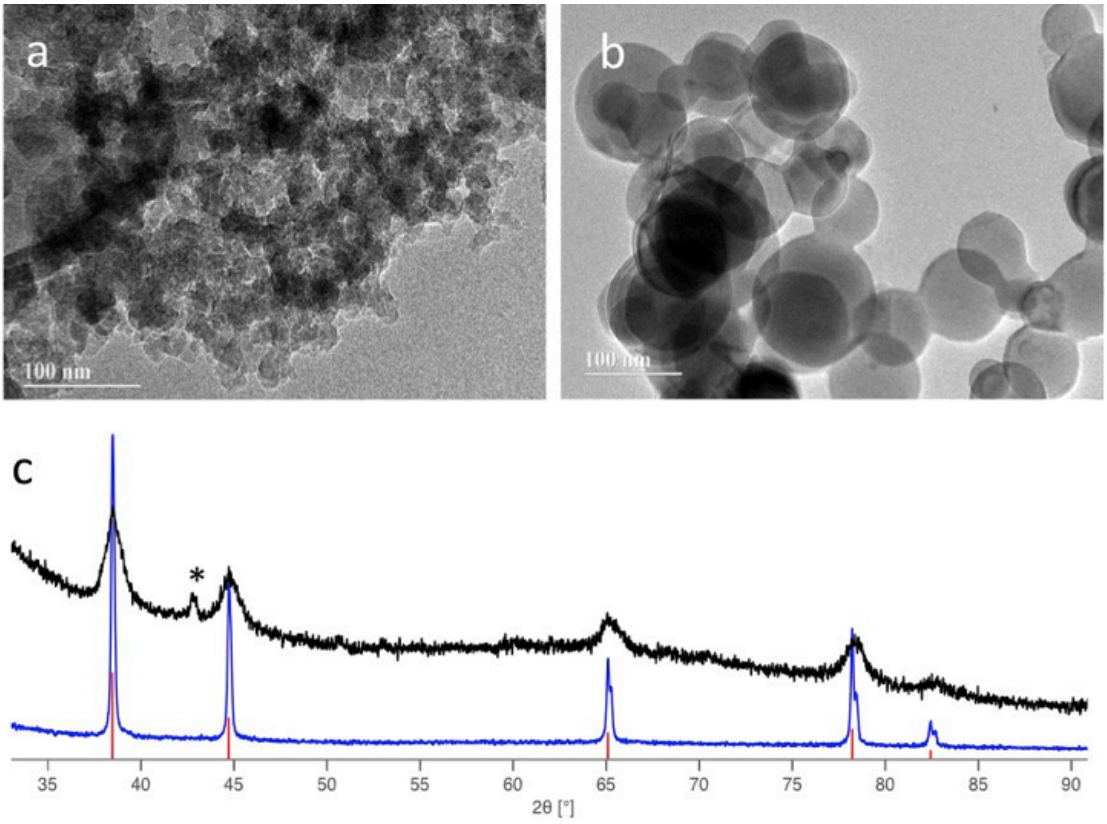

Figure 5.2. (a) TEM image of unsupported Al-NP produced from reduction of AlX solution of 21.7±2.1 nm average diameter aluminum nanoparticles (b) TEM image of commercial Al-NPs (c) XRD of commercial Al-NP (blue) unsupported Al NPs produced from reduction of AlX solutions (black), * denotes impurity. Pattern associated with Fm$\bar{3}$m aluminum (JCPDS 01-0713760, red)

These refinements demonstrated that on average, commercial nanoparticles are 76.3 ± 0.3 nm in size, while our NPs have an average diameter of 19.2 ± 0.1 nm. TEM images show a fair amount of agglomeration among the unsupported particles (Figure 5.2a), and

indicate an average size of an Al NP to be 21.7 ± 2.1 nanometers. Note that attempts of using a weaker reducing agent such as $NaBH_4$ with the AlX solutions did not result in aluminum nanoparticles, indicating that use of a strong reducing agent is necessary in these synthetic procedures.

5.2.2 Synthetic Routes and Characterization of FGS-Supported Aluminum Nanoparticles

All methods utilize vacuum dried FGS, and differ in the amount or order of reducing agent addition. When attempted with $NaBH_4$ or no reducing agent, aluminum nanoparticles were not synthesized. Note that size analyses of the NPs in this section are based off of TEM images, only providing insight into a small, representative sample size.

5.2.2.1 Aluminum NP deposition in presence of FGS and $LiAlH_4$ (Route 1)

Aluminum nanoparticles were deposited on FGS through the reduction of AlX (where X= Cl or Br) at -78°C in toluene (Eq. 5.3).

$$FGS + LAH \xrightarrow[toluene]{-78^{\circ}C,30\ \text{minutes}} LAH\ \ Slurry + AlX \longrightarrow Al\ \ on\ \ FGS + LiX + H_2 \quad (5.3)$$

The Al on graphene is washed with toluene until $LiAlH_4$ is no longer present in the wash, which is indicated by lack of H_2 evolution when water was added to the washes. The supported Al-NPs were characterized through XRD-powder diffraction and HR-TEM (Figure 5.3).

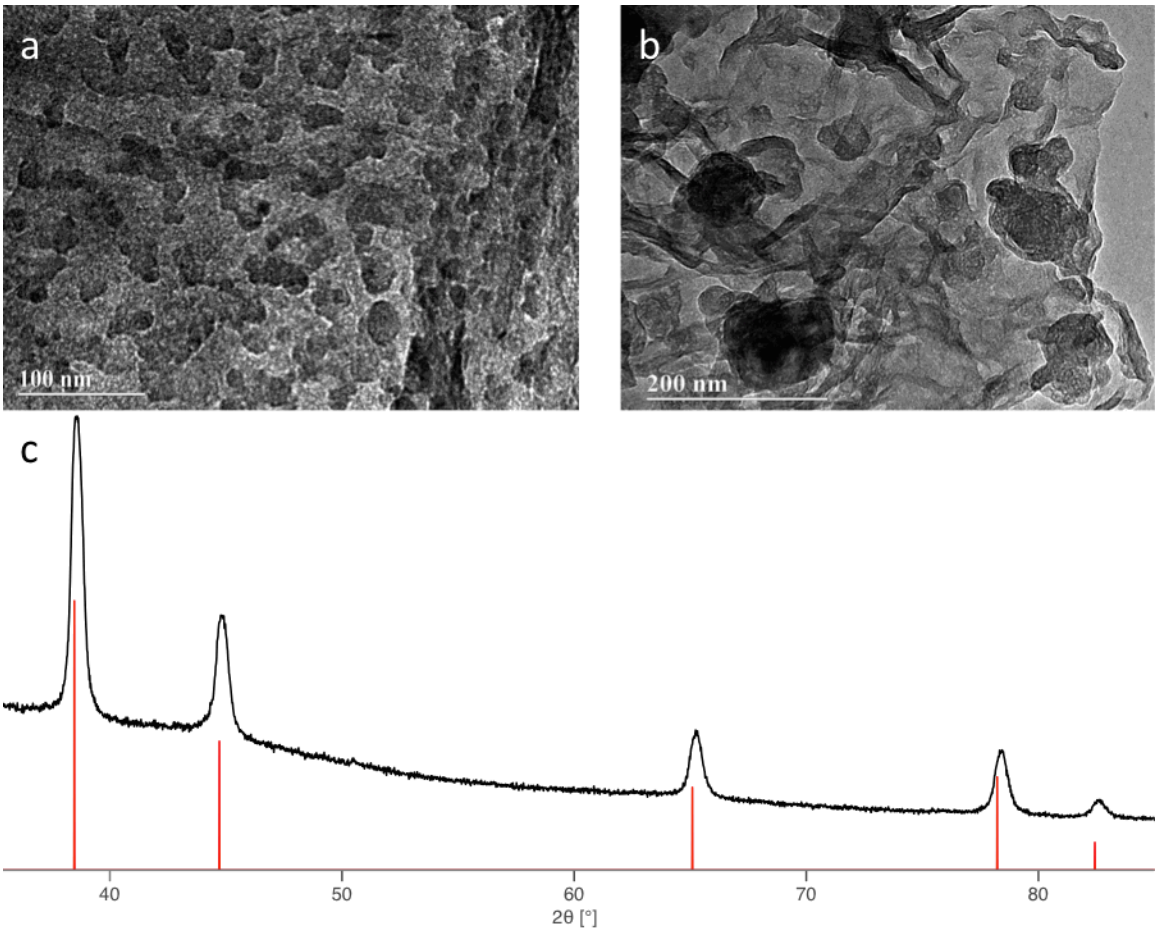

Figure 5.3. (a)TEM image of Al NP dispersed on FGS (b) agglomeration of Al NP on the sheets of FGS (c) X-ray diffraction pattern (1) experimental (black) database reference Al Fm$\bar{3}$m (red, JCPDS 01-071-3760)

The diffraction pattern indicates the formation of aluminum metal. A representative TEM of particles supported on FGS are shown Figure 5.3. Figure 5.3a shows deposition of Al NP on FGS where the average particle size is 20 ± 7.55 nm, while Figure 5.3b shows Al NPs on FGS sheets but also shows the presence of agglomeration on the sheets. Figure 5.4 shows the wide range of observed Al-NP sizes via TEM in this synthetic route. Loading on graphene is ≈ 65% aluminum by weight.

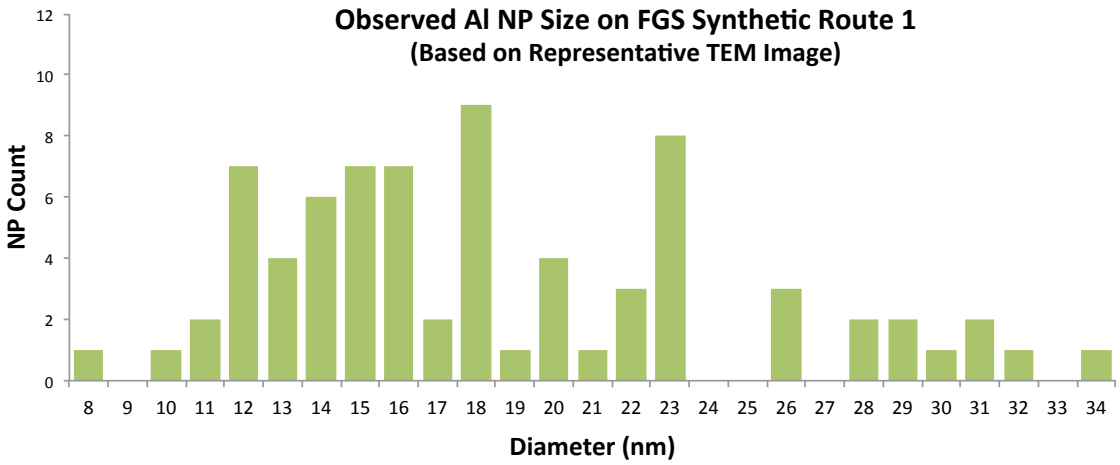

Figure 5.4. Al nanoparticle size distribution on FGS in presence of $LiAlH_4$ based on representative TEM images.

5.2.2.2 Post-Reduction of AlX in presence of FGS (Route 2)

FGS was pre-treated with an excess of $LiAlH_4$ and washed until $LiAlH_4$ is no longer present in the wash, as indicated by lack of H_2 evolution when water was added to the washes (Eq. 5.4). The 'pre-reduced' FGS is suspended in toluene and AlX is added at room temperature, once mirroring is observed, indicating the formation of Al(s), the reaction mixture is cooled to -78°C. Once cooled, a suspension of $LiAlH_4$ in toluene is added to the reaction mixture (Eq. 5.5).

$$FGS + LAH \xrightarrow{THF} \text{'}Pre-reduced\text{'}\ \ FGS \qquad (5.4)$$

$$\text{'}Pre-reduced\text{'}\ \ FGS + AlX \xrightarrow[Toluene,LAH]{25^{\circ}C \rightarrow -78^{\circ}C} Al\ on\ FGS + LiX + H_2 \qquad (5.5)$$

The sample is washed with toluene until the presence of LAH is no longer indicated. The supported Al-NPs are characterized through XRD-powder diffraction and HR-TEM.

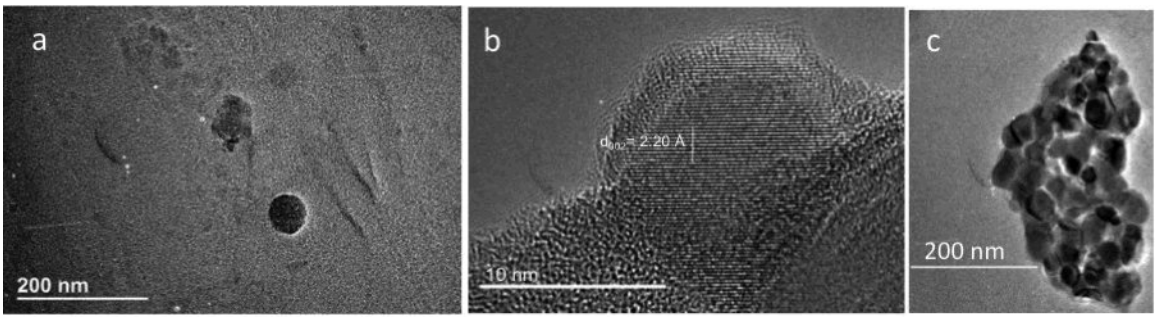

Figure 5.5. HRTEM of post-reduction of AlX in the presence of graphene (a) Poor deposition on a sheet of graphene (b) Representative Al NP from the synthetic route (c) Agglomeration of Al NP, not deposited on graphene

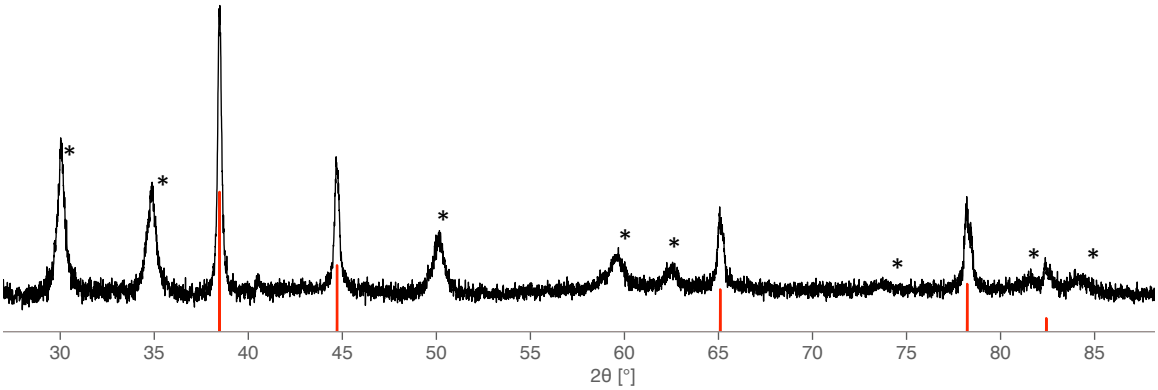

Figure 5.6. XRD pattern of synthetic route (2) Al NPs (black) database reference Al $Fm\overline{3}m$ (red, JCPDS 01-07103769) *Denotes reflections associated with LiCl.

The XRD pattern indicates the formation of aluminum metal, along with LiCl (Figure 5.6). A representative TEM image of an Al particle is shown in Figure 5.5b. Figure 5.5a shows that uniform dispersion of particles on the graphene did not occur, instead Al-NPs agglomerate off of the graphene Figure 5.5c.

5.2.2.3 Addition of AlX to pre-reduced FGS (Route 3)

FGS was pre-treated with LAH and washed until LAH is no longer present in the wash (Eq. 5.6). The 'pre-reduced' FGS is suspended in toluene and cooled to -78°C, once cooled AlX is then added (Eq. 5.7).

$$FGS + LAH \xrightarrow{THF} \text{'Pre}-reduced\text{'}\ \ FGS \qquad (5.6)$$

$$\text{'Pre}-reduced\text{'}\ \ FGS + AlX \xrightarrow[Toluene]{-78^{\circ}C} Al\ \ on\ \ FGS + LiX + H_2 \qquad (5.7)$$

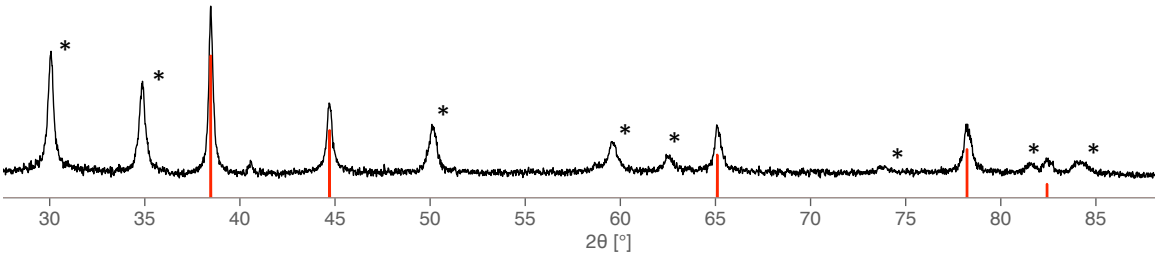

Figure 5.7 XRD pattern of synthetic route (3) Al nanoparticles (black) database reference Al Fm$\bar{3}$m (red, JCPDS 01-07103769) *Denotes reflections associated with LiCl.

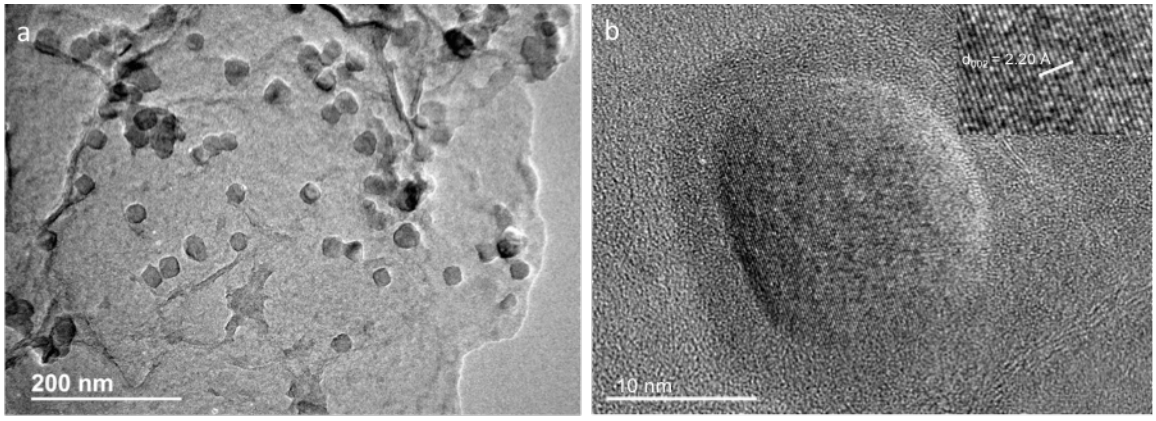

Figure 5.8. (a) HR-TEM of faceted Al NP deposited on a sheet of 'pre-reduced' FGS (b) HR-TEM of representative Al particle on the sheet of FGS.

The Al on graphene is washed with toluene until color is no longer evident in the supernatant. The supported Al-NPs are characterized through XRD-powder diffraction and TEM. The diffraction pattern indicates the formation of aluminum metal and LiCl (Figure 5.7). A representative TEM image of particles supported on functionalized graphene is shown Figure 5.8a and a representative particle is shown in Figure 5.8b. Exposure to air prior to TEM analysis results in development of a uniform oxide shell approximately 3 nm thick is illustrated in Figure 5.8b. The Al NPs fabricated via this synthetic route are highly crystalline, with no evidence of amorphous domains and few particles with twinning or other grain boundaries. Unlike the other synthetic routes the

particles deposited are distinct and widespread, and agglomeration is not observed. The size of the nanoparticles formed is less varied than in the other routes (Figure 5.9), and the average particle size is calculated to be 23.8 ± 3.30 nm.

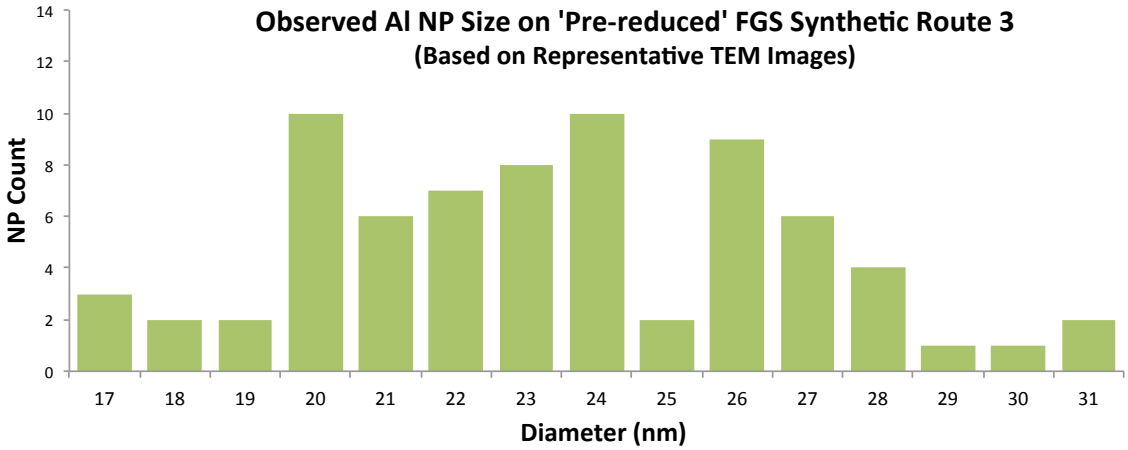

Figure 5.9. Nanoparticle size distribution of Al NP on FGS, based on representative TEM image.

5.2.2.4 Addition of AlX to Graphene Oxide (GO)

GO (C:O = 70:30), prepared via the Hummer's method in our lab by Kim Hyunh, was vacuum dried suspended in THF and cooled to -78 °C. LAH suspended in THF is added to the cooled flask, and the slurry mixes for 30 minutes. After 30 minutes AlX is added and the work-up is the same as delineated in synthesis route (1) (Eq. 5.8).

$$GO + LAH \xrightarrow[THF]{-78^{\circ}C,\ 30\ minutes} LAH\ \ Slurry + AlX \longrightarrow Al\ \ on\ \ GO + LiX + H_2 \quad (5.8)$$

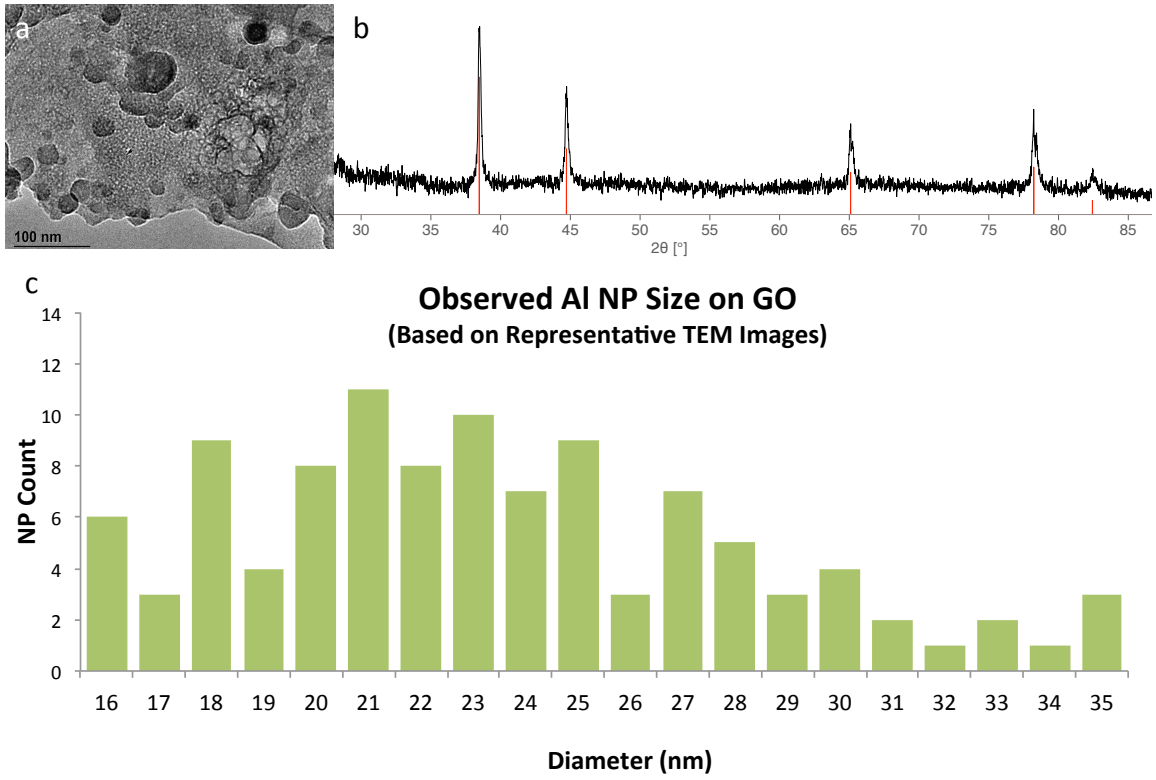

Figure 5.10. (a) Al NPs supported on GO (b) XRD pattern showing formation of Al NPs (black) database reference Al Fm$\bar{3}$m (red, JCPDS 01-07103769) Broad peak centered at 22.4° indicative of GO (c) Nanoparticle size distribution of Al NP on GO

The supported Al-NPs are characterized through XRD-powder diffraction and HR-TEM (Figure 5.10). XRD indicates that Al and no LiCl is present (Figure 5.10b). These analyses were supported through HR-TEM imaging and EDX analysis, which shows Al deposited among GO flakes and no indication of Cl (Figure 5.11).

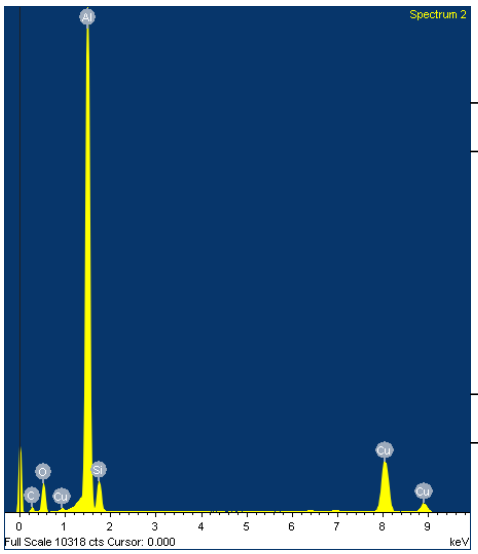

Element	Weight %	Atomic %
C	3.30	7.47
O	7.40	12.59
Al	67.66	68.25
Si	4.47	4.33
Cu	17.18	7.36
Totals	100	100

Figure 5.11. EDS of Al on GO: The presence of Cl is not indicated, and the overwhelming product is Al

5.3 Discussion

All methods described resulted in production of aluminum nanoparticles, as indicated by XRD and HR-TEM studies. For this study the material of greatest interest are supported Al NPs. In particular synthesis route **2**, which shows growth of Al nanoparticles on the graphene monolayers without direct contact of a reducing agent (Figure 5.8). The expected Al and LiCl lattice spacings match all reflections in the diffraction pattern, and studying the lattice fringes via TEM along with EDS analysis support that aluminum metal is the major product isolated. Synthetic route **2**, involves the pre-reduction of FGS, which de-acidifies and activates the surface. The subsequent addition of AlX at -78 °C without further addition of reducing agent deposits faceted aluminum on graphene with little agglomeration, and has the smallest spread of nanoparticle sizes. When a weaker reducing agent, $NaBH_4$, is substituted in for LAH, the patterns do not demonstrate the formation of aluminum metal. This result indicates that

the presence of LAH is important in the reduction of AlX, and that a stronger reducing agent is necessary for full reduction to Al-metal to occur.

AlX solution provides a unique and successful starting material for nanoparticle production, and products yielded from AlX have shown structural resemblances to Al metal. A reason for this success could be attributed to the close relationship the AlX has to bulk aluminum metal. As previously mentioned reactions of Li(HMDS) with AlX precursors yield a series of Al clusters: $[Al_7R_6]^-$, $[Al_{12}R_8]^-$, $[Al_{14}R_6X_6]^-$, $[Al_{69}R_{18}]^{3-}$, and $[Al_{77}R_{20}]^{2-}$ (where R = HMDS).[20,23,24,31,33,34] These clusters have been described as molecular nanostructured elemental modifications of fcc Al, and is evident when viewing the topological relationship of both $[Al_7R_6]^-$ and $[Al_{12}R_8]^-$ to the bulk phase (Figure 5.12).[112] The relationship between the 'nano-wheel' structure of $[Al_{14}R_6X_6]^-$ relationship and the solid state of aluminum metal can be demonstrate through 30° rotation of the 'top ring' in relation to the 'bottom ring' (Figure 5.12).

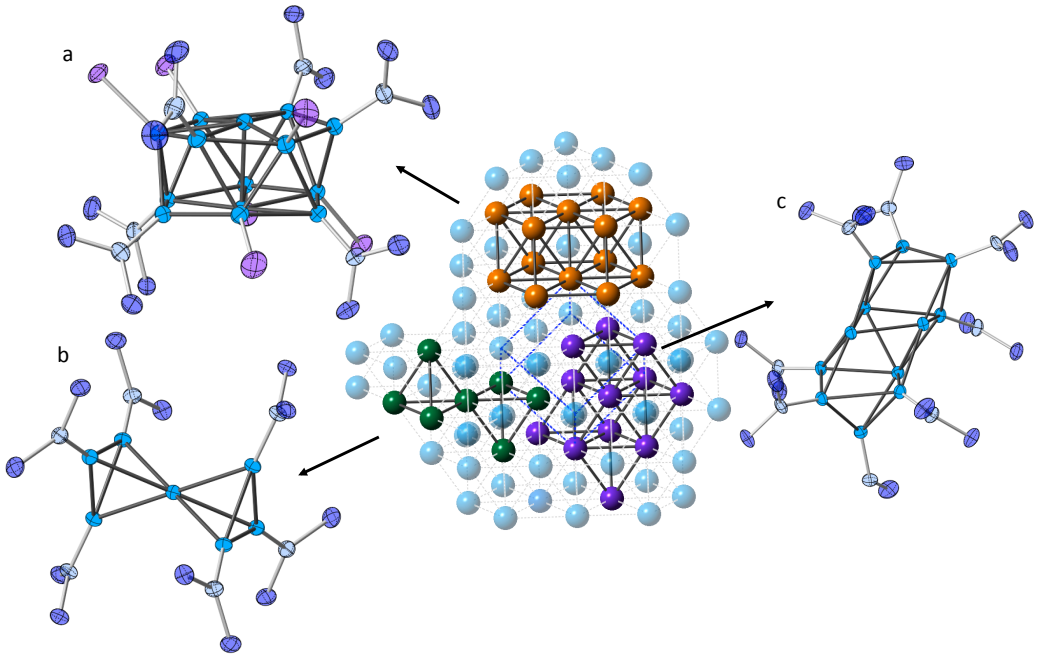

Figure 5.12 Relationship of known metalloid clusters and solid-state structure of elemental aluminum (fcc): a) $[Al_{14}R_6I_6]^-$ b) $[Al_{12}R_6]^-$ c) $[Al_{12}R_6]^-$. R = $N(SiMe_3)_2$ (adapted from [**112**])

The two larger metalloid clusters $[Al_{69}R_{18}]^{3-}$, and $[Al_{77}R_{20}]^{2-}$ demonstrate the interface between molecular and nano-scale chemistry for aluminum, and the Al-atoms favor an arrangement in a closest packing fashion as is observed in aluminum metal (refer to section 1.5.1).[14] This close relationship between AlX and Al metal may be why it is good starting material for the production of Al NPs.

Mechanism of Al-nanoparticle formation

Calculations performed by Hooper *et al*. indicate that AlCl interacts weakly with graphene in the absence of vacancies.[53] However, AlCl interacts very strongly with a single vacancy (SV) in graphene, preferring an orientation-aligned perpendicular to the sheet with Al atom directly above the defect at a distance of 1.92 Å from the three carbons adjacent to the vacancy.[53] These calculations support the notion that the aluminum monohalide is largely free to diffuse across the surface of a pure graphene

sheet, but will chemisorb very strongly at a single vacancy and provide a nucleation point for further oxidative insertion. This oxidative binding introduces an aluminum (III) chloride center capable of undergoing oxidative insertion with additional AlCl monomers in solution. This is in agreement with the mechanism proposed by Schnöckel and coworkers for metalloid cluster growth (Scheme 5.1).[153]

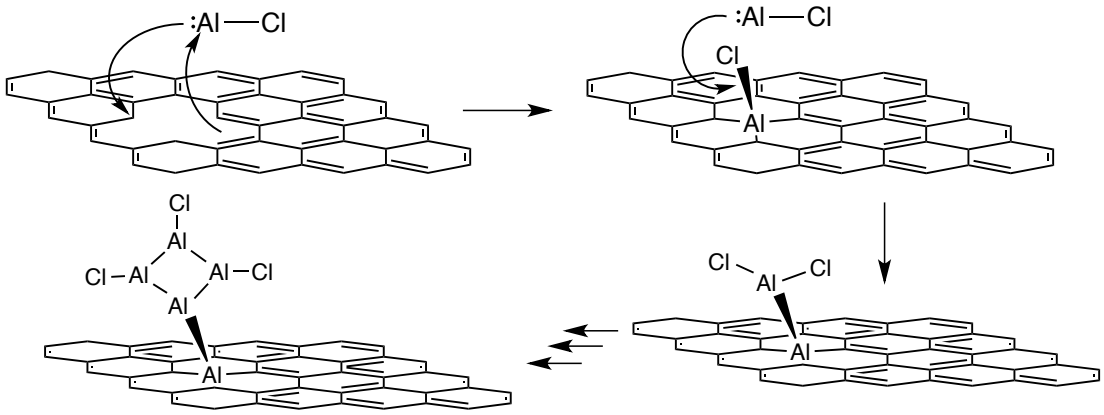

Scheme 5.1. Oxidative insertion of AlCl into graphene defect followed by particle growth

The closest to mimicking this postulation experimentally is the pre-reduction of graphene that subsequently reacted with our aluminum source AlX described in synthetic route **2**. But by introducing the LAH to the system in order to pre-reduce/clean the graphene can lead to the 'activation' of the acidic sites. This activation could be leading to the formation of alkoxide groups on the sheets of graphene, which changes the manner in which the Al NPs could be forming as depicted in Scheme 5.2. At graphene alkoxide sites, electrophilic aluminum monochloride may undergo salt metathesis reactions, similar to the synthetic route for metalloid cluster formation, forming graphene –

supported aluminum (I) alkoxide and lithium chloride (Scheme 5.2).

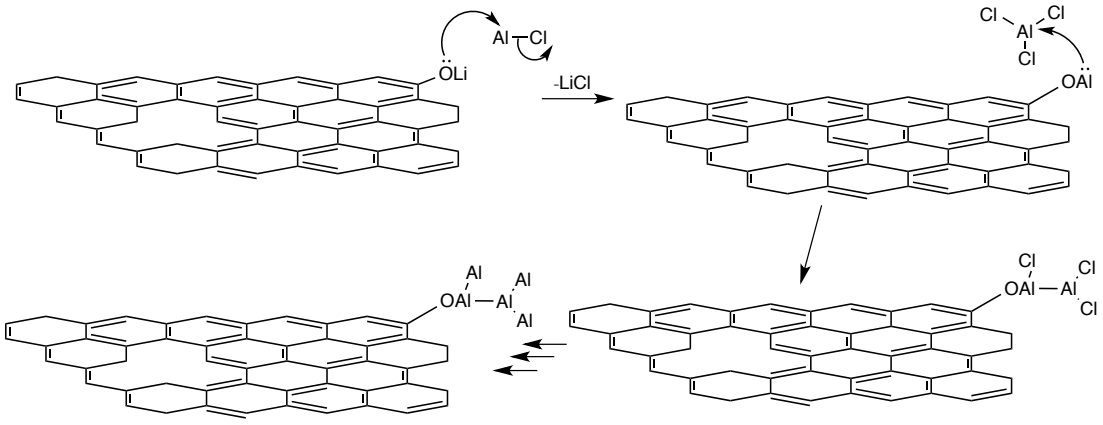

Scheme 5.2. Salt metathesis reaction involves the alkoxide group, present from the pre-reduction of the graphene, followed by Al-NP growth.

This graphene-bound aluminum atom is capable of nanoparticle growth through oxidative insertion reactions into $AlCl_3$ bonds in a method similar to that described in Scheme 5.2. In this case, insertion into the minor $AlCl_3$ byproduct is present after AlCl generation, which leads to particle growth. Either one or both of these mechanisms could be occurring and are consistent with the TEM and XRD data described in the results section. At this time more studies are necessary to parse what is happening mechanistically.

5.4 Conclusion

AlX has proven to being adept at producing metalloid clusters whose structures strongly correlate to solid-state aluminum metal, making it a logical choice as a precursor for nanoparticle production. The synthesis of Al NPs from AlX solutions are able to occur at low temperatures and utilizing limited amounts of reducing agent. The nanoparticles produced from AlX are readily supported on both FGS and GO. Unsupported NPs produced with these solutions are almost uniform in size (average size

19.3 nm), and when compared to commercial aluminum are smaller and have a less size dispersity. A synthetic route has been developed for the production of well-dispersed, faceted Al NPs. Also synthetic route for the deposition of Al NPs on GO is described. This material is of interest because it contains both reduced Al and the oxidant in one product, but more experimental work still needs to be performed.

Using the AlX solutions provides two potential mechanistic routes for deposition on graphene. The growth of Al NPs could be due to oxidative insertion, as proposed by Schnöckel *et al.*, or a result of a salt metathesis reaction due to the use of $LiAlH_4$ as a reducing agent. Now that these NPs can be made on supports of FGS and GO studies on energetic output are of high interest and should be compared to unsupported Al NPs.

5.5 Experimental Considerations

General considerations

All reactions were performed in an inert atmosphere using standard Schlenk and dry box techniques. Toluene, diethyl ether, and tetrahydrofuran were purified by distillation from sodium benzophenone ketyl under a dinitrogen atmosphere. All purified solvents were stored in modified Schlenk vessels over 3 Å molecular sieves under a dinitrogen atmosphere. AlX•n (where X = Cl or Br, and n = donor solvent) was prepared according to a modified literature procedure).

FGS was obtained through collaboration with Professor M. Zachariah's lab, and GO was produced in house via the Hummer's method by Kim Huynh.

(Route 1) In the presence of $LiAlH_4$

In a typical synthesis vacuum dried FGS (≈15 mg) and an excess of $LiAlH_4$ (176.4 mg, 4.65 mmol) were combined and suspended in 25 mL of toluene at room temperature.

After 30 minutes the mixture was cooled down to -78°C. Cold AlCl•Et_2O (6.7 mL of a 149 mM [Al] solution, 1 mmol AlCl, 27 mg Al) was then added to the graphene/$LiAlH_4$ slurry via syringe. The reaction mixture was stirred for 16 hours, while slowly warming up to room temperature, and then allowed to settle. The colorless supernatant was removed via cannula and the remaining black solid washed with alternating washes of toluene and Et_2O until the washes no longer exhibited H_2 evolution upon the addition of water. The black powder was dried in vacuo, yielding FGS-supported Al NPs.

(Route 2) Addition of Reducing agent after Al introduction

FGS is pre-reduced: Vacuum dried FGS (≈15 mg) and an excess of $LiAlH_4$ (148.0 mg, 3.90 mmol) were combined and subsequently suspended in 25 mL of THF at room temperature. This treatment was performed to clear any impurities and activate the surface of the graphene prior to the addition of AlX. This gray-black suspension of FGS and $LiAlH_4$ was stirred at room temperature for 60 minutes and then allowed to settle. The mixture was decanted via cannula and the solids were alternately washes with Et_2O (2 × 25 mL) and toluene (2 × 25 mL) until the washes no longer demonstrated hydrogen evolution upon the addition of water. After the final wash the resultant black solid was dried in vacuo, then subsequently suspended in toluene (25 mL). Cold AlCl•Et_2O (6.7 mL of a 149 mM [Al] solution, 1 mmol AlCl, 27 mg Al) was then added to the graphene suspension at room temperature. The reaction flask is then cooled down to -78°C and a slurry of $LiAlH_4$ (148.1 mg, 3.90 mmol) suspended in toluene was added. The reaction mixture was stirred for 16 hours while slowly warming up to room temperature, and allowed to settle. The colorless supernatant was removed via cannula and the remaining black solid washed with alternating washes of toluene and Et_2O until the washes no

longer exhibited H_2 evolution upon the addition of water. The black powder was dried in vacuo, yielding few FGS-supported Al NPs, and mostly unsupported Al NPs.

(Route 3)'Pre-reduced' graphene

In a typical synthesis vacuum dried FGS (≈15 mg) and an excess of $LiAlH_4$ (148.0 mg, 3.90 mmol) were combined and subsequently suspended in 25 mL of THF at room temperature. This treatment was performed to clear any impurities and activate the surface of the graphene prior to the addition of AlX. This gray-black suspension of FGS and $LiAlH_4$ was stirred at room temperature for 60 minutes and then allowed to settle. The mixture was decanted via cannula and the solids were alternately washes with Et_2O (2 × 25 mL) and toluene (2 × 25 mL) until the washes no longer demonstrated hydrogen evolution upon the addition of water. After the final wash the resultant black solid was dried in vacuo, wetted with toluene (25 mL) and cooled to -78°C. Cold $AlCl•Et_2O$ (6.7 mL of a 149 mM [Al] solution, 1 mmol AlCl, 27 mg Al) was then added to the graphene slurry via syringe. The reaction mixture was stirred for 16 h, while slowly warming up to room temperature, and then allowed to settle. The red-brown supernatant was removed via cannula and the remaining black solid washed with toluene until the supernatant was clear and colorless (3 × 25 mL), then washed with diethyl ether (2 × 25 mL). The black powder was then dried in vacuo, yielding FGS-supported Al NPs.

(4) GO supported Al nanoparticles

In a typical synthesis vacuum dried GO (≈30 mg) was suspended in 25 mL of toluene at room temperature, and cooled to -78°C and an excess of $LiAlH_4$ (148.0 mg, 3.90 mmol) was added. The slurry was stirred for 1 hour. Cold $AlCl•Et_2O$ (6.7 mL of a 149 mM [Al] solution, 1 mmol AlCl, 27 mg Al) was then added the graphene oxide/$LiAlH_4$ suspension

via syringe. The reaction mixture was stirred for 16 hours, while slowly warming up to room temperature, and then allowed to settle. The clear supernatant was removed via cannula and the remaining black solid washed with toluene until the supernatant was clear and colorless (3 × 25 mL), then washed with diethyl ether (2 × 25 mL). The black powder was then dried in vacuo, yielding FGS-supported Al NPs.

Physical Methods

Transmission Electron Microscopy (TEM): TEM images were obtained on a JHM 2100F Field Emission TEM operating at 200 KV. The supported NP powders were oxidized in air for ≈20 minutes then dispersed in toluene. A 6 μL aliquot of resulting dispersion was dropcast on the TEM grids. The TEM grids used were lacy carbon-coated Cu grids (Cu-400LC, Pacific Grid Tech).

Powder X-Ray diffraction (XRD): XRD patterns were obtained on a Bruker D8 advance diffractometer equipped with Lynxtec detector using a monochromatic Cu Kα radiation source biased at 40 kV and 40 mA. The XRD patterns were background corrected.

Powder X-ray diffraction (XRD): Patterns of samples were obtained on a Bruker C2 Discover diffractometer equipped with a VÅNTEX-500 detector using a monochromatic Cu kα radiation source biased at 40 kV and 40 mA. The XRD patterns were background corrected.

Chapter 6: $[AlBrNEt_3]_4$ as a dopant in hydrocarbon fuel

6.1 Introduction

Aluminum metal has a long history of being used as an energetic material due to its immense enthalpy of combustion.[154] Its energy content is significantly greater than that of traditional C, H, O, and N materials in terms of both mass and volume considerations.[146] However, the use of aluminum metal as a propellant or explosive has been hindered due to slow initiation kinetics associated with presences of an oxide barrier on the metal surface. Attempts to prevent oxide barrier layer formation through passivation and nanoparticle synthesis have been met with limited success. It has been shown that nanoparticles (with diameters between 1–100 nm) demonstrate shorter ignition delay and higher burning rates than larger particles due to their increasing surface to volume ratios as particle size decreases.[155] Novel methods are required to overcome the kinetic problems associated with the combustion of Al-metal. It has been postulated that use of the unique low oxidation state Al products produced from AlX precursors, would be an invaluable additive to fuels to increase energetic output. Theoretical studies performed by Hooper *et al.* have demonstrated that in low-valent aluminum clusters preferential oxidation occurs at the aluminum centers with minimal initial oxidation of ligands occurring.[55] Studies involving low-valent aluminum products in terms as energetics additives have been limited due to lack of access to low-valent aluminum products , and air/water sensitivity.

In the literature there has a been a great amount of focus and study centered upon 'nanofuels' since the mid 1990's.[156] For the purposes of our study, nanofuels are defined as a fuel that contains nanostructures as a means to increase the energy density or

moderate the burning characteristics of traditional liquid fuels. Early research in this area is heavily marked by studies of direct use of nanoparticles as diesel fuel additives of compression ignition engines. These additives ranging from Al[157-159], Al_2O_3[158], Fe[159], B[159], CeO_2[160], Fe_3O_4[161], and Carbon Nanotubes (CNT)[162] show a decrease in NOx, hydrocarbon, and/or CO emissions.

The exact effect of the additive depends on the relative strength of competing mechanisms, which are highly dependent on ambient temperature, particle loading chemical stabilizations, and physical characteristics of the pure solvent. A variety of interacting processes and mechanisms have been proposed and supported by empirical observation in droplet evaporation and combustion studies.[163-172] For example volatility and viscosity affect the relative timescales of solvent evaporation versus particle transport and aggregation in the fluid. An energetic, soluble alternative to nanoparticle additives has the potential to overcome these aggregation challenges while conserving the benefits of high-energy-density additives, thereby promoting relative dominance of the combustion-promoting mechanisms.

The study described herein involves the determination of the effects that a molecular tetrameric aluminum additive, $[AlBrNEt_3]_4$, produced from an aluminum monohalide (AlBr) solution, has on the burning rate of a hydrocarbon fuel. Guereri *et al.* performed analysis of the fuel in-house via a drop-tower to estimate burning rate constants. Further characterization on the tetramer includes mass spectrometry in order to probe reaction mechanisms of the burning of the fuels.

6.2 Results

6.2.1 Synthesis of [AlBrNEt$_3$]$_4$

The hydrocarbon soluble Al(I) tetrameric cluster, [AlBrNEt$_3$]$_4$, (Figure X) is synthesized from the AlBr•NEt$_3$ starting material. This tetramer has been previously isolated by Schnöckel et al.[173] This cluster is a ligand–stabilized component of the AlBr•NEt$_3$ precursor solution and contains aluminum in the 1+ oxidation state with covalent Al–Al bonds (average bond length 2.41 Å) (Figure 6.1). The structure consists of a square Al$_4$ ring with one halide and one donor molecule bound to each aluminum atom and exhibits virtual T$_d$ symmetry, and the cluster [AlBrNEt$_3$]$_4$ exhibit D$_{2h}$ symmetry. The halide and donor molecules alternate above and below the ring plane (Figure 6.1).

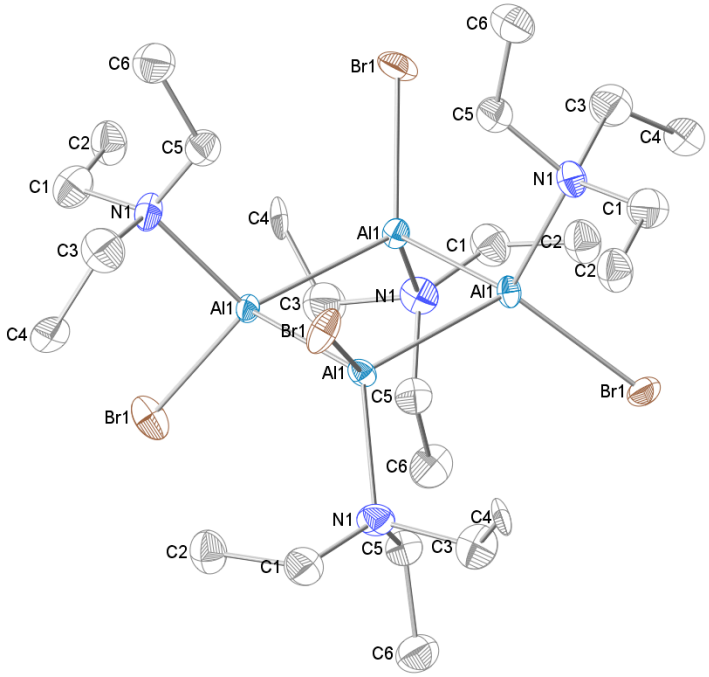

Figure 6.1. Crystal structure of [AlBrNEt$_3$]$_4$ thermal ellipsoids reported thermal ellipsoids drawn at the 50% probability level, hydrogen atoms omitted for clarity.

The tetramer is isolated from solution as tetragonal yellow crystals, $P\bar{4}2_1c$, and exhibits good solubility in the nonpolar organic solvents benzene and toluene and is readily characterized via ^1H NMR.

6.2.2 Preparation of $[AlBrNEt_3]_4$ doped hydrocarbon fuel

To maximize the concentration of aluminum in solution for energetic studies, the donor solvent Et_2O was added to the toluene maximize the solubility of the cluster in a tol:Et_2O (4:1) co-solvent mixture for maximum concentration. This mixture allows for more concentrated samples containing ≈40 mmol of aluminum, compared to ≈24 mmol of aluminum in pure toluene solutions. Due to the low oxidation state of the aluminum (I) tetramer and lack of an oxide passivation layer normally found on bulk aluminum metal, the solution, is extremely air and moisture sensitive. Once $[AlBrNEt_3]_4$ is exposed to air, rapid oxidation occurs causing precipitation of aluminum oxide and hydrolysis products, which necessitates the use of Schlenk techniques and gas tight syringes for handling of the fuel.

6.2.3 Drop Tower Burning rate Analysis

Burning rate analyses were performed a tower from Yetter *et al.* adapted by Guerieri. For in depth description of the droplet tower and image collection parameters, see Guerieri *et al.* in reference [174]. A reasonable set-up to determine the burning rate of the nanofuel was developed. The need for an adapted method was compounded by the air sensitivity of the fuel, and the behavior of the droplet once burned in the tower. Typically, in liquid droplet combustion theory sates that, assuming the droplet is fully liquid, and therefore the volume of the droplet is directly coupled with its mass, the rate

of decrease in droplet volume is linearly proportional to the diameter of the droplet.[175] This relationship is relayed through the following equation (Eq. 6.1):

$$\frac{D(t)^2}{D_0^2} = 1 - K\frac{t}{D_0^2} \tag{6.1}$$

This equation is commonly referred to as the D^2 law is used to determine the burning rate of the liquids characterized in this study; the burning rate constant (K), expressed in s^{1-}, increases proportionally for droplets that burn faster. Experimentally determined droplet diameters and burn times are fit to the D^2 law by plotting the square of the diameter (normalized to the initial diameter) versus time and assessing the slope of a linear best fit, and from that trend an estimated burning rate constant can be determined. Another way to solve for the K, without the constraint that the droplet be entirely liquid is to use the equation (Eq. 6.2):

$$K = \frac{1 - \left(\frac{D^2_{Extinction}}{D_0^2} \right)}{\left(\frac{t_{Extinction}}{D_0^2} \right)} \tag{6.2}$$

The data for this equation are collected by capturing the entire combustion trajectory instead of relying on solely the diameter of the in flight droplet. The basic set-up can be described as follows: A 20" tall × 3 inches squared aluminum tower has three sides consisting of removable transparent windows. Oxygen gas enters the tower at the top, and a nitrogen flow is introduced through the droplet delivery nozzle. In order to avoid over-pressure of the system, the gases escape via exhaust at the open bottom of the tower. Droplet generation is achieved with a capillary needle assembly nested in a glass sheath tube supplied with nitrogen gas flow. Below the droplet nozzle, methane gas is

introduced and ignited to create two stable diffusion flames for the droplet to pass through.

In the experiment, a measurement of the initial droplet size is required to normalize the data, and account for fluctuations in droplet size. For purposes of these analyses the initial droplet size is defined as the average equivalent spherical diameter of the droplet in three image frames nearest the flames.

With these experimental parameters and analyses in mind, data were collected for the burning droplet of $[AlBrNEt_3]_4$ dissolved in tol:Et_2O. For comparison and control purposes, data were also collected for a dispersion of aluminum nanoparticles (nAl) in tol:Et_2O (4:1), a solution of tol:Et_2O (4:1) with a molar equivalent of NEt_3 (comparable to the amount present in dissolved tetramer), and blank solvent mixture of tol:Et_2O (4:1) were analyzed. Data for the pure solvent and particulate nAl additive were analyzed with the classical model. The fuel with the $[AlBrNEt_3]_4$ dissolved in it exhibits disruptive events characterized by cyclical droplet inflations and eruptions or "micro-explosions" this deviates the droplet diameter evolutions from the classical D^2 law. The 9.7 mM tetramer sample showed up to ten micro-explosion events, most commonly occurring in the later stages of droplet combustion (Figure 6.2).

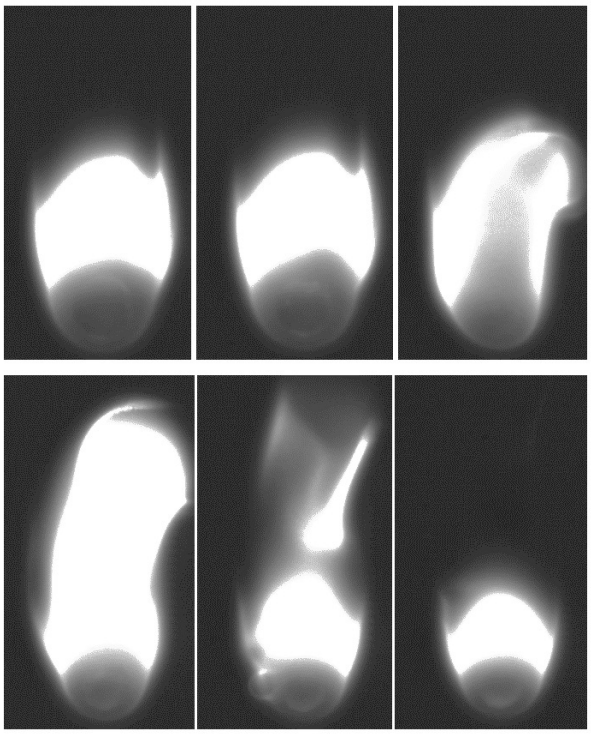

Figure 6.2. Gas generation in $[AlBrNEt_3]_4$ droplet. Top Row: Inflated droplet releasing gas. Bottom Row: Deflated droplet after gas release with flame perturbation. Image period = 234 μs. (Images courtesy of Phil Guerieri)[174]

The frequency and intensity of the micro-explosions correspondingly increases with tetramer concentration in the hydrocarbon fuel. Due to these disruptions the mass and liquid volume of the droplets are decoupled. To compensate, a model estimate is fitted by considering a diameter measurement immediately following a micro-explosion event. At this time the droplet is most likely to include the least amount of internally inflating gaseous product. Fitting the classical, D^2, model to these points leads to a high probability that the burning rate will be underestimated because the droplet is most likely not free of internal gas. Therefore, the determined value provides an estimation of the minimum apparent burning rate of 8% due to the $[AlBrNEt_3]_4$ additive (Table 6.1).

As mentioned previously there are two methods for determining the burning rate of the droplet employed in this study. This is necessary due to aforementioned

disruptions. This was accomplished through observation of the entire combusting droplet trajectory. Both the pure solvent and nAl additive sample terminate explosively at the critical droplet size of 0.1 mm (Figure 6.3). Tetramer additive samples quench more slowly with solid product remaining (Figure 6.3).

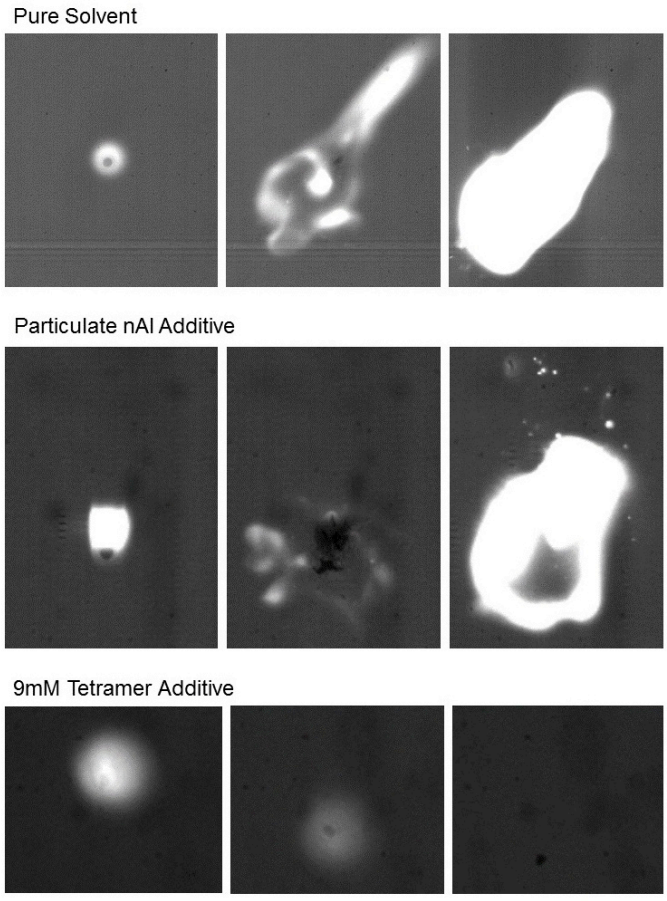

Figure 6.3. Termination of different samples being studied: pure solvent, fuel doped with nAl, fuel doped with tetramer (Images courtesy of Phil Guerieri).[174]

The solid particles left after the burning of the tetramer-containing droplet were collected to confirm the body observed in the termination video is the same size as the remaining solid particle. Once corroborated it was assumed that all the liquid solvent in the tetramer sample burns and the critical diameter of termination is taken to be zero. This allows the termination of $[AlBrNEt_3]_4$ laden droplets to be comparable to nAl and pure solvent

samples. The burning rate constants measured by both described methods are listed in Table 6.1. The constants determined for both the control and nAl sample show a reasonable correlation by the two differing measurement methods; Guerieri performed calculations and analyses of the burning rates. The termination-based measurement is not compromised by the disruptive nature of the tetramer, and yields a more accurate estimate for disruptive samples. This method shows a 20% increase in burning rate for both fuels containing $[AlBrNEt_3]_4$ concentrations of 5.2 mM and 9.7 mM compared to the pure control (Table 6.1).

Table 6.1. Burning rate constants determined via traditional D^2 law and full trajectory of droplet.

Additive	Active [Al]	Burning rate Constant, K	
		D^2 Trend	Time to Termination
None (Control)	None	1.41	1.47
Triethylamine	None	1.48	1.52
0.2 wt% nAl (1.6 mg/mL)	50 mM	1.37	1.43
5.2 mM $[AlBrNEt_3]_4$	21 mM	(Disruptions)	1.80
9.7 mM $[AlBrNEt_3]_4$	39 mM	(Disruptions)	1.79

6.2.4 SEM-EDX and XPS analysis

Due to the fact that the tetramer-containing droplets terminate with solid still remaining, the solid particles were collected and analyzed. Elemental analysis of the outer surface of the particle shows an Al:O atomic ratio of ≈0.3 (Al_2O_3 = 0.6 ≈ atomic %) carbon while and open pore in the particle shows an Al:O atomic ratio of ≈1.3 with 30 atomic % carbon. There is inherent error with EDX analyses of oxygen concentrations, but the conclusion can be drawn that the particle is predominantly composed of Al_mO_n and carbon from the toluene fuel. To corroborate the EDX analyses XPS was performed

on the particles. XPS also revels a high percentage of carbon (79.43%) and atomic ratio of Al:O to be 0.3 %, which supports the conclusions drawn from EDX.

6.2.5 TPR Experiments

Bowen et al. performed TPR experiments on yellow crystalline, $[AlBrNEt_3]_4$ to gain mechanistic insight on the combustion process. First the tetramer was studied by heating the sample in vacuum from 25°C to 110 °C at 10 °C/min. Analysis of the evolved gases by mass spectroscopy shows that the tetramer begins to decompose at 45°C to give NEt_3 (101 amu), and its decomposition products (58 and 86 amu). A similar experiment was conducted in which crystalline $[AlBrNEt_3]_4$ was dosed with 1×10^{-5} Torr of isotopically labeled $^{18}O_2$ gas and heated by the same schedule described above. The resulting gases (Figure 6.4a) are virtually identical to the in-vacuo control TPR experiment yielding only NEt_3 and its decomposition fragments. XPS analysis of the resulting white residue showed Br and Al(III), presumably Al_2O_3 (Figure 6.4b). This supports the theory of preferential oxidation of aluminum put forth by Hooper *et al.* through DFT calculations.[55] The TPR of the tetramer was repeated a third time, dosing with D_2O (1×10^{-4} Torr) prior to heating to investigate possible reactions induced by the presence of water in the droplets. The resultant spectra show that the major product is still the labile NEt_3 consistent with the previous two experiments, but closer examination of 75–84 amu mass spectrum region reveals the production of $D^{79}Br$ at ≈50°C (Figure 6.5).

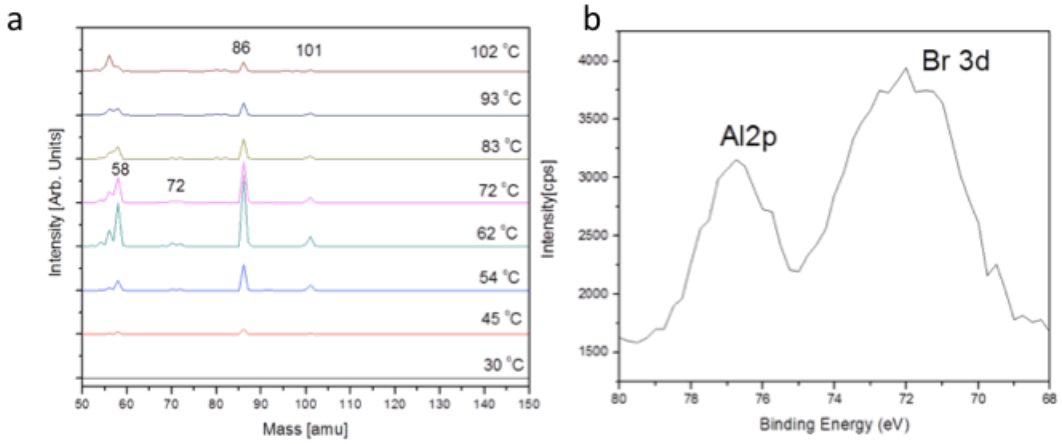

Figure 6.4. (a) TPR spectra of reaction of $[AlBrNEt_3]_4$ with $^{18}O_2$ @ 1 x 10^{-5} Torr. Peaks correspond to NEt_3 and its known fragmentation pattern (b) XPS Spectra of sample after the reaction showing Al and Br remaining (Images courtesy of Bowen).

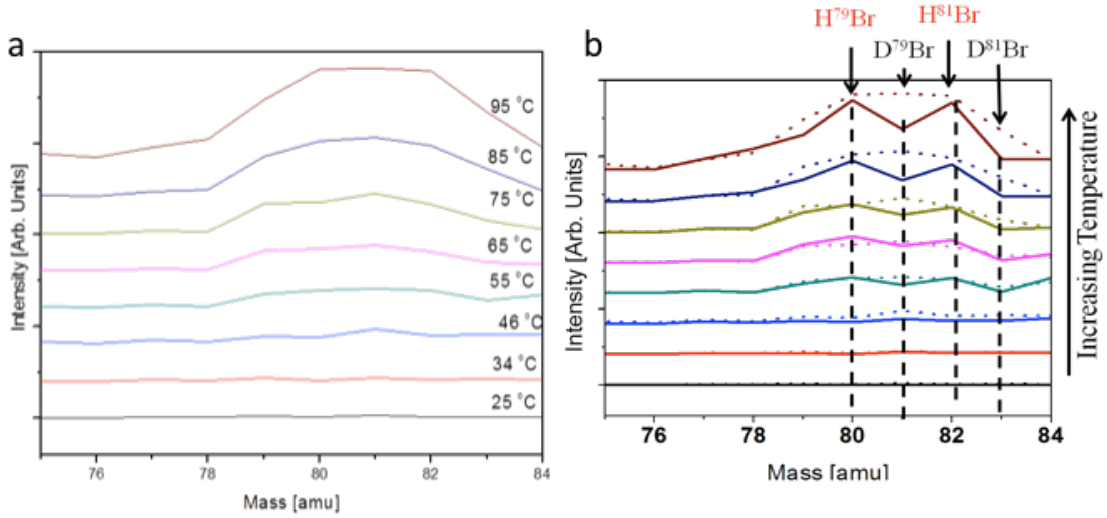

Figure 6.5. TPR reaction spectra of $[AlBrNEt_3]_4$ (a) Reaction of $[AlBrNEt_3]_4$ exposed to D_2O at 1.0 x 10^{-4} Torr for 1 hour. The chamber was the evacuated to 1 x 10^{-7} Torr and the TPR was subsequently taken. (b) Comparison of TPR of $[AlBrNEt_3]_4$ exposed to D_2O (dotted line) and not exposed to D_2O (solid line). This comparison demonstrates that exposure to D_2O does generate some $D^{79}Br$, in support of the proposed mechanism for the 'gas eruptions' as the droplet is burning (Images courtesy of Bowen).

6.3 Discussion

Addition of $[AlBrNEt_3]_4$ shows a 20 % increase in the burning rate constant when compare to the control and nAl samples, and TPR experiments show that the NEt_3 ligand is not preferentially oxidized. When it comes to analyzing the burning of the droplet, it is also important to take note of the "micro-explosions" which make it difficult to analyze the droplets via the traditional D^2 law. A common explanation for similarly observed events in other multi-component droplets is that if the boiling points of components are different enough, the lower boiling point fuel can be superheated when the droplet temperature is driven up by the higher boiling point of the other components.[176,177] This explanation aids in the description of the explosive terminations observed on the control samples. However, this is not an adequate explanation for the micro-explosions observed in the tetramer samples, since these events were unobserved in the control sample (i.e. blank solvent and NEt_3 doped sample). Therefore, the micro-explosions must be attributable to the tetramer.

In order to mechanistically explain the decomposition pathway and observable micro-explosion events solid $[AlBrNEt_3]_4$ was studied through the use of temperature-programmed reaction (TPR) experiments, specifically O_2 and D_2O oxidants. Since the oxygen concentrations on the fuel side of the spherical diffusion flame is very small, we postulated that the water by-product of the tol:Et_2O solvent combustion process was diffusing from the flame to the droplet, and reacting with the $[AlBrNEt_3]_4$ cluster to generate HBr and Al-O. Control experiments in the tower show that micro-explosive gas eruptions were not a result (i.e. not observed) of boiling solvent or of liberated NEt_3 ligand from the cluster. These experiments showed the major product in the presence of

O_2 and D_2O is NEt_3 and its degradation products, but in the presence of D_2O the production of DBr also occurs indicating direct reaction of D_2O with the tetramer.

Breaking down these observations chemically we propose the following simplified step-by-step mechanism (Eq. 6.3–6.5).

$$Toluene/Et_2O + O_2 \rightarrow CO_2 + H_2O \tag{6.3}$$

$$[AlBrNEt_3]_4 + H_2O \rightarrow HBr_{(g)} + \left[AlOH_2NEt_3\right]_n \tag{6.4}$$

$$\left[AlOH_2NEt_3\right]_n + O_2 \rightarrow \left[AlO(OH)\right]_n + NEt_3 \tag{6.5}$$

Early in the droplet lifetime the tetramer concentration is considered homogenous. In terms of elementary reactions, it is difficult to interpret the order at which reaction steps are occurring but in a global sense, combustion of the solvent yields CO_2 and H_2O in the flame region (Eq. 6.3).

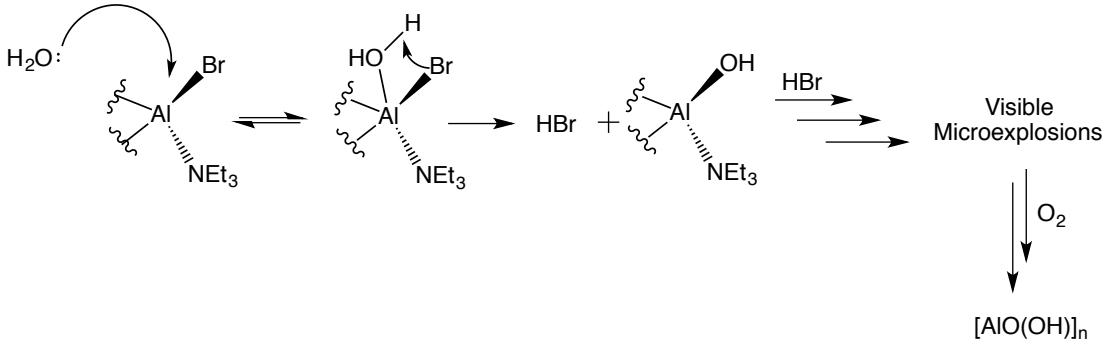

Figure 6.6. $[AlBrNEt_3]_4$ dissolved in a mixture of toluene/Et_2O exposed to an O_2 atmosphere and burned, the combustion of the solvents leads to the formation of $CO_{2(g)}$ and $H_2O_{(g)}$ (Eq. 6.3). The H_2O contributes the oxidation of Al^{1+} the formation of $HBr_{(g)}$ and the expulsion of $NEt_{3(l)}$ leading to a critical point at which visible micro-explosions occur (Eq. 6.4). These explosions lead to increased mixing of the droplet and its contents with the O_2 leading to the formation of $[AlO(OH)]_n$ products (Eq. 6.5).

Upon diffusion of combustion products from the flame into the droplet, reaction of H_2O with the AlBr tetramer, as indicated by the TPR experiments, will lead to the production of HBr gas. Early in the droplet lifetime when it is largely homogenous, this will occur close to the droplet surface, nearest the source of H_2O in the flame. However, liberation

of HBr gas promotes convective mixing near the droplet surface and increase transport of water further into the droplet yielding HBr gas within the liquid, exemplified by the mixing evident upon gas generation in Figures 6.2 and 6.6. This enhanced mixing should promote faster tetramer decomposition and the formation of HBr. At high enough concentrations, the gas will nucleate to bubbles and result in the micro-explosions observed (Figures 6.2). These gas release events transport more fuel to the flame region and the effect the burning rate. The droplet then returns to a deflated droplet form until the next visible event (Figure 6.2). This process is repeated throughout the remainder of the droplet lifetime, until the solvent flame extinguishes where the major product left is aluminate (refer to section 6.2.4).

The mechanism proposed is supported by the lack of visible micro-explosion in less concentrated samples, wherein less tetramer is available for reaction and HBr liberation, and the observation of micro-explosions only in the last ≈ 30% of the droplet burn time. In summary, the production of HBr contributes to bubble nucleation and droplet deformation to allow for increased mixing of the droplets with the oxidizing environment and thus increased reactant transport and burning rate.

6.4 Conclusions

The investigation of discrete soluble aluminum-bromide cluster additive to liquid fuel is presented here. The use of a drop tower apparatus to observe droplet combustion characteristics including a fit to the classical droplet burn law, which minimizes uncertainty caused by disruptive burning. The AlBr tetramer additive increases the burning rate of a toluene-ethyl ether fuel mixture by 20% in a room temperature oxygen environment with 39 mM of active aluminum additive (approximately 0.16 wt % limited

by additive solubility). At 50 mM (0.2 wt %) active aluminum, an analog nanoaluminum additive does not appreciably increase the liquid burning rate at such a low concentration. This study shows that the soluble architecture of the Al-based additive contributes a novel mechanism to increase the burning rate of hydrocarbon fuels, proving significantly more reactive than its particulate Al counterpart. This is the first example in support of the postulations that low-valent aluminum products will increase energetic output, but further studies are needed to ascertain the influence of reduced oxidation state aluminum.

6.5 Experimental Details

General considerations. All reactions are performed under an argon atmosphere in a glovebox or under dinitrogen using standard Schlenk techniques. Toluene and diethyl ether were purified by distillation from sodium benzophenone ketyl under a dinitrogen atmosphere, and triethylamine was purified through distillation over calcium hydride. All purified solvents were stored in modified Schlenk vessels over 3 Å molecular sieves under an argon atmosphere. The ^{1}H and ^{13}C NMR spectra were recorded on a Bruker DRX500 Avance spectrometer.

Synthesis of AlBr•$(NEt_3)_n$: Aluminum metal (0.8410 g, 31.1 mmol) was reacted with gaseous HBr (36.5 mmol) over 3 hours at approximately 1200 K in a modified Schnöckel-type metal halide co-condensation reactor.[178] The resultant gas-phase AlBr was co-condensed with a mixture of toluene:triethylamine (3:1 v/v) at approximately 77 K. The solvent matrix was thawed to –80 °C and the resultant yellow-brown solution stored at that temperature prior to use. Titration of the AlBr•$(NEt_3)_n$ solution via Mohr's method revealed a bromide concentration of 201 mM yielding an Al:Br ratio of 1:1.10.

Synthesis of [AlBrNEt$_3$]$_4$: A 40 mL aliquot of AlBr•(NEt$_3$)$_n$ was transferred to a Schlenk flask. Approximately 10 mL of solvent was removed in vacuo while warming the solution to room temperature. Solvent removal stop upon observing the formation of yellow solid stood at room temperature overnight. The next day the yellow solid was isolated, and washed with copious amounts of hexanes, crystals suitable for X-ray diffraction were obtained. ^{1}H NMR (500 MHz, tol-d8): δ (ppm) = 1.18 (t), 3.08(q) ^{13}C NMR (400 MHz, tol-d8): δ (ppm) = 9.80, 49.05. Synthesis adapted from [173].

[AlBrNEt$_3$]$_4$ solution (doped hydrocarbon fuel): In a glovebox 36.4 mg (0.04374 mmol) of [AlBrNEt$_3$]$_4$ was dissolved in 3.6 mL of dry toluene. After 20 minutes, 0.9 mL of dry Et$_2$O was added to the aluminum tetramer solution, for a final solution concentration of 9.72 mM [AlBrNEt$_3$]$_4$. The solution was then taken up in Hamilton Model 1005 SL Gastight Syringe, and sealed via syringe lock. The 5.12 mM sample was prepared in a similar manner utilizing 17.9 mg (0.0215 mmol) of [AlBrNEt$_3$]$_4$ and was dissolved in 4.5 mL of tol/Et$_2$O (4:1) mixture.

Physical Methods

TPR Experiments: Performed by Bowen *et al.* at the Johns Hopkins University.

Crystallography Experiments. Performed by Dr. Peter Zavalij at UMD.

Tower Construction: Yetter *et al.*(Penn State) and adapted by Phil Guerieri at UMD

Burn Rate Data Analysis: Performed by Phil Guerieri at UMD

Chapter 7: Conclusions

7.1 Summary of Work

This thesis describes the synthesis of aluminum containing products synthesized from AlX precursors, and highlights the use of these materials as a hydrocarbon fuel additive. Materials isolated contain aluminum in oxidation states ranging from 0 to 3+ and were characterized through a variety of techniques including: X-ray crystallography, NMR spectroscopy, ESI-MS, XRD, zero-field cooled magnetometry, and TEM. The application of low-valent aluminum materials as a fuel additives were studied via modified droplet tower.

All of the materials studied were made from the AlX solutions produced via the 'Schnöckel route'. Studies on low oxidation state main group chemistry, particularly aluminum, are still in their infancy. Relatively little is still known about the behavior of the solutions and low-valent aluminum products. Solutions studies involving AlBr and thiolate ligands shows the relationship between reaction conditions and the size of Al-clusters in solution, and further studies should result in isolated low-valent aluminum products containing Al–Al bonds. The aluminum monohalide solutions have yielded the opportunities to study reduced oxidation state aluminum on a relatively large scale and have produced the unique discrete isolated materials discussed in this thesis: $[HAl_3(PPh_2)_6]^{2-}$, $[Al(^{tBu}bpy)_3]$, and $[Al(^{Me}bpy)_3]$. Studies on these materials have given insight into unique properties, such as unexpected magnetic behavior in the case of $[Al(^{Me}bpy)_3]$.

Characterization of $[HAl_3(PPh_2)_6]^{2-}$ highlighted the unexpected diamagnetic behavior of the cluster due to the presence of H in the cluster core. NMR studies show the

congruence of signals that occur with the free ligand and bound diphenylphosphide, and demonstrate some of the difficultly encountered when characterizing this cluster.

Aluminum NPs have held a great area of interest due to the high enthalpy of combustion intrinsic to aluminum. There have been a number of methods involving the passivation of Al NPs, in order to optimize the exploitation of their potential energetics.[154,179] A common issue that is observed in these processes is the agglomeration of the NPs, and commercial NPs are usually larger in size (>100 nm). This study shows that use of AlX as the source for aluminum nanoparticles, and its subsequent reduction in the presence of graphene or graphene oxide yields supported Al NPs. In the case of the graphene supported Al NPs the average NP size was ≈23 nm, and were well dispersed and faceted on the surface of a monolayer of graphene.

The relationship between metalloid clusters produced from disproportionation reactions involving AlX and FCC aluminum have been established.[112] Based on theoretical calculations reduced oxidation state aluminum should have high heat of combustion.[54] Large metalloid clusters are kinetically passivated by and outer shell of ligands, but theoretical studies have shown that the Al core of these clusters would be preferentially oxidized.[55] A major issue in pursuing studies to test metalloid clusters as energetic materials are low yields and air-sensitivity. Described here is the experimental studies low-valent aluminum cluster ($[AlBrNEt_3]_4$) in terms of energetic output. It has been shown that preferential oxidation of the aluminum does occur, and that addition of the tetramer increases the burning rate of the droplet. This represents the first step towards future studies of Al-metalloid clusters as additives to increase energetic output in materials.

7.2 Future Directions

This dissertation highlights new and novel products produced from AlX precursors. There is still little understood about the overall behavior of AlX solutions, but the analysis of a new class of compounds produced from AlX, $[Al(^{R}bpy)_3]$, coupled with exhaustive characterization of $[LiOEt_2]_2[HAl_3(PPh_2)_6]$ are describe. Some insight into the reaction behavior of AlX is given through the solution studies of AlX and thiolates. The relationship between AlX and bulk aluminum metal is further explored through the synthesis of Al-NPs. And finally the development of mechanism of combustion of a reduced oxidation state cluster, $[AlBrNEt_3]_4$, is emphasized through a combination of synthesis and experimental design.

There are many directions that this project can go in based on the results presented here. For the elucidation of new metalloid aluminum cluster the use of ESI-MS for characterization of reaction mixtures should be an integral part of the study of new ligand sets. Our design and implementation of an air-free ESI-MS has provided useful insight into the complex reaction environment of AlX and thiolates. The study described here (Chapter 4) demonstrates that there are a wealth of products that can be obtained from thiolate ligands and that pursuit of novel Al-containing products through reactions of thiolates with AlX are worthwhile. This project will grow through the use of ESI-MS for screening of reaction mixtures with various ligand sets, and give guidance to future directions that this project can take.

In this thesis the characterization of both bpy containing complexes aluminum $[Al(^{R}bpy)_3]$ (R= Me or tBu) is described. This study highlights the use of electrochemistry for characterization and also the unusual magnetic behavior at low

temperatures for $[Al(^{Me}bpy)_3]$. Further studies concerning the magnetism of these complexes may provide more insight into the magnetic behavior of aluminum, specifically how the ground and excited state behavior of aluminum influences characteristics of aluminum containing compounds and complexes. Further experiments involving the Al tris-bpy complexes could also focus on the isolation of the other accessible oxidation states, $[Al(^{R}bpy)_3]^n$ (n =-3 to +3), as observed in the electrochemical experiments, and could be isolated through means of electrochemical deposition. There is a lot of information that can be gleaned from electrochemical experiments and our lab is now outfitted to perform such experiments in an air-free manner.

Characterization of $[LiOEt_2]_2[HAl_3(PPh_2)_6]$ demonstrates the importance of utilizing NMR spectroscopy as tool in characterization of isolated products. Through NMR we are able to separate multiple products based on rates of diffusion, and this methodology should be a useful tool in the analysis of future Al containing clusters and complexes. A more important endeavor in terms of NMR will be the institution and implementation of ^{27}Al NMR which can further assist in the understanding of the solution-phase of the these complex products. Additional studies on this particular cluster, $[LiOEt_2]_2[HAl_3(PPh_2)_6]$, can be performed to show the location and presence of the H-atom. These analyses could give insight into the relationship between the $[HAl_3(PPh_2)_6]^{2-}$ and $[Al_4(H_6)]^{2-}$, further bridging the relationship of gas and solution phase chemistry of aluminum.[121]

These crystalline materials ($[Al(^{R}bpy)_3]$ and $[LiOEt_2]_2[HAl_3(PPh_2)_6]$) can be produced on a relatively large scale, and may prove to be useful starting materials in the

pursuit of isolating new aluminum containing products. Further defining the chemistry of aluminum.

The other vein of this project was centered upon the isolation of Al NPs from AlX precursors and the study of the combustion of aluminum in the reduced oxidation state. The development of synthetic pathways for the isolation of Al NPs from AlX solutions now allows for the study of the catalytic studies of the supported NPs. Since the synthesis for monometallic particles have been developed synthesis of bimetallic Al-NPs can now be targeted using AlX precursor. There are relatively few examples of bimetallic Al-NPs in the literature[180] and utilizing AlX as the aluminum source for bimetallic NPs is a worthwhile pursuit.

With the description of the first study of the combustion of a low-valent aluminum cluster, there is now a protocol established through our collaborations how to analyze these solutions. Expansion of this experimental design to allow for the combustion analyses of the AlX solutions and other reduce oxidation state aluminum cluster and complexes can perhaps be the next steps to the ultimate goal of analyzing aluminum metalloid clusters in terms of energetic output.

The materials studied represent a small sample into what can be isolated from AlX solutions. These products range from mononuclear species (Al^{3+}) to bulk aluminum (Al^{0}) some of which have been described here. These monohalide solutions have the potential to yield high nuclearity aluminum clusters, as established by Schnöckel *et al*., and studies described here provides some insight into the behavior of AlX solutions, to assist in future endeavors to elucidate aluminum metalloid clusters.

Appendices

8.1 Appendix A. Description of Air-Free ESI-MS source

This appendix contains details on the air-free source for ESI-MS designed for used in this project. A major goal of this project was to develop a characterization technique that would allow more insight into the aluminum monohalide solutions, subsequent reaction mixtures, and products. We believe that ESI-MS is the answer to these needs. The design and construction of an air-free inlet source is a critical feature of this approach. This basic design includes:

- Air free needle inlet
- High voltage source
- Temperature control (if needed)
- Inert gas inlet
- Vacuum outlet

Our current set-up can be viewed in Figures A.1 and A.2.

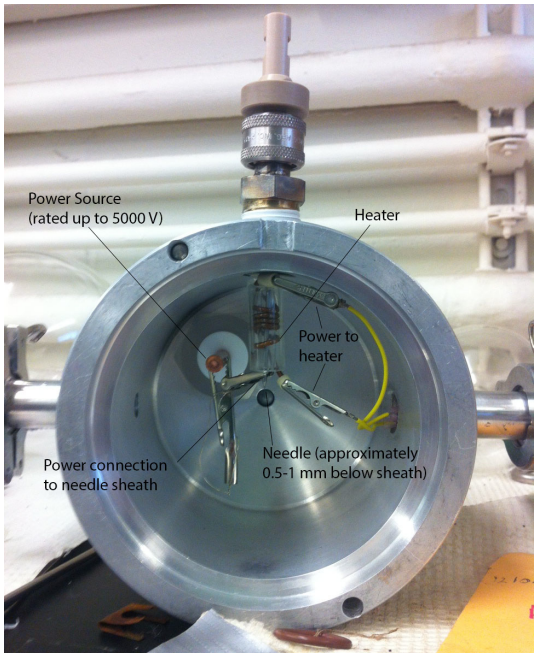

Figure A 1. Internal set-up for ESI-MS source; body for the source is constructed aluminum and was machined at UMD. Power source (rated up to 5000 V) and power source for the heater were purchased from Kurt Lesker©.

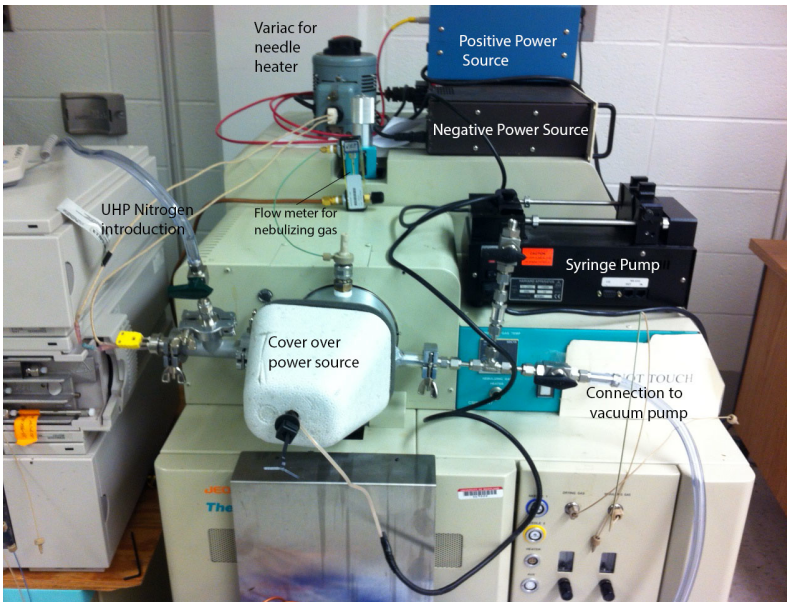

Figure A 2. External set-up for air-free ESI-MS data collection at UMD; prior to sample introduction the whole system is evacuated and purged via connection to an external vacuum pump and UHP nitrogen introduction. The set-up is outfitted for data collection in both positive and negative mode, and the samples are introduced via and external syringe pump in an airtight syringe.

This design and source has been implement at UMD, and is used as a source of solution characterization in chapters 2, 3, and 4. It has proven to be invaluable is assisting with product characterization ($[HAl_3(PPh_2)_6]^{2-}$ and $[Al(^{R}bpy)_3]$) and yielding insight into the basic AlX and alkali salt reactions (thiolate studies). Future work on this project will be bolstered by the information gleaned from ESI-MS studies.

References

(1) Uhl, W. *Zeitschrift fuer Naturforschung, B: Chemical Sciences* **1988**, *43*, 1113.
(2) Tacke, M.; Schnöckel, H. *Inorg. Chem.* **1989**, *28*, 2895–2896.
(3) Timms, P. L. *Accounts of Chemical Research* **1973**, 1–6.
(4) Schnöckel, H. *Dalton. Trans.* **2008**, 4344–4362.
(5) Schnöckel, H. *Chem. Rev.* **2010**, *110*, 4125–4163.
(6) Schnepf, A. *Eur. J. of Inorg. Chem.* **2008**, *2008*, 1007–1018.
(7) Hoberg, H.; Krause, S. *Angew. Chem.* **1976**, *88*, 760.
(8) Wiberg, N.; Blank, T.; Kaim, W. *Eur. J. Inorg. Chem.***2000**, 1475–1481.
(9) Klinkhammer, K. W.; Hiller, W.; Uhl, W.; Wagner, J. *Angew. Chem.***1991**, *103*, 182.
(10) Atkins, P. *Shriver and Atkins' Inorganic Chemistry*; Oxford University Press, USA, 2010.
(11) Cui, C.; Roesky, H.; Schmidt, H.-G.; Noltemeyer, M.; Hao, H.; Cimpoesu, F. *Angew. Chem.* **2000**, *39*, 4274–4276.
(12) Nagendran, S.; Roesky, H. W. *Organometallics* **2008**, *27*, 457–492.
(13) Dolbier, W. R.; Battiste, M. A. *Chem. Rev.* **2003**, *103*, 1071–1098.
(14) Downs, A. J. *The Group 13 Metals Aluminium, Gallium, Indium and Thallium: Chemical Patterns and Peculiarities*; Aldridge, S., Ed.; 1st ed.; Chichester, UK, 2011.
(15) Wiberg, N.; Amelunxen, K.; Blank, T.; Noth, H. *Organometallics* **1998**.
(16) Wehmschulte, R. J.; Ruhlandt-Senge, K.; Olmstead, M. M.; Hope, H.; Sturgeon, B. E.; Power, P. P. *Inorg. Chem.* **1993**, *32*, 2983–2984.
(17) Wright, R. J.; Brynda, M.; Power, P. P. *Angew. Chem. Int. Ed. Engl.* **2006**, *45*, 5953–5956.
(18) Bonyhady, S. J.; Collis, D.; Frenking, G.; Holzmann, N.; Jones, C.; Stasch, A. *Nature Chem* **2010**, *2*, 865–869.
(19) Schnepf, A.; Schnöckel, H. *Angew Chem Int Edit* **2002**, *41*, 3533–3552.
(20) Andreas Purath, R. *Angew Chem Int Edit* **1999**, *38*, 2926–2928.
(21) Yang, P.; Koeppe, R.; Duan, T.; Hartig, J.; Hadiprono, G.; Pilawa, B.; Keilhauer, I.; Schnöckel, H. *Angew Chem Int Edit* **2007**, *46*, 3579–3583.
(22) Henke, P.; Trapp, N.; Anson, C. E.; Schnöckel, H. *Angew. Chem. Int. Ed.* **2010**, *49*, 3146–3150.
(23) Kohnlein, H.; Stosser, G.; Baum, E.; Mollhausen, E.; Huniar, U.; Schnöckel, H. *Angew Chem Int Edit* **2015**, *39*, 799–801.
(24) Purath, A.; Dohmeier, C.; Ecker, A.; Koppe, R.; Krautscheid, H.; Schnöckel, H.; Ahlrichs, R.; Stoermer, C.; Friedrich, J.; Jutzi, P. *J. Am. Chem. Soc.* **2000**, *122*, 6955–6959.
(25) Huber, M.; Hartig, J.; Koch, K. *Z. Anorg. Allg. Chem.* **2009**, *635*, 423–430.
(26) Klemp, C.; Bruns, M.; Gauss, J.; Haussermann, U.; Stosser, G.; van Wullen, L.; Jansen, M.; Schnöckel, H. *J. Am. Chem. Soc.* **2001**, *123*, 9099–9106.
(27) Christoph Klemp, R. *Angew Chem Int Edit* **1999**, *38*, 1739–1743.
(28) Vollet, J.; Burgert, R.; Schnöckel, H. *Angew Chem Int Edit* **2005**, *44*, 6956–6960.
(29) Vollet, J.; Hartig, J. R.; Schnöckel, H. *Angew. Chem. Int. Ed. Engl.* **2004**, *43*, 3186–3189.

(30) Huber, M.; Schnepf, A.; Anson, C. E.; Schnöckel, H. *Angew. Chem. Int. Ed. Engl.* **2008**, *47*, 8201–8206.
(31) Kohnlein, H.; Purath, A.; Klemp, C.; Baum, E.; Krossing, I.; Stosser, G.; Schnöckel, H. *Inorg. Chem.* **2001**, *40*, 4830–4838.
(32) Ecker, A.; Weckert, E.; Schnöckel, H. *Nature* **1997**, *387*, 379–381.
(33) Purath, A.; Koppe, R.; Schnöckel, H. *Chem. Rev.* **1999**, 1933–1934.
(34) Ecker, A.; Weckert, E.; Schnöckel, H. *Nature* **1997**, *387*, 379–381.
(35) Jiang, W.; Knobler, C. B.; Hawthorne, M. F. *Angew. Chem. Int. Ed.* **1996**, *35*, 2535–2537.
(36) Thanh, N. T. K.; Maclean, N.; Mahiddine, S. *Chem. Rev.* **2014**, *114*, 7610–7630.
(37) Watzky, M. A.; Finke, R. G. *J. Am. Chem. Soc.* **1997**, *119*, 10382–10400.
(38) Aiken, J. D.; Lin, Y.; Finke, R. G. *J. Mole. Cat. A: Chem.***1996**, *114*, 29–51.
(39) Aiken, J. D.; Finke, R. G. *J. Mole. Cat. A: Chem.***1998**, *145*, 1–44.
(40) Champion, Y.; Bigot, J. *Nanostructured Materials* **1998**, *10*, 1097–1110.
(41) Pozarnsky, G. A. Process for the manufacture of metal nanoparticle, January 13, 2004.
(42) Abdelsayed, V.; Samy El-Shall, M. *Journal Chem. Phys.***2014**, *141*, 054710.
(43) Yamamoto, N.; Nishiyama, T.; Nagayama, K. *Process controlled synthesis of aluminum nanoparticles as a next generation propellant*; 819-0395; Department of Aeronautics and Astronautics, Kyushu University, 2007; pp. 1–2.
(44) Rai, A. Characterization and reactivity of aluminum nanoparticles, University of Minnesota, 2013, pp. 1–191.
(45) Pivkina, A.; Streletskii, A.; Kolbanev, I.; Ul'Yanova, P.; Forlov, Y. U.; Butyagin, P. *J. Mat. Sci.* **2004**, *39*, 5451–5453.
(46) Sen, P.; Ghosh, J.; Abdullah, A.; Kumar, P. *J. Chem. Sci.* **2003**, *115*, 499–508.
(47) Sindhu, T. K.; Sarathi, R.; Chakravarthy, S. R. *Nanotechnology* **2007**, *19*, 025703.
(48) Fernando, K. A. S.; Smith, M. J.; Harruff, B. A.; Lewis, W. K.; Guliants, E. A.; Bunker, C. E. *J Phys Chem C* **2009**, *113*, 500–503.
(49) Ghanta, S. R.; Muralidharan, K. *Nanoscale* **2010**, *2*, 976.
(50) Mahendiran, C.; Li, H.; Ganesan, R.; Meziani, M. J.; Gedanken, A.; Lu, F.; Bunker, C. E.; Guliants, E. A.; Sun, Y.-P. *Eur.J. Inorg. Chem.* **2009**, *2009*, 2050–2053.
(51) Abedin, El, S. Z.; Moustafa, E. M.; Hempelmann, R.; Natter, H.; Endres, F. *Electrochemistry Comm.***2005**, *7*, 1111–1116.
(52) Andres, R. P.; Averback, R. S.; Brown, W. L. *Materials Research* **1989**.
(53) Alnemrat, S.; Mayo, D.; DeCarlo, S.; Hooper, J. P. *Growth of metalloid aluminum clusters on graphene vacanies*; In preparation, 2015.
(54) Lightstone, J.; Hooper, J.; Stoltz, C.; Wilson, B.; Mayo, D.; Eichhorn, B.; Bowen, K. *APS Shock Compression of Condensed Matter Meeting Abstracts* **2011**, *-1*, 2006.
(55) Alnemrat, S.; Hooper, J. P. *J. Phys.: Conf. Ser.* **2014**, *500*, 172001.
(56) Kaes, C.; Katz, A.; Hosseini, M. W. *Chem. Rev.* **2000**, *100*, 3553–3590.
(57) P rez-Cordero, E.; Buigas, R.; Brady, N.; Echegoyen, L.; Arana, C.; Lehn, J.-

M. *Helv. Chim. Acta* **1994**, *77*, 1222–1228.
(58) Scarborough, C. C.; Wieghardt, K. *Inorg. Chem.* **2011**, *50*, 9773–9793.
(59) Bowman, A. C.; Sproules, S.; Wieghardt, K. *Inorg. Chem.* **2012**, *51*, 3707–3717.
(60) Wang, M.; Weyhermüller, T.; England, J.; Wieghardt, K. *Inorg. Chem.* **2013**, *52*, 12763.
(61) Pérez Cordero, E. E.; Campana, C.; Echegoyen, L. *Angew. Chem. Int. Ed. Engl.* **1997**, *36*, 137–140.
(62) Bowman, A. C.; England, J.; Sproules, S.; Weyhermüller, T.; Wieghardt, K. *Inorg. Chem.* **2013**, *52*, 2242–2256.
(63) England, J.; Wieghardt, K. *Inorg. Chem.* **2013**, *52*, 10067–10079.
(64) Baker, R. J.; Jones, C.; Kloth, M.; Mills, D. P. *New J. Chem.* **2004**, *28*, 207.
(65) Wulf, E.; Herzog, S. *Z. Anorg. Allg. Chem.* **1972**, *387*, 81–90.
(66) Ma, G.; Kritikos, M.; Maliarik, M.; Glaser, J. *Inorg. Chem.* **2004**, *43*, 4328–4340.
(67) Inoue, M.; Horiba, T.; Hara, K.-I. *Bull. Chem. Soc. Jap.* **1978**, *51*, 3073–3074.
(68) Herzog, S.; Geisler, K.; Präkel, H. *Angew. Chem. Int. Ed.* **1963**, *2*, 47.
(69) Herzog, S.; Grimm, U. *Z. Chem.* **1968**, *8*, 186–187.
(70) Herzog, V. S.; Gustav, K.; Schuster, R. *Z. Natur*. **1962**, *17b*, 67.
(71) Herzog, S.; Taube, R. *Z. Anorg. Allg. Chem.* **1960**, *306*, 159–179.
(72) Albrecht, G. *Z. Chem.* **1963**, 3, 182-187.
(73) Herzog, V. S.; Zühlke, H. *Z. Natur*. **1960**, *15b*, 466.
(74) Quirk, J.; Wilkinson, G. *Polyhedron* **1982**.
(75) Brandt, W. W.; Dwyer, F. P.; Gyarfas, E. D. *Chem. Rev.* **1954**, *54*, 959–1017.
(76) Herzog, V. S.; Renner, K. C.; Schön, W. *Z.. Natur*. **1957**, *12b*, 809.
(77) Herzog, S.; Schneider, I. *Z. Chem.* **1962**, *2*, 24–24.
(78) Herzog, S.; Präkel, H. *Z. Chem.* **1965**, *5*, 469–470.
(79) Hall, F. S.; Reynolds, W. L. *Inorg. Chem.* **1966**, *5*, 931–932.
(80) Herzog, S.; Klausch, U.; Lantos, J. *Z. Chem.* **1964**, *4*, 150–150.
(81) England, J.; Scarborough, C. C.; Weyhermüller, T.; Sproules, S.; Wieghardt, K. *Euro. J. Inorg. Chem.* **2012**, *2012*, 4605–4621.
(82) Wang, M.; England, J.; Weyhermüller, T.; Wieghardt, K. *Inorg. Chem.* **2014**, *53*, 140127145234003.
(83) van Albada, G. A.; Mutikainen, I.; Turpeinen, U.; Reedijk, J. *Acta Cryst (2005). E61, 1411-1412 [doi:10.1107/S1600536805019574]* **2005**, 1–2.
(84) Amarante, T. R.; Fernandes, J. A.; Gonçalves, I. S.; Almeida Paz, F. A. *Acta Crystallogr E Struct Rep Online* **2011**, *67*, m1828–m1829.
(85) Lehleh, A.; Beghidja, A.; Beghidja, C.; Mentré, O.; Welter, R. *Comptes Rendus - Chimie* **2011**, *14*, 462–470.
(86) Han, Z.-G.; Li, S.; Wu, J.-J.; Zhai, X.-L. *J.Coord. Chem.* **2011**, *64*, 1525–1532.
(87) Huang, W.; Qian, H. *Trans. Met. Chem* .**2006**, *31*, 621–629.
(88) Schwalbe, M.; Schäfer, B.; Görls, H.; Rau, S.; Tschierlei, S.; Schmitt, M.; Popp, J.; Vaughan, G.; Henry, W.; Vos, J. G. *Euro. J. Inorg. Chem.* **2008**, *2008*, 3310–3319.
(89) Sandroni, M.; Zysman-Colman, E. *Dalton. Trans.* **2014**, *43*, 3676.
(90) Li, J.-H.; Wang, J.-T.; Zhang, L.-Y.; Chen, Z.-N.; Mao, Z.-W.; Ji, L.-N. *Inorg*

Chim Acta **2009**, *362*, 1918–1924.
(91) Yang, X.-J.; Wu, B.; Janiak, C. *Cryst. Eng. Comm.* **2004**, *6*, 126.
(92) Rutherford, T. J.; Pellegrini, P. A.; Aldrich Wright, J.; Junk, P. C.; Keene, F. R. *Euro. J. Inorg. Chem.***1998**, *1998*, 1677–1688.
(93) Damrauer, N. H.; Boussie, T. R.; Devenney, M.; McCusker, J. K. *J. Am. Chem. Soc.* **1997**, *119*, 8253–8268.
(94) Zhang, Y.; Zhou, N.; Akella, S.; Kuang, Y.; Kim, D.; Schwartz, A.; Bezpalko, M.; Foxman, B. M.; Fraden, S.; Epstein, I. R.; Xu, B. *Angew. Chem. Int. Ed.* **2013**, *52*, 11494–11498.
(95) Yadav, Y. J.; Mastropietro, T. F.; Szerb, E. I.; Talarico, A. M.; Pirillo, S.; Pucci, D.; Crispini, A.; Ghedini, M. *New J. Chem.* **2013**, *37*, 1486.
(96) Nikiforov, G. B.; Roesky, H. W.; Noltemeyer, M.; Schmidt, H.-G. *Polyhedron* **2004**, *23*, 561–566.
(97) Bellavance, P. L.; Corey, E. R.; Corey, J. Y.; Hey, G. W. *Inorg. Chem.* **1977**, *16*, 462–467.
(98) Scarborough, C. C.; Sproules, S.; Weyhermüller, T.; DeBeer, S.; Wieghardt, K. *Inorg. Chem.* **2011**, *50*, 12446–12462.
(99) Martinez, C. R.; Iverson, B. L. *Chem. Sci.* **2012**, *3*, 2191.
(100) Chun, H.; Verani, C. N.; Chaudhuri, P.; Bothe, E.; Bill, E.; Weyhermüller, T.; Wieghardt, K. *Inorg. Chem.* **2001**, *40*, 4157–4166.
(101) Taube, H. *Chem. Rev.* **1952**, *50*, 69–126.
(102) D'Alessandro, D. M.; Keene, F. R. *Dalton. Trans.* **2004**, 3950.
(103) Myers, T. W.; Kazem, N.; Stoll, S.; Britt, R. D.; Shanmugam, M.; Berben, L. A. *J. Am. Chem. Soc.* **2011**, *133*, 8662–8672.
(104) Berry, G. A. B. A. J. F. *J. Chem. Ed.* **2008**, *85*, 532.
(105) Irwin, M.; Doyle, L. R.; Krämer, T.; Herchel, R.; McGrady, J. E.; Goicoechea, J. M. *Inorg. Chem.* **2012**, *51*, 12301–12312.
(106) Irwin, M.; Jenkins, R. K.; Denning, M. S.; Krämer, T.; Grandjean, F.; Long, G. J.; Herchel, R.; McGrady, J. E.; Goicoechea, J. M. *Inorg. Chem.* **2010**, *49*, 6160–6171.
(107) Mansell, S. M.; Adams, C. J.; Bramham, G.; Haddow, M. F.; Kaim, W.; Norman, N. C.; McGrady, J. E.; Russell, C. A.; Udeen, S. J. *Chem. Rev.* **2010**, *46*, 5070.
(108) Kobayashi, H.; Youkoh, K.; Matsuzawa, H.; Sekino, H. *Mol. Phys.* **1993**, *78*, 909–928.
(109) xdf, K. G.; Gatteschi, D.; Bogani, L. *Phys. Chem. Chemical Phys.* **2014**, *16*, 18076–18082.
(110) Wagner, M. J.; Dye, J. L.; Perez-Cordero, E.; Buigas, R.; Echegoyen, L. *J. Am. Chem. Soc.* **1995**, *117*, 1318–1323.
(111) Sudheendra Rao, M.; Roesky, H.; Anantharaman, G. *J. Organomet. Chem.* **2002**, *646*, 4–14.
(112) Schnepf, A.; Schnöckel, H. *Angew. Chem. Int. Ed. Engl.* **2002**, *41*, 3532–3552, 3511.
(113) Dohmeier, C.; Loos, D.; Schnöckel, H. *Angew Chem Int Edit* **1996**, *35*, 129–149.
(114) Burt, J.; Levason, W.; Reid, G. *Coordin Chem Rev* **2014**, *260*, 65–115.

(115) Zhao, Y.; Liu, Y.; Yang, L.; Yu, J.-G.; Li, S.; Wu, B.; Yang, X.-J. *Chem-Eur J* **2012**, *18*, 6022–6030.
(116) Huber, M.; Schnöckel, H. *Inorg Chim Acta* **2008**, *361*, 457–461.
(117) Rivard, E.; Power, P. P. *Inorg. Chem.* **2007**, *46*, 10047–10064.
(118) Robinson, G. H. *Accounts Chem. Research* **1999**, *32*, 773–782.
(119) Ichinohe, M.; Igarashi, M.; Sanuki, K.; Sekiguchi, A. *J. Am. Chem. Soc.* **2005**, *127*, 9978–9979.
(120) Wright, R. J.; Brynda, M.; Power, P. P. *Angew. Chem. Int. Ed. Engl.* **2006**, *45*, 5953–5956.
(121) Henke, P.; Huber, M.; Steiner, J.; Bowen, K.; Eichhorn, B.; Schnöckel, H. *J. Am. Chem. Soc.* **2009**, *131*, 5698–5704.
(122) Wiberg, N.; Amelunxen, K.; Blank, T.; Nöth, H.; Knizek, J. *Organometallics* **1998**, *17*, 5431–5433.
(123) Kandalam, A. K.; Boggavarapu, K. Calculations on $[Al_3(PPh_2)_6]^2$.
(124) Stepanova, V. A.; Dunina, V. V.; Smoliakova, I. P. *Organometallics* **2009**, *28*, 6546–6558.
(125) Ashby, E.; Gurumurthy, R.; Ridlehuber, R. *J. Organ. Chem.***1993**, *58*, 5832–5837.
(126) Yokoyama, Y.; Takahashi, K. *Bull. Chem. Soc. Jap.***1987,** 60, 3485.
(127) Less, R. J.; Simmonds, H. R.; Wright, D. S. *Dalton. Trans.* **2014**, *43*, 5785.
(128) Cohen, Y.; Avram, L.; Frish, L. *Angew. Chem. Int. Ed. Engl.* **2005**, *44*, 520–554.
(129) Johnson, C. S., Jr. *Progress in nuclear magnetic resonance spectroscopy* **1999**, *34*, 203–256.
(130) Kerssebaum, R.; Slanikov, G. *DOSY and Diffusion by NMR*; 2nd ed.; Topspin 2.0; Bruker BioSpin: Rheinstetten, Germany, 2006; pp. 1–32.
(131) Ovenden, S. P. B.; Bourne, D. J. *The Diffusion Ordered SpectroscopY (DOSY) Pulse Sequence and Defence Applications*; DSTO-TR-2130; Human Protection and Performance Division Defence Science and Technology Organisation (DSTO), 2008; pp. 1–18.
(132) Price, W. S. *Concepts in Magnetic Resonance* **1997**, *9*, 299–336.
(133) Price, W. S. *Concepts in Magnetic Resonance* **1998**, *10*, 197–237.
(134) Fernández, I.; Martínez-Viviente, E.; Pregosin, P. S. *Inorg. Chem.* **2004**, *43*, 4555–4557.
(135) Pregosin, P. S. Royal Society of Chemistry: Cambridge, 2011; Vol. 42, pp. 248–268.
(136) Li, D.; Keresztes, I.; Hopson, R.; Williard, P. G. *Accounts Chem. Res.* **2009**, *42*, 270–280.
(137) Jahn, H. A.; Teller, E. *Proc. R. Soc. A.* **1937**, 161, 220.
(138) Schnöckel, H.; Schnepf, A.; Whetten, R. L.; Schenk, C.; Henke, P. *Z. Anorg. Allg. Chem.* **2010**, *637*, 15–23.
(139) Daniel, S.; Hoffman, D. M. *Inorg. Chem.* **2002**, *41*, 3843–3849.
(140) Carmalt, C. J.; Mileham, J. D.; White, A. J. P.; Williams, D. J.; Rushworth, S. *Polyhedron* **2003**, *22*, 2655–2660.
(141) Lips, F.; Fettinger, J. C.; Power, P. P. *Polyhedron* **2014**, *79*, 207–212.
(142) Janiak, C. *J Chem Soc Dalton* **2000**, 3885–3896.

(143) Kehrwald, M.; Köstler, W.; Rodig, A.; Linti, G.; Blank, T.; Wiberg, N. *Organometallics* **2001**, *20*, 860–867.
(144) Klemp, C.; Stosser, G.; Krossing, I.; Schnöckel, H. *Angew. Chem. Int. Ed.* **2000**, *39*, 3691–3694.
(145) Duan, T.; St er, G.; Schn ckel, H. *Z. anorg. allg. Chem.* **2005**, *631*, 1129–1133.
(146) Akhavan, J. *Chemistry of Explosives*; 2nd ed.; Royal Society of Chemistry: Cambridge, 2004.
(147) Sims, C. M.; Ponce, A. A.; Gaskell, K. J.; Eichhorn, B. W. *Dalton. Trans.* **2015**, *44*, 977–987.
(148) Schniepp, H. C.; Li, J.-L.; McAllister, M. J.; Sai, H.; Herrera-Alonso, M.; Adamson, D. H.; Prud'homme, R. K.; Car, R.; Saville, D. A.; Aksay, I. A. *The J. Phys. Chem. B* **2006**, *110*, 8535–8539.
(149) Wan, D.; Yang, C.; Lin, T.; Tang, Y.; Zhou, M.; Zhong, Y.; Huang, F.; Lin, J. *ACS Nano* **2012**, *6*, 9068–9078.
(150) Al-Marri, A. H.; Khan, M.; Khan, M.; Adil, S. F. *Int. J. Mat. Sci.* **2015**, 16, 1131.
(151) Wang, W.; He, D.; Zhang, X.; Duan, J.; Wu, H.; Xu, H.; Wang, Y. *J Nanosci Nanotechnol* **2014**, *14*, 3412–3416.
(152) Huang, C.-F.; Yao, G.-H.; Liang, R.-P.; Qiu, J.-D. *Biosens Bioelectron* **2013**, *50*, 305–310.
(153) Henke, P.; Schnöckel, H. *Chem-Eur J* **2009**, *15*, 13391–13398.
(154) Shahravan, A.; Desai, T.; Matsoukas, T. *ACS Appl. Mater. Interfaces* **2014**, *6*, 7942–7947.
(155) Yetter, R. A.; Risha, G. A.; Son, S. F. Metal particle combustion and nanotechnology. *Proceedings of the Combustion Institute* **2009,** 32, 1819-1838.
(156) Choi, S.U.S.; Eastman, J.A. ASME International Mechanical Engineering Congress and Exposition, San Francisco, CA, November 12-17, **1995.**
(157) Kao, M.J.; Ting, C.C.; Lin, B.F.; Tsung, T.T. Aqueous Aluminum Nanofluid Combustion in Diesel Fuel. *J. Test and Eval.* **2008**, *36*, 1-5.
(158) Tyagi, H.; Phelan, P. E.; Prasher, R.; Peck, R.; Lee, T.; Pacheco, J. R.; Arentzen, P. *Nano Lett.* **2008**, *8*, 1410–1416.
(159) Mehta, R. N.; Chakraborty, M.; Parikh, P. A. *Fuel* **2014**, *120*, 91–97.
(160) Sajith, V.; Sobhan, C.B.; Peterson, G.P. *Advances in Mechanical Engineering.* **2010**, Article ID 581407.
(161) Sarvestany, N.S.; Farzad, A.; Ebrahimnia-Bajestan, E.; Massoud, M.. *Journal of Dispersion Science and Technology.* 2014, **35**(12), 1745-1750
(162) Singh, N.; Bharj, R. S. *International Journal of Current Engineering and Technology* **2015**, *5*, 477–485.
(163) Gan, Y.; Qiao, L. *International Journal of Heat and Mass Transfer* **2012**, *55*, 5777–5782.
(164) Gan, Y.; Qiao, L. *Energy Fuels* **2012**, *26*, 4224–4230.
(165) Javed, I.; Baek, S. W.; Waheed, K.; Ali, G.; Cho, S. O. *Combustion and Flame* **2013**, *160*, 2955–2963.
(166) Javed, I.; Baek, S. W.; Waheed, K. *Experimental Thermal and Fluid Science* **2014**, *56*, 33–44.
(167) Javed, I.; Baek, S. W.; Waheed, K. *Combustion and Flame* **2015**, *182*, 191–

206.
(168) Tanvir, S.; Qiao, L. *Journal of Propulsion and Power* **2015**, *31*, 408–415.
(169) Gan, Y.; Lim, Y. S.; Qiao, L. *Combustion and Flame* **2012**, *159*, 1732–1740.
(170) Gan, Y.; Qiao, L. *International Journal of Heat and Mass Transfer* **2011**, *54*, 4913–4922.
(171) Javed, I.; Baek, S. W.; Waheed, K. *Combustion and Flame* **2013**, *180*, 170-183.
(172) Gan, Y.; Qiao, L. *Combustion and Flame* **2011**, *158*, 354–368.
(173) Mocker, M.; Robl, C.; Schnöckel, H. *Angew. Chem. Int. Ed.* **1994**, *33*, 1754–1755.
(174) Guerieri, P. M.; DeCarlo, S.; Eichhorn, B.; Yetter, R. A.; Tang, X.; Hicks, Z.; Bowen, K. H.; Zachariah, M. R. Molecular Aluminum Additive for Burn Enhancement of Hydrocarbon Fuels, *In preparation* (2015).
(175) Godsave, G. A. E. *Fourth Symposium (International) on Combustion.* **1953**; Vol. 4, pp. 818–830.
(176) Law, C. K. *AIChE Journal* **1978**, *24*, 626–643.
(177) Wang, C. H.; Liu, X. Q.; Law, C. K. *Combustion and Flame* **1984**, *56*, 175–197.
(178) Tacke, M.; Schnöckel, H. *Inorg. Chem.* **1989**.
(179) Meziani, M. J.; Bunker, C. E.; Lu, F.; Li, H.; Wang, W.; Guliants, E. A.; Quinn, R. A.; Sun, Y.-P. *ACS Appl. Mater. Interfaces* **2009**, *1*, 703–709.
(180) Cokoja, M.; Parala, H.; Birkner, A.; Fischer, R. A.; Margeat, O.; Ciuculescu, D.; Amiens, C.; Chaudret, B.; Falqui, A.; Lecante, P. *Euro. J. Inorg. Chem.* **2010**, 1599–1603.